Insights from operating under gas-liquid Taylor flow and techno-economic optimisation Reactor design and economics of CO2 electrolysers

Bagemihl, I.

DOI
10.4233/uuid:3bc3bb7e-03f4-4941-90b0-57747b14e5e8

Publication date
2024

Citation (APA)
Bagemihl, I. (2024). *Insights from operating under gas-liquid Taylor flow and techno-economic optimisation: Reactor design and economics of CO2 electrolysers*. [Dissertation (TU Delft), Delft University of Technology]. https://doi.org/10.4233/uuid:3bc3bb7e-03f4-4941-90b0-57747b14e5e8

REACTOR DESIGN AND ECONOMICS OF CO_2 ELECTROLYSERS

INSIGHTS FROM OPERATING UNDER GAS-LIQUID TAYLOR FLOW AND TECHNO-ECONOMIC OPTIMISATION

REACTOR DESIGN AND ECONOMICS OF CO_2 ELECTROLYSERS

INSIGHTS FROM OPERATING UNDER GAS-LIQUID TAYLOR FLOW AND TECHNO-ECONOMIC OPTIMISATION

Dissertation

for the purpose of obtaining the degree of doctor
at Delft University of Technology,
by the authority of the Rector Magnificus Prof. dr. ir. T.H.J.J. van der Hagen,
Chair of the Board for Doctorates,
to be defended publicly on
Monday, 4th of November 2024 at 10 o'clock.

by

Isabell BAGEMIHL

Master of Science in Process Engineering,
University of Stuttgart, Germany,
born in Hamburg, Germany.

This dissertation has been approved by the promotors.

Prof. dr. ir. J. R. van Ommen
Dr. ir. V. van Steijn

Composition of the doctoral committee:

Rector Magnificus,	Chairperson
Prof. dr. ir. J. R. van Ommen,	Delft University of Technology, promotor
Dr. ir. V. van Steijn,	Delft University of Technology, promotor
Independent members:	
Prof. dr. F.M. Mulder	Delft University of Technology
Prof. dr. U.-P. Apfel	Ruhr University Bochum, Germany
Dr. ir. D.A. Vermaas	Delft University of Technology
Dr. M. Costa Figueiredo	Eindhoven University of Technology
Prof. dr. V. Garbin	Delft University of Technology, reserve member
Other members:	
Dr. ir. M.D.M. Pérez-Fortes	Delft University of Technology

This work was financially supported by the Electrons to Chemical Bonds program (E2CB), which is (partly) financed by the Dutch Research Council (NWO).

Keywords: Electrochemical CO_2 reduction, multi-scale model, Taylor-Flow, techno-economic optimisation, tubular electrolysers

Printed by:

Cover by: M. Peters

ISBN 000-00-0000-000-0

An electronic version of this dissertation is available at
`http://repository.tudelft.nl/`.

SUMMARY

The electrochemical conversion of captured carbon dioxide (CO_2) at low temperatures holds promise as a sustainable method for producing materials and fuel using renewable energy sources. However, technological hurdles such as mass transfer limitations and operational instability hinder its industrial application. This dissertation aims to address these challenges by exploring the use of gas-liquid Taylor flow (series of confined gaseous CO_2 bubbles, which are separated from each other by liquid electrolyte and from the channel walls by a thin liquid film) in electrolysis, which can enhance mass transfer without requiring complex electrode designs, potentially improving long-term operational reliability. Additionally, a multi-scale modelling framework is introduced to evaluate electrolyser designs from an economic standpoint, aiding in the identification of bottlenecks and guiding technology development.

In Chapter 2, we propose a tubular electrolyser design operating under gas-liquid Taylor flow to overcome mass transfer limitations. By developing a numerical model, we investigate the relationship between process conditions, mass transfer, and reactor performance. Insights gained from this model allow us to derive an easy-to-use analytical relation to evaluate the impact of changes in inlet flow rates on Faradaic efficiency and current density. We find that long gaseous CO_2 bubbles and low velocities enhance the current density towards CO, outperforming traditional H-cells. However, achieving performance comparable to flow-through electrolysers operated with a gas diffusion electrode (GDE) requires means to increase CO_2 solubility in the liquid electrolyte, by for example increasing pressure.

Chapter 3 focuses on experimentally testing how Taylor flow influences the electrolyser performance within the established zero-gap water electrolyser concept adapted for CO_2 reduction, by employing a silver gauze as the cathode. Our experimental findings reveal that Taylor flow enhances the Faradaic efficiency towards CO compared to single-phase flow, with minimal influence from gas holdup within the studied velocity range. Contrary to the tubular design, high velocities are desirable to increase the Faradaic efficiency towards CO in the rectangular flow channel. We find that further optimisation of cathode design and fabrication is needed to fully exploit the potential of this electrolyser concept.

In Chapter 4, techno-economic aspects of electrochemical CO_2 conversion are addressed, aiming to optimise operational parameters for industrial applications. A multi-scale model capturing mass transfer effects over the channel length of a GDE electrolyser is integrated into an economic framework to analyse the interdependencies of key performance variables on the economic outlook. The analysis indicates that optimal current densities may differ significantly from previously reported benchmarks, emphasising the importance of multi–scale modelling for evaluating electrolyser designs under economic considerations.

SAMENVATTING

De elektrochemische omzetting van kooldioxide (CO_2) met hernieuwbare energiebronnen bij lage temperaturen biedt hoop als duurzame methode voor het produceren van materialen en brandstof. Echter, technologische obstakels zoals massatransportbeperkingen en operationele instabiliteit belemmeren de industriële toepassing. In dit proefschrift wordt het gebruik van gas-vloeistof *Taylor flow* (reeks opgesloten gasvormige CO_2 bellen, die van elkaar gescheiden zijn door vloeibaar elektrolyt en van de kanaalwanden door een dunne vloeistoffilm) in elektrolyse onderzocht, om deze obstakels te overwinnen. *Taylor flow* kan de stofoverdracht verbeteren zonder complexe elektrodeontwerpen te vereisen, en daarom mogelijk de operationele betrouwbaarheid op lange termijn verbeteren. Daarnaast presenteren we een *multi-scale model* om de werking van de reactor onder Industriële omstandigheden te evalueren. Dit helpt bij het identificeren van knelpunten en het sturen van technologieontwikkeling.

In Hoofdstuk 2 stellen we een tubulaire elektrolyser voor die onder gas-vloeistof *Taylor flow* werkt, om massatransportbeperkingen te overwinnen. We ontwikkelen een numeriek model om de relatie tussen procesomstandigheden, massatransport en de werking van de reactor te analyseren. Uit de bevindingen van dit model kunnen we een eenvoudige analytische relatie afleiden om de effecten van veranderingen in de inlaatvolumestroom op selectiviteit (*Faradaic efficiency*) en stroomdichtheid (reactiesnelheid) te evalueren. We vinden dat lange gasbellen en lage stroomsnelheden de CO-gerelateerde stroomdichtheid verbeteren en dat de werking beter is dan in traditionele H-cellen. Om echter vergelijkbare prestaties te bereiken als *flow-through* electrolyser die een gasdiffusie-elektrode (GDE) gebruiken, moet de oplosbaarheid van CO_2 in de vloeibare elektrolyt verhoogd worden, bijvoorbeeld door de druk te verhogen.

Hoofdstuk 3 richt zich op het experimenteel testen van hoe Taylor-stroming de prestaties van de electrolyser beïnvloedt binnen het gevestigde concept van de *zero-gap* water electrolyser, maar dan aangepast voor CO_2-reductie. We gebruiken een zilvergaas als kathode om de reductie van CO_2 te katalyseren. We tonen aan dat *Taylor flow* de selectiviteit voor CO verbetert in vergelijking met de inlaatvolumestroom, terwijl de invloed van de gas/vloeistofverhouding minimaal is. In tegenstelling tot cylindrische kanelen zijn hoge snelheden wenselijk in deze reactor met rechthoekige kanalen om de selectiviteit voor CO te verhogen. We concluderen dat verdere optimalisatie van het kathodemateriaal nodig is om het potentieel van dit reactorconcept volledig te benutten.

Hoofdstuk 4 behandelt de technisch-economische aspecten van de elektrochemische reductie van CO_2 in een GDE-reactor, met als doel het optimaliseren van de procesomstandigheden voor industriële toepassingen. Hiervoor ontwikkelen we een *multi-scale model* dat de massatransporteffecten over de lengte van de reactor voorspelt. De resultaten van dit model worden vervolgens geanalyseerd vanuit economisch perspectief. De analyse geeft aan dat de optimale stroomdichtheden aanzienlijk kunnen verschillen van de eerder gerapporteerde richtwaarden. Modelleren over meerdere schalen

is daarom essentieel voor de evaluatie van reactorontwerpen vanuit economisch perspectief.

CONTENTS

1

INTRODUCTION

1.1. ELECTROCHEMISTRY AND THE ENERGY TRANSITION

Energy sustains our daily lives, serving as the lifeblood of transportation, building material production, and the creation of everyday goods. Historically, our energy production heavily relied on burning fossil fuels, consequently releasing carbon dioxide (CO_2) into the atmosphere, a prominent greenhouse gas. Although nature possesses mechanisms for recycling naturally emitted CO_2, the advent of the industrial revolution introduced a linear energy flow, lacking a means to effectively recirculate emitted CO_2. This phenomenon contributed to an atmospheric CO_2 increase, recognised as a primary driver of climate change. Consequently, societal and governmental efforts over recent decades have concentrated on mitigating CO_2 emissions across all sectors and closing the carbon cycle, with the ultimate aim of achieving a carbon-neutral society [1–3]. In the process industry, this transition away from fossil fuels towards renewable energy sources is well underway, however accompanied by challenges such as the fluctuating nature of renewable power sources, necessitating large-scale energy storage and transportation solutions as well as the production of base chemicals from non-fossil feedstocks [4–6].

Electrochemistry emerges as a pivotal technology in this transition, utilising electrical energy—rather than thermal energy—to drive chemical reactions. It enables the storage of electricity from renewable sources like wind and solar energy in chemical bonds, notably hydrogen. Hydrogen, currently utilised as both an energy carrier and a fundamental component in industrial processes, faces challenges due to its low energy density, resulting in costly storage and transportation [7]. Additionally, the production of higher hydrocarbons, vital as fuels and base chemicals, necessitates a combination of carbon monoxide (CO) and hydrogen (H_2), referred to as syngas. One sustainable route to syngas production involves biomass gasification [8], which presents challenges related to biodiversity, food security, and water use at large scales [9]. Alternatively, captured CO_2 from industrial emissions, the atmosphere, or the ocean offers another avenue. Captured CO_2 can undergo electro-catalytic conversion into CO, subsequently combined with H_2 from water electrolysis to produce sustainable syngas for traditional processes like Fischer-Tropsch synthesis or fermentation, leading to the formation of higher hydrocarbons [10].

1

The electro-catalytic reduction of CO_2 has received significant attention since the 1990s, as it can be directly powered by electricity from renewable sources. Low-temperature and pressure electrolysis presents the additional advantage of requiring no supplementary energy input, rendering it a compelling prospect in electrifying the process industry. Despite successful demonstrations of electrochemical CO_2 conversion to CO and other hydrocarbons at laboratory scale, challenges in improving the performance of electrolysers in terms of selectivity and current density, while ensuring operational stability and overall economic viability hinder large-scale implementation. Consequently, this dissertation addresses the scientific challenges in reactor design by exploring a novel reactor type (electrolysis cell operated under gas-liquid Taylor flow) and evaluating one of the most studied reactor design from an economic perspective.

1.2. THESIS AIM, RESEARCH QUESTIONS AND EMBEDDING

The electrochemical conversion of CO_2 to CO or hydrocarbons shows promise for producing base chemicals from non-fossil sources. However, existing reactor designs, which strive to overcome mass transfer limitations in aqueous electrolytes, suffer from poor operational stability. A first aim of this dissertation is to explore an alternative approach by introducing gaseous CO_2 bubbles into narrow channels filled with liquid electrolyte, creating gas-liquid Taylor flow. This approach seeks to overcome mass transfer limitations without the need for complex electrode designs, potentially improving operational stability. A subsequent aim of this dissertation is to develop a multi-scale framework for assessing reactor designs from an economic perspective, aiding in the identification of bottlenecks and optimal operating conditions. These two aims are structured around three research questions:

1. Under what conditions are tubular reactors operating under gas-liquid Taylor flow a competitive electrolyser design for CO_2 conversion? (Chapter 2)

2. How does gas-liquid Taylor flow influence the reactivity and selectivity in a zero-gap membrane electrolyser for CO_2 reduction? (Chapter 3)

3. How can economic considerations help identify bottlenecks in electrolyser design and operation? (Chapter 4)

The overarching goal of this dissertation—to contribute to the technological advancement of electrolysers for the direct electrochemical conversion of CO_2—aligns with TU Delft's commitment to a sustainable future. TU Delft has initiated programs such as the Energy and Climate Action Initiative to facilitate collaboration between researchers and industry across various sectors. This dissertation is part of the Electrons to Chemical Bonds (E2CB) program, aimed at developing materials and reactor designs for the electrochemical production of base chemicals from CO_2, nitrogen, and biomass [11]. Collaborating with Dutch universities and industry partners such as Shell, TATA Steel, and Vattenfall, this project benefits from drawing on experimental and techno-economic expertise from various departments within TU Delft. Before addressing the research questions, we provide a concise background on electrolyser designs and performance metrics for the electrochemical conversion of CO_2 in the remainder of this chapter.

1.3. ELECTROLYSER DESIGNS

Electrochemical reactors for the electrochemical reduction of CO_2 are broadly divided into two categories: batch and flow-through reactors. Both categories share the following similarity: two electrodes which are locally separated but are conductively connected. The connection consists of an outer electrical circuit and an inner transport of charge which occurs in the form of ions in the electrolyte and electrons in the electrodes. The charge-transfer occurs at the electrode surface, with the reduction reaction (electron consuming reaction) at the cathode and the oxidation reaction (electron supplying reaction) at the anode. Typically CO_2 is reduced at the cathode, while water oxidation to oxygen serves as the counter reaction at the anode due to its ease of implementation. A polymeric membrane keeps the reaction products separated while ensuring good ionic conductivity.

Figure 1.1 a) shows a schematic of this common electrolyser set-up for a batch reactor, often referred to as H-cell. This reactor typically involves a stagnant liquid electrolyte on both the cathode and anode sides, with CO_2 continuously bubbling through the catholyte [12]. Depending on the electrode material CO_2 can be reduced to several products including formic acid over tin, higher hydrocarbons like ethylene over copper or CO over silver [13], i.e.,

$$CO_2(aq) + H_2O(l) + 2e^- \longrightarrow CO(g) + 2OH^-(aq). \tag{1.1}$$

The activation potential required for CO_2 reduction to any reaction product is similar to the equilibrium potential of the hydrogen evolution reaction

$$2H_2O(l) + 2e^- \longrightarrow H_2(g) + 2OH^-(aq), \tag{1.2}$$

leading to the simultaneous formation of hydrogen at the cathode. The oxygen evolution reaction at the anode side typically takes place over iridium under acidic and neutral conditions, or over a more cost-effective nickel-based electrode under alkaline conditions [14]. In H-cells the electrodes are either made out of foils or a catalyst layer is deposited together with a polymeric ink on an inert and conductive substrate such as a glassy carbon sheet. This electrode configuration leads to mass transfer limitations at low reaction rates. Flow-through reactors, which employ porous electrodes instead as shown in Figure 1.1 b) and c), overcome these mass transfer limitations which allows operation under industrially relevant conditions [15, 16]. Both types of flow-through reactors come with their unique advantages and challenges for CO_2 electrolysis, which are discussed in the following.

Figure 1.1 b) illustrates a design, featuring a zero-gap configuration where the membrane is sandwiched between the cathode and anode, often termed a membrane electrode assembly (MEA). The porous electrodes typically consist of a porous transport layer (PTL), which facilitates access of the reactant to the catalyst layer (CL), while providing the electrons required for the charge-transfer reaction. The catalyst particles are either coated on the membrane (CCM) or on the porous transport layer (CCS). Catalyst deposition in MEAs is particularly challenging, requiring both good ionic and electrical connections. For CO_2 electrolysis sputtering and airbrushing are common techniques for the deposition of the catalyst layer. The PTL at the anode side is either fabricated via

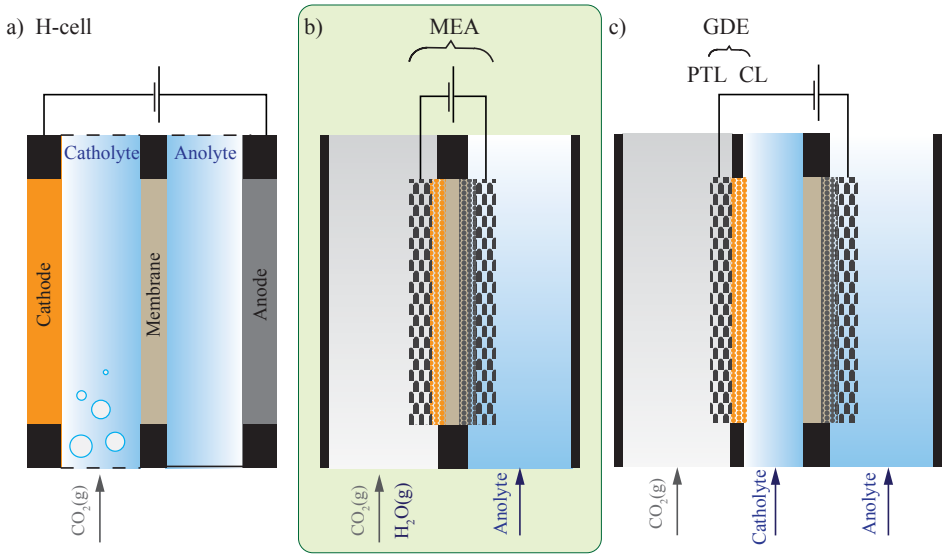

Figure 1.1: Sketch of a gas-fed batch cell/H-cell a), zero-gap flow-through cell with a membrane electrode assembly (MEA) fed with a gaseous CO_2 water-vapor mix b) and flow-through cell fed with a liquid catholyte and gaseous CO_2 which are separated by a gas diffusion electrode (GDE) comprised of the porous transport layer (PTL) and the catalyst layer (CL) c).The MEA set-up subject to most scale-up studies is highlighted in green.

sintering metal particles like titanium, or using structured sheets, foams, or grids. At the gas-fed cathode side the PTL is typically made from carbon fibres in the form of carbon sheets or cloth and is referred to as gas-diffusion electrode (GDE) [17–19]. The use of either a pure CO_2 gas or a CO_2-water vapor mix stream at the cathode side significantly reduces mass transfer limitations, and demonstrates scalability up to an electrode area of around 800 cm^2 [20].

Anion exchange membranes (AEMs), which supply OH^- ions from the cathode to the anode are predominantly used in zero-gap configurations, because cation exchange membranes (CEMs) and bipolar membranes (BPMs) supply H^+ ions directly to the cathode resulting in an increase of the hydrogen evolution reaction and hence a drop in Faradaic efficiency towards the carbon products [21]. However, due to the poor ion selectivity of AEMs, cations from the anode (e.g., Cs^+ or K^+) can cross over to the cathode, where they react with CO_2 and H_2O to carbonate salts, blocking the CO_2 pathway to the catalyst side over time [22]. Furthermore, crossover of (bi)carbonate anions from the cathode to the anode reduces the passage of OH^- ions, resulting in a shift in water oxidation towards the formation of H^+, leading to slow acidification of the recycled anolyte [23, 24]. The (bi)carbonate reacts back to CO_2 in the acidic anolyte, causing CO_2 gassing out from the anode side. Further, liquid products from the cathode can cross over to the anode side [25–28]. Therefore, additional downstream separation steps are required for zero-gap AEM electrolysers [29, 30].

Introducing a liquid catholyte buffer layer between the GDE and the membrane, as depicted in Figure 1.1 c), permits the use of CEMs and BPMs, hence mitigating challenges in terms of salt precipitation and CO_2 crossover, while still maintaining good selectivity towards carbonaceous products (60-90%) [31–33]. Further, the flowing catholyte enables better control of the local reaction environments at the GDE compared to pure gas-phase MEA designs, facilitating ion mass transfer via diffusion, migration, and convection. Nonetheless, the liquid catholyte layer adds resistance to the ion pathways, increasing the required energy input to drive the reaction. Additionally, scaling this reactor type remains challenging due to the risk of flooding the GDE [34–36]. While various solutions have been proposed to mitigate flooding [37–39], this reactor type primarily serves for testing catalysts under industrially relevant conditions [40] and understanding mass transfer phenomena [41, 42].

This brief description on electorolyser designs illustrates that existing designs, which aim to overcome mass transfer limitations, suffer from poor operational stability. Other proposed reactor designs for CO_2 reduction, such as microfluidic flow cells [43], face similar challenges but offer potential through adaptations like gas-liquid Taylor flow, promising efficient mass transfer with a controllable reaction environments [44]. Chapter 2 of this dissertation examines the feasibility of such flow types for electrochemical CO_2 reduction from a theoretical perspective through modelling, while Chapter 3 dives into the experimentally measured performance.

1.4. PERFORMANCE METRICS FOR ELECTROLYSERS

The electrolyser design greatly influences the mass transfer rate and operational stability as discussed in the previous section. Five performance metrics can be identified to asses and compare different electrolyser designs for CO_2 electrolysis: cell potential, current density (reaction rate), Faradaic efficiency (selectivity) towards the desired product, single-pass conversion, and operational stability.

The electrochemical reduction of CO_2 is driven by the potential difference between the cathode and the anode, which is controlled by the applied cell potential (V) through the outer electrical circuit, as shown in Figure 1.2 a). The required potential to drive the reaction is dictated by the thermodynamic cell potential plus kinetic losses associated with the electron transport, mass transport losses associated with the reactant/product transport, and ohmic losses associated with ionic transport. Increasing the applied cell potential typically leads to an increase of supplied electrons to the electrode surface and hence an increase in the reaction rate. The relation between cell potential and reaction rate is given in terms of current density ($i = I/A$) through the Butler-Volmer equation. Ideally the current density increases with an increase of the applied cell potential, as shown for the hydrogen evolution reaction (i_{HER}) in Figure 1.2 b). However, mass transfer limitations can occur such that an an increase in cell potential does not yield any increase in current density: the limiting current density is reached as illustrated for the electrochemical CO_2 reduction (i_{ECO2R}). As discussed in the previous section and illustrated in Figure 1.2 b) the CO_2 reduction reaction and the hydrogen evolution reaction share a similar equilibrium potential, meaning that typically both reactions take place simultaneously at the cathode. Thus, alongside carbonaceous reaction products, hydrogen is often generated as an undesired side product at the cathode, decreasing the

Faradaic efficiency (FE) towards the CO_2 reduction products. The Faradaic efficiency is heavily influenced by the local reaction environment, with the hydrogen evolution reaction being favoured over the CO_2 reduction reaction in an acidic environment and vice versa in a basic environment. Importantly, in a basic environment CO_2 can also react in a buffer reaction with the OH^- ions increasing mass transfer limitations near the electrode. Typically an increase in cell potential and hence current density unavoidably leads to an increase in the local pH due to the formation of OH^- ions during the reduction reaction. Changes in electrolyser design such as adding a catholyte flow chamber as discussed in the previous section can help in controlling the local pH but increase the overall cell voltage due to an increase in the distance the ions need to travel between the anode and cathode.

Economically favourable electrolysers aim for operation at high current densities (>200-300mA cm^{-2}) [45, 46], high Faradaic efficiencies towards desired products (>95%) [46], and low cell potentials (<2-3V) [47] to reduce investment and operational costs. In addition a single-pass conversion of at least 50% is typically indicated to be desirable to reduce separation costs [45]. These values are derived based on techno-economic analysis considering the performance metrics as completely independent from each other. However, naturally an increase in conversion leads to a decrease in selectivity (Faradaic efficiency) and high current densities imply a high cell potential, and vice versa. Chapter 4 of this dissertation dives into the interplay among these performance metrics and their impact on economic feasibility, focusing on a specific reactor design. Operational stability becomes important for scale-up, but is difficult to asses with the available literature data. It is therefore not taken as a direct performance metric in this dissertation.

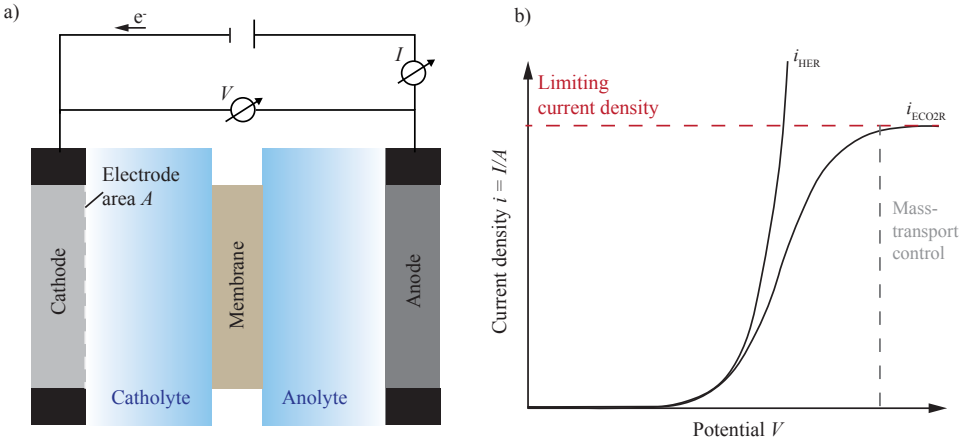

Figure 1.2: Schematic of a CO_2 electrolyser with planar electrodes shown in a). The relation between current density ($i = I/A$) and applied potential (V) is sketched in b), with the partial current density towards hydrogen (i_{HER}) and CO_2 reduction (i_{ECO2R}).

REFERENCES

[1] UNFCCC, *Paris agreement (2015),* (2016).

[2] European Commission and Directorate-General for Climate Action, *Going climate-neutral by 2050 – A strategic long-term vision for a prosperous, modern, competitive and climate-neutral EU economy* (Publications Office, 2019).

[3] G. Hammond and M. Newborough, *Glasgow climate pact: a step on the way towards a lower carbon dioxide world,* Proceedings of the Institution of Civil Engineers - Civil Engineering **175**, 8 (2022).

[4] Z. J. Schiffer and K. Manthiram, *Electrification and decarbonization of the chemical industry,* Joule **1**, 10 (2017).

[5] G. Centi and S. Perathoner, *Chemistry and energy beyond fossil fuels. A perspective view on the role of syngas from waste sources,* Catalysis Today **342**, 4 (2020).

[6] J. L. Holechek, H. M. E. Geli, M. N. Sawalhah, and R. Valdez, *A global assessment: Can renewable energy replace fossil fuels by 2050?* Sustainability **14**, 4792 (2022).

[7] A. Kovač, M. Paranos, and D. Marciuš, *Hydrogen in energy transition: A review,* International Journal of Hydrogen Energy **46**, 10016 (2021).

[8] F. Montagnaro, *Biomass gasification for energy production,* in *Sustainable energy production using solid materials* (Springer Nature Switzerland, 2024) pp. 125–142.

[9] G. Berndes, *Bioenergy and water—the implications of large-scale bioenergy production for water use and supply,* Global Environmental Change **12**, 253 (2002).

[10] R. Chetty, S. Varjani, G. Keerthiga, S. Srinath, and K. S. Rajmohan, *Electrochemical reduction of carbon dioxide into useful low-carbon fuels,* in *CO_2 Separation, Purification and Conversion to Chemicals and Fuels*, edited by F. Winter, R. A. Agarwal, J. Hrdlicka, and S. Varjani (Springer Singapore, 2019) pp. 119–151.

[11] Nederlandse Organisatie voor Wetenschappelijk Onderzoek (NWO), *Electrons to chemical bonds,* `https://www.e2cb.nl` (2022), accessed: 11th of April 2024.

[12] P. Lobaccaro, M. R. Singh, E. L. Clark, Y. Kwon, A. T. Bell, and J. W. Ager, *Effects of temperature and gas–liquid mass transfer on the operation of small electrochemical cells for the quantitative evaluation of CO_2 reduction electrocatalysts,* Physical Chemistry Chemical Physics **18**, 26777 (2016).

[13] Y. Hori, *Electrochemical CO_2 reduction on metal electrodes,* in *Modern Aspects of Electrochemistry*, edited by C. G. Vayenas, R. E. White, and M. E. Gamboa-Aldeco (Springer New York, 2008) pp. 89 – 189.

[14] Vass, Ádám and Kormányos, Attila and Kószó, Zsófia and Endrődi, Balázs and Janáky, Csaba, *Anode catalysts in CO_2 electrolysis: Challenges and untapped opportunities,* ACS Catalysis **12**, 1037 (2022).

[15] S. Nitopi, E. Bertheussen, S. B. Scott, X. Liu, A. K. Engstfeld, S. Horch, B. Seger, I. E. L. Stephens, K. Chan, C. Hahn, J. K. Nørskov, T. F. Jaramillo, and I. Chorkendorff, *Calculation for the cathode surface concentrations in the electrochemical reduction of CO_2 in $KHCO_3$ solutions,* Journal of Applied Electrochemistry **36**, 161 (2006).

[16] T. Burdyny and W. A. Smith, *CO_2 reduction on gas-diffusion electrodes and why catalytic performance must be assessed at commercially-relevant conditions,* Energy and Environmental Science **12**, 1442 (2019).

[17] S. Verma, B. Kim, H.-R. M. Jhong, S. Ma, and P. J. A. Kenis, *A gross-margin model for defining technoeconomic benchmarks in the electroreduction of CO_2,* ChemistrySustainability-Energy-Materials **9**, 1972 (2016).

[18] S. Garg, M. Li, A. Z. Weber, L. Ge, L. Li, V. Rudolph, G. Wang, and T. E. Rufford, *Advances and challenges in electrochemical CO_2 reduction processes: An engineering and design perspective looking beyond new catalyst materials,* Journal of Materials Chemistry A **8**, 1511 (2020).

[19] C. P. O'Brien, R. K. Miao, A. Shayesteh Zeraati, G. Lee, E. H. Sargent, and D. Sinton, *CO_2 electrolyzers,* Chemical Reviews **124**, 3648 (2024).

[20] J. P. Edwards, T. Alerte, C. P. O'Brien, C. M. Gabardo, S. Liu, J. Wicks, A. Gaona, J. Abed, Y. C. Xiao, D. Young, A. Sedighian Rasouli, A. Sarkar, S. A. Jaffer, H. L. MacLean, E. H. Sargent, and D. Sinton, *Pilot-scale CO_2 electrolysis enables a semi-empirical electrolyzer model,* ACS Energy Letters **8**, 2576 (2023).

[21] J.-B. Vennekoetter, R. Sengpiel, and M. Wessling, *Beyond the catalyst: How electrode and reactor design determine the product spectrum during electrochemical CO_2 reduction,* Chemical Engineering Journal **364**, 89 (2019).

[22] M. Sassenburg, M. Kelly, S. Subramanian, W. A. Smith, and T. Burdyny, *Zero-gap electrochemical CO_2 reduction cells: Challenges and operational strategies for prevention of salt precipitation,* ACS Energy Letters **8**, 321 (2023).

[23] M. Ma, E. L. Clark, K. T. Therkildsen, S. Dalsgaard, I. Chorkendorff, and B. Seger, *Insights into the carbon balance for CO_2 electroreduction on Cu using gas diffusion electrode reactor designs,* Energy & Environmental Science **13**, 977 (2020).

[24] J. Rabinowitz and M. Kanan, *The future of low-temperature carbon dioxide electrolysis depends on solving one basic problem,* Nature Communications **11**, 5231 (2020).

[25] J. J. Kaczur, H. Yang, Z. Liu, S. D. Sajjad, and R. I. Masel, *Carbon dioxide and water electrolysis using new alkaline stable anion membranes,* Frontiers in Chemistry **6**, 1 (2018).

[26] G. O. Larrazábal, P. Strøm-Hansen, J. P. Heli, K. Zeiter, K. T. Therkildsen, I. Chorkendorff, and B. Seger, *Analysis of mass flows and membrane cross-over in CO_2 reduction at high current densities in an MEA-type electrolyzer,* ACS Applied Materials & Interfaces **11**, 41281 (2019).

[27] Y. C. Li, Z. Yan, J. Hitt, R. Wycisk, P. N. Pintauro, and T. E. Mallouk, *Bipolar membranes inhibit product crossover in CO_2 electrolysis cells,* Advanced Sustainable Systems **2**, 1700187 (2018).

[28] J. Zhang, W. Luo, and A. Züttel, *Crossover of liquid products from electrochemical CO_2 reduction through gas diffusion electrode and anion exchange membrane,* Journal of Catalysis **385**, 140 (2020).

[29] T. Moore, D. I. Oyarzun, W. Li, T. Y. Lin, M. Goldman, A. A. Wong, S. A. Jaffer, A. Sarkar, S. E. Baker, E. B. Duoss, and C. Hahn, *Electrolyzer energy dominates separation costs in state-of-the-art CO_2 electrolyzers: Implications for single-pass CO_2 utilization,* Joule **7**, 782 (2023).

[30] M. Heßelmann, H. Minten, T. Geissler, R. G. Keller, A. Bardow, and M. Wessling, *Why membranes matter: Ion exchange membranes in holistic process optimization of electrochemical CO_2 reduction,* Advanced Sustainable Systems **7**, 2300077 (2023).

[31] T. Haas, R. Krause, R. Weber, M. Demler, and G. Schmid, *Technical photosynthesis involving CO_2 electrolysis and fermentation,* Nature Catalysis **1**, 32 (2018).

[32] K. Xie, R. Miao, A. Ozden, L. Shijie, C. Zhu, D. Cao-Thang, H. Jianan Erick, X. Qiucheng, G. Christine M., L. Geonhui, E. Jonathan P., O. Colin P., B. Shannon W., S. David, and S. Edward H., *Bipolar membrane electrolyzers enable high single-pass CO_2 electroreduction to multicarbon products,* Nature Communications **13**, 3609 (2022).

[33] B. De Mot, J. Hereijgers, N. Daems, and T. Breugelmans, *Insight in the behavior of bipolar membrane equipped carbon dioxide electrolyzers at low electrolyte flowrates,* Chemical Engineering Journal **428**, 131170 (2022).

[34] L. M. Baumgartner, C. I. Koopman, A. Forner-Cuenca, and D. A. Vermaas, *Narrow pressure stability window of gas diffusion electrodes limits the scale-up of CO_2 electrolyzers,* ACS Sustainable Chemistry & Engineering **10**, 4683 (2022).

[35] K. Yang, R. Kas, W. A. Smith, and T. Burdyny, *Role of the carbon-based gas diffusion layer on flooding in a gas diffusion electrode cell for electrochemical CO_2 reduction,* ACS Energy Letters **6**, 33 (2021).

[36] L. M. Baumgartner, A. Goryachev, C. I. Koopman, D. Franzen, B. Ellendorff, T. Turek, and D. A. Vermaas, *Electrowetting limits electrochemical CO_2 reduction in carbon-free gas diffusion electrodes,* Energy Advances **2**, 1893 (2023).

[37] B. De Mot, J. Hereijgers, M. Duarte, and T. Breugelmans, *Influence of flow and pressure distribution inside a gas diffusion electrode on the performance of a flow-by CO_2 electrolyzer,* Chemical Engineering Journal **378**, 122224 (2019).

[38] M. Großeheide, D. Schaffeld, R. Keller, and M. Wessling, *A falling film design for electrochemical CO_2 reduction,* Electrochemistry Communications **150**, 107487 (2023).

[39] L. M. Baumgartner, C. I. Koopman, A. Forner-Cuenca, and D. A. Vermaas, *When flooding is not catastrophic-woven gas diffusion electrodes enable stable CO_2 electrolysis,* ACS Applied Energy Materials **5**, 15125 (2022).

[40] M. Sassenburg, R. de Rooij, N. T. Nesbitt, R. Kas, S. Chandrashekar, N. J. Firet, K. Yang, K. Liu, M. A. Blommaert, M. Kolen, D. Ripepi, W. A. Smith, and T. Burdyny, *Characterizing CO_2 reduction catalysts on gas diffusion electrodes: Comparing activity, selectivity, and stability of transition metal catalysts,* ACS Applied Energy Materials **5**, 5983 (2022).

[41] L.-C. Weng, A. T. Bell, and A. Z. Weber, *Modeling gas-diffusion electrodes for CO_2 reduction,* Physical Chemistry Chemical Physics **20**, 16973 (2018).

[42] R. Kas, A. G. Star, K. Yang, T. Van Cleve, K. C. Neyerlin, and W. A. Smith, *Along the channel gradients impact on the spatioactivity of gas diffusion electrodes at high conversions during CO_2 electroreduction,* ACS Sustainable Chemistry & Engineering **9**, 1286 (2021).

[43] K. Wu, E. Birgersson, B. Kim, P. J. A. Kenis, and I. A. Karimi, *Modeling and experimental validation of electrochemical reduction of CO_2 to CO in a microfluidic cell,* Journal of The Electrochemical Society **162**, F23 (2014).

[44] F. Zhang, C. Chen, Y. Tang, and Z. Cheng, *CO_2 reduction in a microchannel electrochemical reactor with gas-liquid segmented flow,* Chemical Engineering Journal **392**, 124798 (2020).

[45] M. Jouny, W. Luc, and F. Jiao, *General techno-economic analysis of CO_2 electrolysis systems,* Industrial and Engineering Chemistry Research **57**, 2165 (2018).

[46] M. G. Kibria, J. P. Edwards, C. M. Gabardo, C.-T. Dinh, A. Seifitokaldani, D. Sinton, and E. H. Sargent, *Electrochemical CO_2 reduction into chemical feedstocks: From mechanistic electrocatalysis models to system design,* Advanced Materials **31**, 1807166 (2019).

[47] R. Masel, Z. Liu, H. Yang, J. J. Kaczur, D. Carrillo, R. Shaoxuan, D. Salvatore, and C. P. Berlinguette, *An industrial perspective on catalysts for low-temperature CO_2 electrolysis,* Nature Nanotechnology **16**, 118–128 (2021).

2

ELECTROCHEMICAL REDUCTION OF CO_2 IN TUBULAR FLOW CELLS UNDER GAS-LIQUID TAYLOR FLOW

This chapter has been published in ACS Sustainable Chemistry & Engineering **10**, 38 (2022) [1].

Electrochemical reduction of CO_2 using renewable energy is a promising avenue for sustainable production of bulk chemicals. However, CO_2 electrolysis in aqueous systems is severely limited by mass transfer leading to low reactor performance insufficient for industrial application. This paper shows that structured reactors operated under gas-liquid Taylor flow can overcome these limitations and significantly improve reactor performance. This is achieved by reducing the boundary layer for mass transfer to the thin liquid film between the CO_2 bubbles and the electrode. This work aims to understand the relationship between process conditions, mass transfer, and reactor performance by developing an easy-to-use analytical model. We find that the film thickness and the volume ratio of CO_2/electrolyte fed to the reactor significantly affect the current density and the Faradaic efficiency. Additionally, we find industrially relevant performance when operating the reactor at elevated pressure beyond 5 bar. We compare our predictions with numerical simulations based on the unit cell approach, showing good agreement for a large window of operation conditions, illustrating when the easy-to-use predictive expressions for the current density and Faradaic efficiency can be applied.

2.1. INTRODUCTION

Introducing waste CO_2 as a feedstock for the production of base chemicals can close the carbon cycle and reduce the use of fossil resources [2, 3]. When powered by renewable electricity, the electrochemical conversion of CO_2 further enables the first steps towards the energy transition [4, 5]. The feasibility of this process has been demonstrated at lab scale, notably through impressive advances in catalyst development. However, the main challenge to reach commercialisation is imposed by mass transport limitations [6–8]. A strategy to enhance mass transfer is to actively introduce CO_2 as a gas flow while keeping diffusion paths between reactants and catalyst short by separating the gas flow from the liquid electrolyte through a gas diffusion electrode [7, 9–12]. However, flooding, salt formation, or drying out of the gas diffusion electrode are common problems and present a major obstacle towards commercialisation [13–16].

A promising reactor concept that enhances mass transfer without a gas diffusion electrode is a zero-gap membrane reactor operated under gas-liquid Taylor flow [17, 18]. A key feature of this flow type is the thin liquid film between the elongated bubbles and the electrode surface, see Figure 2.1 (a). This film is orders of magnitude thinner than the boundary layer for mass transfer in, for example, an H-cell in which CO_2 is fed by bubbling it through a static electrolyte, see Figure 2.1 (b). Reducing this boundary layer to the thin liquid film between the CO_2 bubbles and the electrode increases the resulting current density by orders of magnitude. While this is a proven concept for heterogeneous catalysis in flow cells with the catalyst coated on the wall [17–19], literature on this approach for electrochemical processes is scarce. First evidence was reported by Zhang et al. [20, 21], who demonstrated a general increase in activity and selectivity towards CO_2 in an electrolyser operated under gas-liquid Taylor flow. Contrary to the literature on heterogeneous catalysis, they primarily attributed the enhancing effect to the mass transfer inside the liquid slugs rather than to the mass transfer inside the thin liquid film around the bubbles. While the experimental demonstration is encouraging, a key step forward is understanding the mechanisms responsible for enhancing mass transfer in electrolysers operated under Taylor flow. Ideally, the insights are translated into an easy-

to-use relation between experimental conditions and reactor performance.

In this work, we propose a tubular cell design, inspired by the field of fuel cells [22, 23], for CO_2 electrolysis with a zero-gap membrane electrode assembly and develop a numerical model to reveal how reactor performance in terms of Faradaic efficiency and current density is governed by the key features of Taylor flow such as film thickness, bubble velocity, and volume fraction of CO_2 bubbles over aqueous electrolyte, for a given cathode potential. Based on these insights, we reveal the primary mechanism responsible for mass transfer enhancement and develop easy-to-use analytical relations to evaluate Faradaic efficiency and current density for parameters known a priori. We show that these relations are accurate within 10 - 15 % for a wide range of operating parameters by direct comparison to the full numerical simulations. For the reader interested in the main results, we structured the paper such that we directly provide the derived easy-to-use analytical relations for the reactor performance in terms of current density and Faradaic efficiency, followed by an illustration of the performance for one exemplary system. After that, we present the numerical model and validation. We believe that the easy-to-use analytical relations between operating parameters and reactor performance parameters offer a valuable tool to guide reactor design and experimental studies for electrochemical conversion.

2.2. SUMMARY OF MAIN RESULTS

To illustrate how operation under Taylor flow enhances the performance of electrochemical reactors, we consider an exemplary system: The reduction of CO_2 to CO in the tubular cell design shown in Figure 2.1 (a), with the inner and outer channel separated by a circular membrane electrode assembly. Liquid catholyte and gaseous CO_2 bubbles flow through the inner channel as Taylor flow, while liquid anolyte flows through the outer channel (Figure 2.7 appendix). For simplicity, we consider that CO and H_2 are the sole two reduction products. In practice, high selectivity's towards these products are achieved by preparing the membrane electrode assembly with silver catalyst particles [24, 25] (see Section 2.A). Therefore, we consider only the mass transfer limited CO_2 reduction reaction towards CO and the concentration-independent reduction of water towards H_2

$$CO_2 + H_2O + 2\,e^- \longrightarrow CO + 2\,OH^-, E^0_{CO} = -0.11\,V \tag{2.1}$$

$$2\,H_2O + 2\,e^- \longrightarrow H_2 + 2\,OH^-, E^0_{H_2} = 0\,V. \tag{2.2}$$

These reactions are driven by applying a fixed potential (E_c) at the cathode. For simplicity, we consider an electrolyte with a high buffer capacity (e.g. 1 M $KHCO_3$), such that local changes in pH can be safely neglected.

The analytical relation between two key reactor performance parameters, the Faradaic efficiency and the current density, and operating parameters are introduced for this exemplary system, with all relevant symbols summarised in Table 3.1 (appendix). The reactor performance enhancement under Taylor flow is then illustrated for a set of prototypical operating parameters based on the presented analytical relations. This illustration is followed by validating the analytical model against the full numerical model.

2.2.1. EASY-TO-USE ANALYTICAL RELATIONS

The Faradaic efficiency towards CO (FE_{CO}) gives the amount of current driving the desired reduction towards CO over the overall current [26–28]

$$FE_{CO} = \frac{i_{CO}}{i_{CO} + i_{H_2}}, \tag{2.3}$$

with i_{CO} and i_{H_2} the current densities for CO and H_2 respectively. The current density for a mass transfer limited species (CO_2 in the here considered exemplary system) equals [29]

$$i_{CO} = 2Fk_{ov,CO_2}c^*_{CO_2}\frac{Da(\eta_{COER})}{1+Da(\eta_{COER})}, \tag{2.4}$$

with Faraday's coefficient F, mass transfer coefficient k_{ov,CO_2} under Taylor flow, the saturation concentration of CO_2 in the catholyte $c^*_{CO_2}$, which can be determined based on Henry's law and the Sechenov equation. Additionally $Da(\eta_{COER})$ is the Damköhler number for the reduction reaction of CO_2, which progresses at a rate that depends on the activation overpotential. The activation overpotential η_{COER} is given by the applied cathode potential (E_c) as follows

$$\eta_{COER} = E_c - (E^0_{CO} - 0.059\text{pH}), \tag{2.5}$$

with the standard electrode potential E^0_{CO} as given in Eq. 1. The overpotential for the hydrogen evolution reaction (HER) is described similarly with $E^0_{H_2}$ as given in Eq. 2. Inspired by the insights developed on heterogeneous catalysis under Taylor flow [17], the mass transfer coefficient k_{ov,CO_2} for electrochemical conversion of CO_2 under Taylor flow

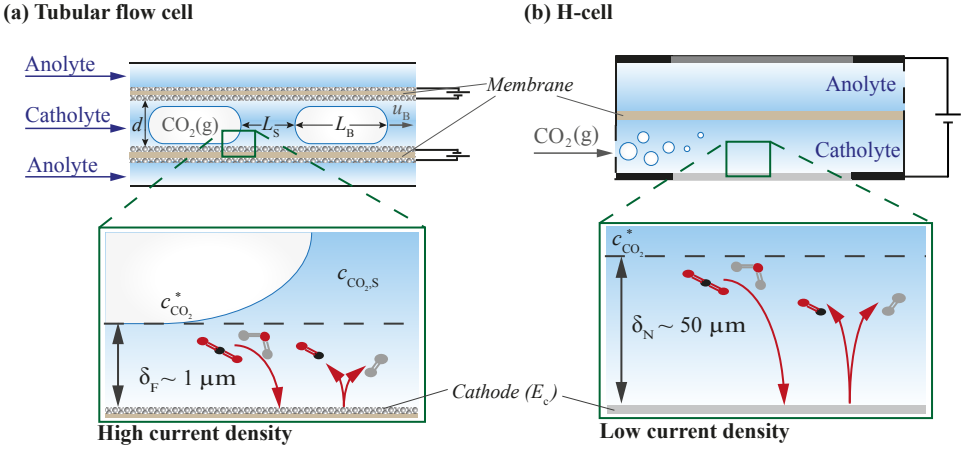

Figure 2.1: Schematic of a tubular flow cell operated under gas-liquid Taylor flow (a) and an H-cell with static electrolyte and a continuous inflow of gaseous CO_2 at the cathode chamber (b). The enlarged regions show mass transfer limitations indicated as diffusion layer thicknesses in these systems (film thickness δ_F and Nernst diffusion layer thickness δ_N).

can be written as

$$k_{ov,CO_2} = \frac{D_{CO_2}}{\delta_F}\left(\frac{L_B - d}{L_S + L_B} + \frac{L_S + d}{L_S + L_B}\frac{c_{CO_2,S}}{c^*_{CO_2}}\right), \tag{2.6}$$

with D_{CO_2} the diffusion coefficient of dissolved CO_2 in the catholyte, L_S the length of the slug, L_B the length of the bubble, and d the tubular diameter (see Figure 2.1 (a)). The film thickness [30]

$$\frac{\delta_F}{d} = \frac{0.66Ca^{2/3}}{1 + 3.33Ca^{2/3}}, \tag{2.7}$$

depends on viscous and capillary forces as captured by the Capillary number Ca. The Capillary number is defined as $Ca = (\mu u_B)/\gamma$ with u_B the velocity of the bubbles, μ the viscosity of the catholyte and γ the interfacial tension between the CO_2 bubbles and liquid catholyte. The concentration of CO_2 in the liquid slugs $c_{CO_2,S}$ is

$$\frac{c_{CO_2,S}}{c^*_{CO_2}} = \left(1 + \frac{L_S + d}{\delta_F}\sqrt{\frac{D_{CO_2}\pi}{8 d u_B}}\frac{Da(\eta_{COER})}{1 + Da(\eta_{COER})}\right)^{-1}, \tag{2.8}$$

where the Damköhler number is defined based on the reaction rate of the reduction reaction of CO_2 to CO (see Section 2.B). The reaction rate is described by Butler-Volmer kinetics [29],

$$Da(\eta_{COER}) = \frac{i_{0,COER}}{2Fc^*_{CO_2}} \times \exp\left(\frac{-\alpha_{COER}F}{RT}\eta_{COER}\right)\frac{\delta_F}{D_{CO_2}}, \tag{2.9}$$

with D_{CO_2}/δ_F the inverse of the mass transfer based on film theory, $i_{0,COER}$ the exchange current density, α_{COER} the cathodic charge transfer coefficient, R the universal gas constant, and T the temperature.

The above expressions (Eq. 2.3 – 2.9) form a complete set that allows straightforward calculation of the current density of CO. The current density of H_2, the species that is considered not to present mass transfer limitations, immediately follows from Butler-Volmer kinetics

$$i_{H_2} = -i_{0,HER}\exp\left(\frac{-\alpha_{HER}F}{RT}\eta_{HER}\right), \tag{2.10}$$

with the kinetic constants $i_{0,HER}$ and α_{HER} and the overpotential η_{HER} (see Eq. 2.5). The two key reactor performance parameters, the Faradaic efficiency towards CO (FE_{CO}) and the current density for CO (i_{CO}), can now be straightforwardly evaluated using Eq. 2.3 - 2.10, in which we introduced the Taylor flow specific behaviour in the general electrochemistry framework through the mass transfer coefficient (Eq. 2.6) and the concentration in the slugs (Eq. 2.8).

2.2.2. PERFORMANCE ENHANCEMENT UNDER TAYLOR FLOW

To illustrate the reactor performance under Taylor flow, we consider the prototypical operating parameters: CO_2 bubbles flowing through the central tube with a diameter of $d = 1\,mm$ at a velocity of $u_B = 10\,mm\,s^{-1}$, resulting in a thin film around the bubbles with a thickness of $\delta_F = 1.6\,\mu m$ (see Eq. 2.7). We further consider the gaseous CO_2 bubbles to occupy a fraction $\beta_g = V_B/(V_B + V_S) \approx (L_B - d/3)/(L_B + L_S) = 0.75$ of the channel volume.

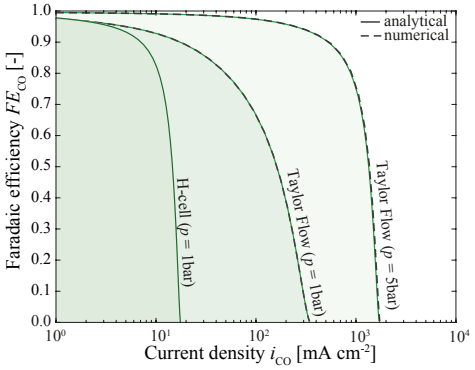

Figure 2.2: Map of reactor performance as current density and Faradaic efficiency towards CO, determined by the easy-to-use analytical relations (solid lines) and the full numerical model (dashed lines) for the prototypical operating conditions (d = 1 mm, u_B = 10 mm s^{-1}, β_g = 0.75) at 1 and 5 bar. The reactor performance for larger u_B, larger d, and smaller β_g lies underneath the lines in the green highlighted areas.

The length of bubble and slug are considered equal to $L_B + L_S = 5d$. Using these prototypical operating parameters, and the electrochemical/fluid properties listed in Table 2.3 (appendix), including the saturation concentration of CO_2 in a 1 M $KHCO_3$ electrolyte at a pressure of 1 bar and ambient temperature ($c^*_{CO_2} \approx 24\,\mathrm{mol\,m^{-3}}$), we calculated FE_{CO} and i_{CO} for a range of cathode potentials (E_c = -0.6 to -3.0 V vs SHE) using Eqs. 2.3 - 2.10. The chosen potential range allows to study the reactor performance of the tubular Taylor flow reactor under mass transfer limitation, a regime in which the hydrogen evolution reaction fully overtakes the CO_2 reduction reaction. The reactor performance of an H-cell can similarly be predicted by assuming (1) film theory for the mass transfer coefficient in Eq. 2.4

$$k_{ov,CO_2} = \frac{D_{CO_2}}{\delta_N}, \tag{2.11}$$

with $\delta_N \approx 50\,\mu m$ [31] and (2) replacing δ_F in Eq. 2.9 by δ_N. Figure 2.2 shows the predicted reactor performance in terms of FE_{CO} and i_{CO} for the H-cell and tubular Taylor flow reactor under ambient pressure for the prototypical operating parameters (solid lines). The x-axis intersect of the solid lines directly gives the mass transfer related reactor performance metric: Limiting current density. Comparing this metric for the H-cell and Taylor flow reveals that the reactor performance can be increased by an order of magnitude under Taylor flow. This increase is mainly attributed to the decrease in diffusion layer thickness. We evaluated the reactor performance for the range of operating parameters shown in Table 2.1. For u_B and d larger and β_g smaller than the prototypical operating parameters, the performance lies underneath the solid lines in the green highlighted areas. The reactor performance range can further be increased to compete with industrially required current densities and Faradaic efficiencies by operating under elevated pressure, e.g. to 5 bar. This increase is understood by the increase in solubility of CO_2 in the liquid electrolyte ($c^*_{CO_2} \approx 120\,\mathrm{mol\,m^{-3}}$), which enhances the availability of CO_2 at the electrode [32–34].

Table 2.1: Range of operating parameters used to test the validity of the easy-to-use analytical relations against full numerical simulations.

Symbol	Range	Unit	Label (Fig. 2.3)
d	1 - 3	mm	□ - ◊
u_B	0.01 - 0.3	$m\,s^{-1}$	green - black
β_g	0.25 - 0.75	-	empty - filled

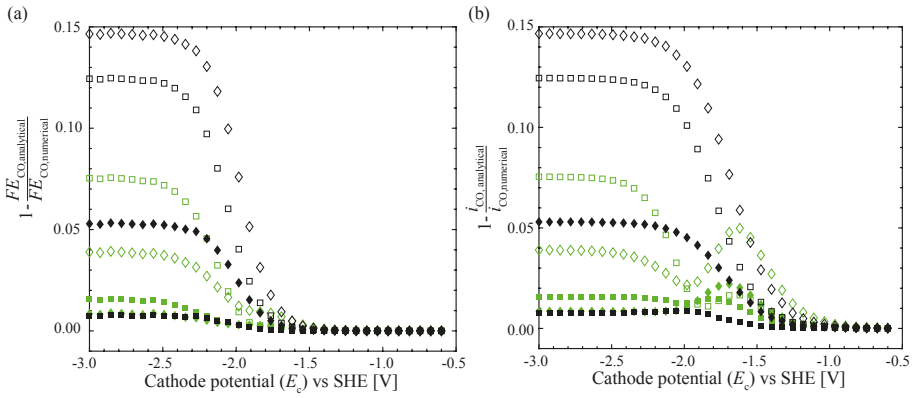

Figure 2.3: Comparison of the Faradaic efficiency (a) and current density (b) calculated with the easy-to-use analytical relations (Eq. 2.3 - 2.10) and the full numerical model over the upper and lower bound of the range of operating parameters listed in Table 2.1 and electrochemical/fluid properties listed in Table 2.3 (appendix). The filled, green squares represent the prototypical operating parameters for Taylor flow at 1 bar shown in Figure 2.2, all other symbols are summarized in Table 2.1

2.2.3. VALIDATION OF ANALYTICAL SOLUTION

To test the validity of the easy-to-use analytical relations (Eq. 2.3 - 2.10) in predicting the reactor performance for operation under Taylor flow, we compare the prediction of the easy-to-use relations with full numerical simulations. For the prototypical operating parameters, the easy-to-use analytical relations (solid lines in Figure 2.2) are in excellent agreement with the full numerical simulations (dashed lines). To test the validity of the easy-to-use analytical relations, we consider a wide range of operating parameters (at ambient pressure and temperature), see Table 2.1. This range is taken from Berčič and Pintar[35], because the range of capillary diameters overlaps with common channel dimensions for tubular fuel cells [22]. Figure 2.3 shows that the analytical relations predict the reactor performance within 15 % for the studied parameter range. The limit of the analytical model, as derived in Section 2.C, can be expressed as

$$Pe\frac{\delta_F}{L_B - d - 2\delta_F} < 1, \tag{2.12}$$

with the Péclet number Pe, which relates convective to diffusive transport. The limit is met for low bubble velocities (black symbols in Figure 2.3), which reduces the relative error to less than 8 %. It is further evident that the analytical model's accuracy increases for high void fractions and strongly increases for low bubble velocities (see also Figure 2.8 (appendix)).

2.3. FULL MODEL AND MECHANISTIC INSIGHTS

The numerical modelling of the hydrodynamics and mass transfer of Taylor flow in a unit cell approach [36] is well-documented in literature [19, 37–40]. Therefore, only this study's relevant geometrical Taylor flow parameters (Table 2.4 appendix) and assumptions are briefly described here, with all relevant equations and fluid/electrochemical properties summarized in Section 2.C. This approach allows for a systematic variation of the operating parameters and analysis of the mass transport limitations, providing the necessary mechanistic insights into the contribution of the operating parameters on the reactor performance.

2.3.1. FULL NUMERICAL MODEL

The hydrodynamics and species transport with an electrochemical wall reaction are numerically solved for the cathode department in a two-dimensional radial coordinate system following the unit cell approach, as shown in Figure 2.4. The model is solved steady-state, axisymmetrical and in the reference frame of the bubble. The dimensionless governing equations are listed in Table 2.5 (appendix), with the boundary conditions based on the work by van Baten et. al [37], see Table 2.6 (appendix). The bubble shape is assumed to be non-deformable [41–44] (most accurate for $Ca \leq 10^{-3}$), allowing for the assumption of hemispherical bubble caps connected by a cylinder. In addition, by neglecting viscous effects at the bubble interface, it is sufficient to solely compute the liquid flow with a slip boundary condition at the bubble interface. Eq. 2.7 describes the uniform thickness of the lubrication film between bubble and wall. The flow velocities are chosen to fall in the laminar flow regime ($Re < 800$). The validation of the velocity field can be found in Figure 2.9 (appendix).

The dimensionless species balances for CO_2, H_2 and CO are listed as convection-diffusion equations in Table 2.5 (appendix). Similar to the work by Cao *et al.*[44] the electrochemical reduction reaction is assumed to take place at the wall of the channel and is described by Butler-Volmer kinetics (see boundary conditions in Table 2.6 (appendix)). Contrary to their study, in which the cathode and anode are placed on the opposite channel sides with the gas bubbles flowing through the inter-electrode gap, the tubular Taylor flow cell is made of a zero-gap membrane electrode assembly (Figure 2.1 (a)). In this configuration the cathode and anode are sandwiched together with a membrane in between minimising the inter-electrode gap. The CO_2 bubbles and the gas evolving products are therefore solely by-passing the cathode allowing us to neglect the effect of bubbles on the ohmic losses and potential distribution. Additionally, it is assumed that all gaseous products either directly diffuse back into the Taylor bubble or

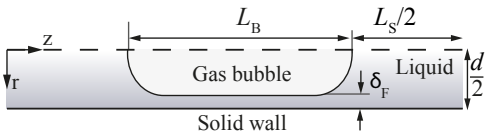

Figure 2.4: Schematic representation of two-dimensional axisymmetrical unit cell showing all relevant parameters.

form small bubbles after leaving the electrode such that local effects of gas evolution can be neglected. Further, it is assumed that the thin catalyst is directly in contact with anion exchange membrane, and a catholyte with a high buffer capacity (e.g. 1 M $KHCO_3$) is used, which leads to ignoring any change in pH and its resulting effect on carbonate crossover (Section 2.E and Figure 2.10 (appendix)). The validation of the predicted mass transfer coefficient can be found in Table 2.7 (appendix).

All two-dimensional unit cell simulations are carried out with the finite element-based software COMSOL Multiphysics 5.6, in which the hydrodynamics are solved decoupled from the species transport. Calculation of the electrolyte dependent parameters, geometrical properties and evaluation of the analytical model equations was carried out in Matlab R2020a. Details regarding the mesh parameters (Table 2.8 and Figure 2.11 (appendix)), mesh independence (Figure 2.12 (appendix)) and solver scheme are given in Section 2.F.

2.3.2. MECHANISTIC INSIGHTS INTO THE MASS TRANSFER UNDER TAYLOR FLOW

To understand the main mechanism responsible for the enhanced reactor performance under Taylor flow, we now consider the limit in which the mass transfer limitations dominate over the reaction kinetics. In this limit, the analytical model is considerably simplified, allowing to quantify the separate contributions of the film and slug region to the mass transfer coefficient (Figure 2.5 (a)). This is achieved at high cathode potentials (-3.0 V vs SHE) that translate into high Damköhler numbers. For $Da >> 1$, Eq. 2.4 simplifies to the limiting current density equation

$$i_{\mathrm{Lim,CO}} = 2F k_{\mathrm{ov,CO_2}} c_{\mathrm{CO_2}}, \tag{2.13}$$

where we introduce $c_{\mathrm{CO_2}}$ as the more generic concentration of CO_2 in the bulk. In the film region, $c_{\mathrm{CO_2}}$ equals the saturation concentration $c^*_{\mathrm{CO_2}}$. In the slug region, $c_{\mathrm{CO_2}}$ equals the average concentration $c_{\mathrm{CO_2,S}}$, which depends on the mass transfer over the caps as described in Eq. 2.8. For high Damköhler [17], it simplifies to $c_{\mathrm{CO_2,S}} = c^*_{\mathrm{CO_2}} \left(1 + (L_S + d_B)/\delta_F \sqrt{D\pi/(8 d u_B)}\right)^{-1}$. Considering Eq. 2.13, with the above expressions for the bulk concentration, together with the mass transfer coefficient based on film theory (Eq. 2.11) allows us to straightforwardly see the role of the operating parameters on the limiting current density. While the current density in the film region solely depends on the film thickness, it additionally depends on the void fraction in the slug region.

In Figure 2.5 (b) and (c), the limiting current density $i_{\mathrm{Lim,CO}}$ calculated with Eq. 2.13 and the full numerical simulations are shown for the film and slug region respectively, for varying dimensionless film thicknesses and three different void fractions. Increasing film thicknesses generally lead to a decrease in the mass transfer coefficient (see Eq. 2.11), which consequently leads to a decrease in current density (see Eq. 2.13). This inversely related dependency between limiting current density and film thickness becomes dominant in the film region (Figure 2.5 (b)). The numerical simulation further displays a slight dependency of limiting current density on void fraction for increasing film thicknesses, which is not captured by the analytical relation. The deviation between analytical relation and numerical model is mostly seen for low void fractions in which

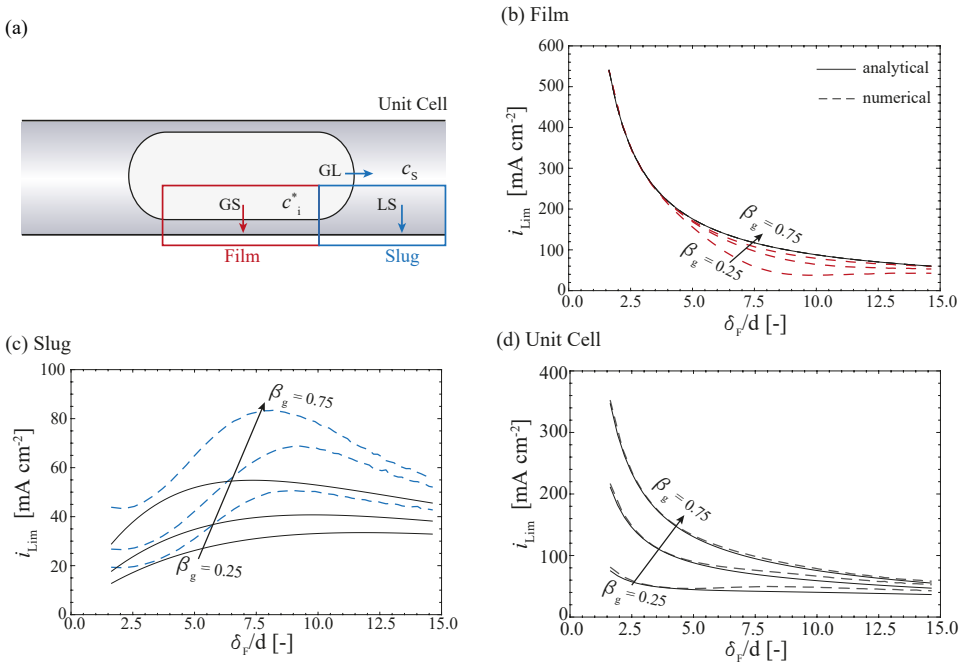

Figure 2.5: Schematic of the unit cell including film and slug region with the respective mass transfer routes (a). The limiting current density for a varying film thickness (Eq. 2.7) for the film region (b), the slug region (c), the unit cell (d).

the assumption of solely diffusive transport in the liquid film fails (see limit of analytical assumption in Eq. 2.12 and Section 2.C). The moderate dependency on film thickness and void fraction in the slug region predicted by Eq. 2.13 are reasonably in line with the full numerical simulations (Figure 2.5 (c)). Deviations between the numerical model and analytical relation are mostly arising from the simplified assumption that the diffusion layer thickness in the slug region equals the film thickness (see Figure 2.13 (appendix)). Importantly, the contribution to the current density from the film region is significantly larger than for the slug region. Only for the higher film thicknesses the contribution of both regions becomes similar (for additional information, see Figure 2.12 (appendix)). Figure 5 (d) shows that the current density for film and slug region together ($i_{\mathrm{Lim,UC}} = i_{\mathrm{Lim,F}}\,(L_B - d)\,/\,L_{\mathrm{Lim,UC}} + i_{\mathrm{Lim,S}}\,(L_S + d)\,/\,L_{\mathrm{Lim,UC}}$) and is well captured by the analytical model.

2.3.3. REACTOR PERFORMANCE UNDER VARYING OPERATING CONDITIONS

We quantified reaction performed in terms of the (limiting) current density and Faradaic efficiency towards CO. An additional representation useful in the light of downstream operations is to describe the performance in terms of the ratio between H_2 and CO_2 in the produced syngas. Figure 2.6 (a) shows the influence of bubble velocity in terms of the film thickness (see Eq. 2.7) on the Faradaic efficiency and H_2 to CO ratio for different

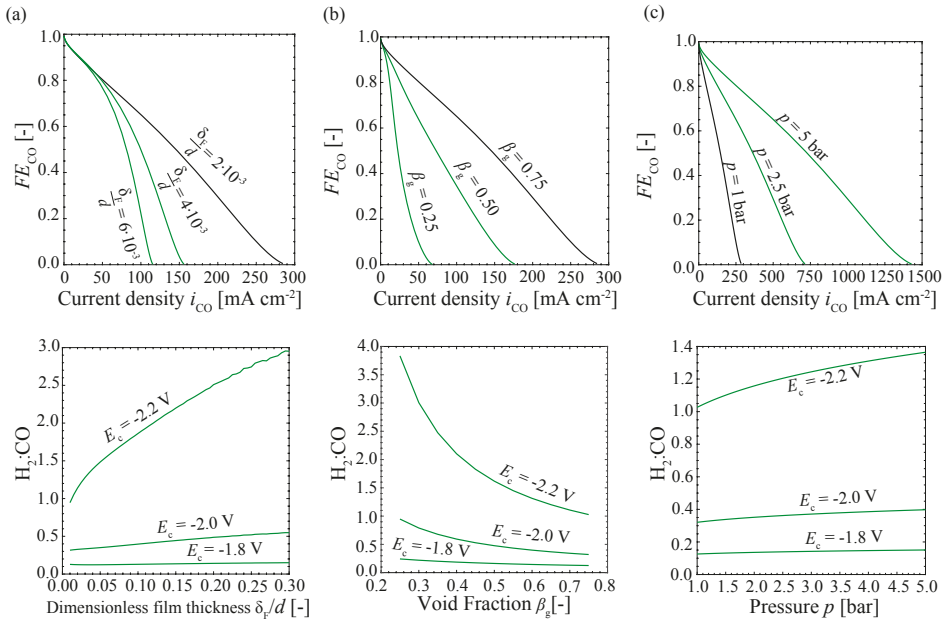

Figure 2.6: Prediction of reactor performance and H_2 to CO ratio with the numerical model for varying film thicknesses (a), void fractions (b) and pressures (c). Black lines in the top figures indicate the same conditions with $d = 1\,\text{mm}$, $u_B = 14\,\text{mm s}^{-1}$ and $\beta_g = 0.75$ at ambient pressure and temperature.

cathode potentials. Similarly to the limiting current density, the Faradaic efficiency decreases non-proportional with increasing the film thickness, leading to a shift in the H_2 to CO ratio towards the formation of H_2. This becomes more prominent under higher applied potentials and is explained by increased mass transfer limitations at high cathode potentials. The bubble velocity and therefore film thickness can be directly controlled by the superficial velocities at the inlet [17] ($u_B \approx u_{gas} + u_{catholyte}$) allowing to easily control the reactor performance.

The void fraction [17] can be varied based on the ratio of superficial velocities $\beta_g \approx \epsilon_g = u_{gas}/u_{gas} + u_{catholyte}$ and its influence on Faradaic efficiency and H_2 to CO ratio is shown in Figure 2.6 (b). Higher void fractions result in longer CO_2 bubbles and shorter electrolyte slugs, leading to an increased film region compared to the slug region. As demonstrated previously, in Figure 2.5, the mass transfer in the film region is an order of magnitude higher than the one in the slug region for low velocities. Therefore, the Faradaic efficiency increases proportionally with increasing the void fraction, shifting the H_2 to CO ratio towards CO.

Apart from varying the superficial velocities the pressure can be increased to change the saturation concentration of CO_2 in the liquid electrolyte and thereby increase the Faradaic efficiency towards CO (Figure 2.6 (c)). Changes in the CO_2 concentration increases the availability of CO_2 and shift the equilibrium of the carbon reaction in the electrolyte according to Le Chatelier's principle, resulting in a slightly more acidic bulk pH. The changes in pH lower the activation potential (Eq. 2.5), leading to higher cur-

rent densities for the same cathode potential at increased pressure [32–34] (Figure 2.13 (appendix)). Therefore, the effect of pressure on the H_2 to CO for the herein shown potentials is comparably lower than the influence of film thickness and void fraction. This implies that pressure is a good way to increase Faradaic efficiencies and reduce the required cell potential, while the superficial velocities present a valuable way to control the H_2 to CO ratio.

2.4. DISCUSSION AND CONCLUSION

We introduced an easy-to-use analytical model to predict the current density and Faradaic efficiency in a tubular flow cell operated under gas-liquid Taylor flow. Comparing the reactor performance to numerical predictions for the electrochemical reduction of CO_2 to CO shows good agreement within the derived limits. Further, we showed that the limiting current density increases by an order of magnitude for the tubular Taylor flow cell compared to an H-cell reactor. The film thickness and void fraction significantly influence the Faradaic efficiency and H_2 to CO ratio. Further, the bubble region is mainly contributing to mass transfer for low velocities suggesting a preference for thin films and high void fractions, while for increasing velocities, the mass transfer becomes region independent. The tubular Taylor flow cell architecture offers a design which can be straightforwardly operated under elevated pressure [45–48] further improving mass transfer to achieve a high Faradaic efficiency (> 90 %) at a current density of up to 500 $mA\,cm^{-2}$, demonstrating the general potential of this reactor concept to overcome mass transfer limitations in the field of electrolysis. With tubular flow cells operated under gas-liquid Taylor flow yet to be explored experimentally in the field of electrolysis, we expect the generic insights into mass transfer and the simple analytical model to provide guidelines for experimental studies and reactor design choices.

Table 2.2: List of symbols.

Symbol	Description	Unit
Latin letters		
A_{GL}	Exchange area for gas-liquid mass transfer	m^2
A_{LS}	Exchange area for liquid-solid mass transfer	m^2
Ca	Capillary number	-
c_{CO_2}	Concentration of CO_2	$mol\,m^{-3}$
$c^*_{CO_2}$	Saturation concentration of CO_2	$mol\,m^{-3}$
$c_{CO_2,S}$	Concentration of CO_2 in the liquid slug	$mol\,m^{-3}$
c_{wall}	Concentration at the wall	$mol\,m^{-3}$
Da	Damköhler number	-
D_i	Diffusion coefficient	$m^2\,s^{-1}$
d	Diameter	m
d_b	Bubble diameter	m
E^0_i	Standard potential	V
E_C	Cathode potential	V
F	Faraday constant	$As\,mol^{-1}$
FE_{CO}	Faradaic efficiency towards CO	V
H^{cp}	Henry coefficient	$mol\,m^{-3}\,Pa^{-1}$
i_i	Exchange current density	$A\,m^{-2}$
J_{GL}	Gas-liquid molar flux	$mol/m^2/s$
J_{LS}	Liquid-solid molar flux	$mol/m^2/s$
k_f	Forward reaction rate constant	$mol^{-1}\,s$
k_{GL}	Gas-liquid mass transfer coefficient	mol/s
k_{LS}	Liquid-solid mass transfer coefficient	mol/s
k_{ov,CO_2}	Overall mass transfer coefficient of CO_2	mol/s
k_r	Backward reaction rate constant	s^{-1}
L_B	Bubble length	m
L_F	Film length	m
L_S	Slug length	m
L_{UC}	Unit cell length	m
p	Pressure	bar
Pe	Peclet number	-
u_B	Bubble velocity	$m\,s^{-1}$
u_{TP}	Two-phase velocity	$m\,s^{-1}$
Greek letters		
α_{COER}	Transfer coefficient of the CO_2 reduction reaction	-
α_{HER}	Transfer coefficient of the hydrogen evolution reaction	-
β_g	Void fraction	-
δ_F	Film thickness	m
δ_N	Nernst diffusion layer thickness	m
η_{COER}	Activation overpotential of the CO_2 reduction reaction	V
η_{HER}	Activation overpotential of the hydrogen evolution reaction	V
γ	Interfacial tension	$N\,m^{-1}$
μ	Dynamic viscosity	$Pa\,s$
ρ	Density	$kg\,m^{-3}$

APPENDIX

2.A. CELL DESIGN

In H-cell configurations, the electrodes are commonly placed with some distance to the membrane, which allows to use either two dimensional electrodes like foils or porous three dimensional electrodes like meshes, felts and papers [49]. In the tubular design the anode and cathode are sandwiched together with a thin polymeric membrane in a zero-gap membrane electrode assembly (MEA) [50]. In this configuration porous electrodes have to be used to allow for the transport of ions and reactants to the catalyst sites. The electrode can then either be made entirely out of the catalyst material, e.g silver meshes or foams or the catalyst material is deposited on an electrical conductive substrate, e.g carbon paper. Several deposition techniques are available while drop-casting, airbrushing and sputtering are widely applied in the field of CO_2 electrolysis [6]. Due to the weak interaction between substrate and catalyst layer these techniques are only limited suitable for tubular flow cells. Therefore, techniques like atomic layer deposition have been proposed in literature for these designs [47]. These techniques can be used to form very thin catalyst layers ($\approx 10\,\text{nm}$)[9, 47].

The cathode in the H-cell could be made of a silver foil, while the cathode in the tubular configuration could be either a silver mesh or a porous transport layer which is coated with silver via atomic layer deposition (ALD). Based on the resulting thin catalyst layer the electrochemical reaction can be assumed to occur at the interface leading to the boundary conditions for the numerical model (Table 2.6). Additionally, to reduce mass transfer limitations for the reactant CO_2 the catalyst layer would be placed close to the bubble interface and the thickness of the supporting substrate minimised to reduce additional ohmic resistance from the transport of ions to the catalyst side (see Figure 2.7).

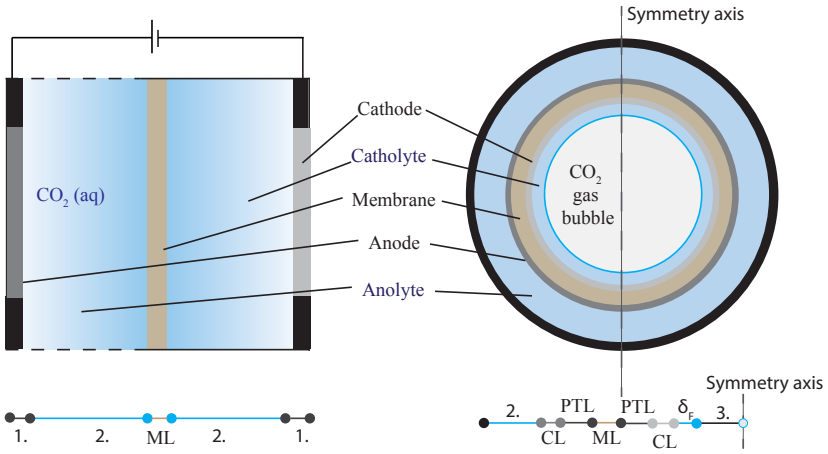

Figure 2.7: Cross sectional view of the H-cell and tubular Taylor flow configuration with the different layers electrode(1.), electrolyte (2.), membrane layer (ML), catalyst layer (CL), porous transport layer (PTL), film thickness (δ_F) and gaseous Taylor bubble (3.) represented by the line beneath each configuration.

2.B. REACTION RATE DEPENDENT CONCENTRATION IN THE LIQUID SLUGS

The mass transfer over the bubble caps (J_{GL}) depends on the concentration difference between the saturation concentration at the gas-liquid interface ($c^*_{CO_2}$) and the concentration in the liquid slugs ($c_{CO_2,S}$) which is assumed well-mixed, the area of the spherical caps (A_{GL}), and the mass transfer with the mass transfer coefficient k_{GL} described by penetration theory as follows [17]

$$J_{GL} = k_{GL} A_{GL} \left(c^*_{CO_2} - c_{CO_2,S} \right) = 2 \cdot 2 \sqrt{\frac{D_{CO_2} d}{\pi 2 u_{TP}}} \frac{1}{2} \pi d^2 \left(c^*_{CO_2} - c_{CO_2,S} \right), \tag{2.14}$$

with the two-phase velocity u_{TP}. The mass transfer (J_{LS}) from the slugs to the channel wall is given by [17]

$$J_{LS} = k_{LS} A_{LS} \left(c_{CO_2,S} - c_{wall} \right) = \frac{D_{CO_2}}{\delta_F} (L_S + d) \pi d \left(c_{CO_2,S} - c_{wall} \right), \tag{2.15}$$

with the mass transfer coefficient k_{LS} described by film theory, and A_{LS} for the circular slug region. Equating the fluxes in Eq. 2.14 and 2.15, and using the reaction diffusion boundary condition that translates into $c_{wall} = c^*_{CO_2} \cdot 1/\left(1 + Da(\eta_{COER})\right)$, we find

$$k_{LS} A_{LS} \left(c_{CO_2,S} - c^*_{CO_2} \frac{1}{1 + Da(\eta_{COER})} \right) = k_{GL} A_{GL} \left(c^*_{CO_2} - c_{CO_2,S} \right). \tag{2.16}$$

Rearranging this equation the ratio of slug concentration over saturation concentration is

$$\frac{c_{CO_2,S}}{c^*_{CO_2}} = \left(1 + \frac{L_S + d}{\delta_F} \sqrt{\frac{D_{CO_2} \pi}{8 d u_B}} \frac{Da(\eta_{COER})}{1 + Da(\eta_{COER})} \right)^{-1}. \tag{2.17}$$

2.C. LIMIT OF THE ANALYTICAL MODEL

The analytical model, as described in the Section "Easy-to-use analytical relations", is based on a stagnant film approach which allows assuming film theory for the mass transfer in the bubble region and implies that the boundary layer for mass transfer equals the film thickness ($\delta = \delta_F$). This assumption is only valid if the convective transport of species in the liquid film is smaller than diffusive transport. Starting from the stationary convection-diffusion equation

$$0 = D \frac{\partial^2 c}{\partial r^2} - u_B \frac{\partial c}{\partial z}, \tag{2.18}$$

with the convective ($u_B \partial c / \partial z$) and diffusive ($D \partial^2 c / \partial r^2$) transport terms, using δ as the characteristic length scale in the radial direction and L_f as the characteristic length scale in the axial direction, we find that the diffusive contribution dominates over the convective contribution when

$$\frac{u_B \delta}{D} \frac{\delta}{L_F} < 1. \tag{2.19}$$

With the characteristic length δ Eq. 2.19 can be rewritten in terms of the Peclét number $Pe = u_B\delta/D$. To arrive at Eq. 12 the length of the liquid film is given as the length of the cylindrical part of the bubble without considering the bubble caps $L_F = L_B - d - 2\delta_F$. It should also be noted that the numerical model does not consider a change in bubble shape, which is expected with increasing velocities. Increasing velocities leads to a flattening out of the rear back of the bubble [17], which can lower the convective transport in the film.

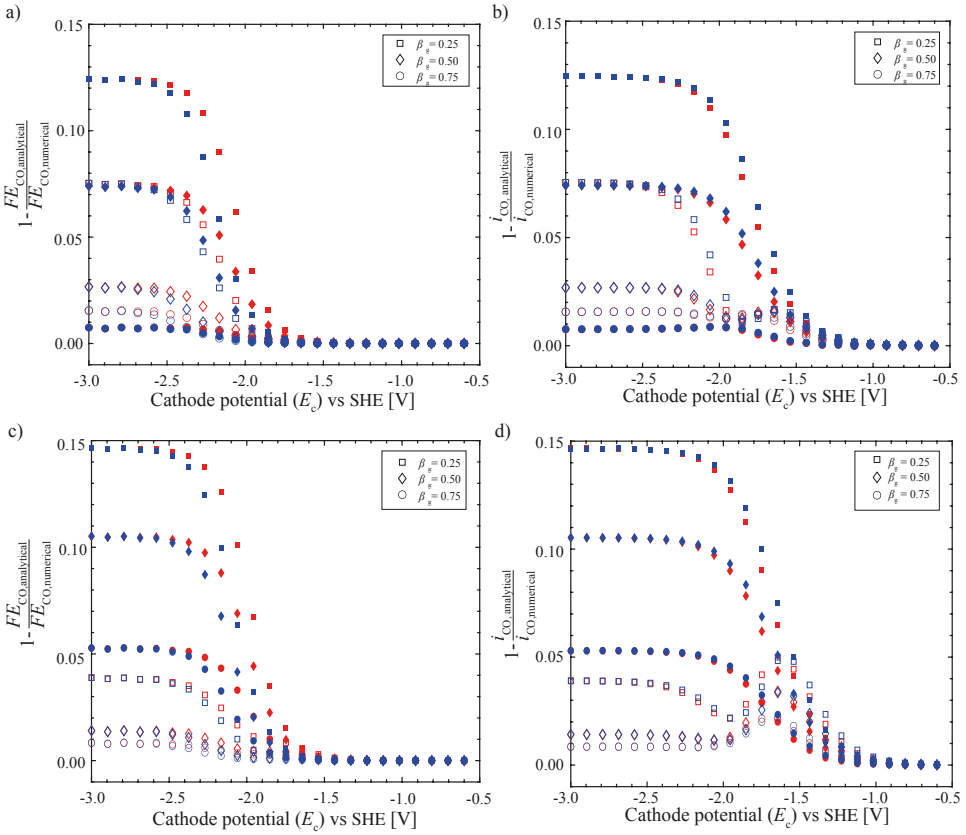

Figure 2.8: Relative error of analytical predictions towards the numerical results for a tube diameter of d = 1 mm (a-b) and of 3 mm (c-d) for three different void fraction β_g. Red corresponding to a pressure of 1 bar and blue to a pressure of 5 bar. Filled symbols $u_B = 0.03\,\mathrm{m\,s^{-1}}$, open symbols $u_B = 0.1\,\mathrm{m\,s^{-1}}$.

2.D. FLUID/ELECTROCHEMICAL PROPERTIES AND MODEL DESCRIPTION

2.D.1. FLUID/ELECTROCHEMICAL PROPERTIES AND PARAMETER LIST

All fluid/electrochemical properties are summarised in Table 2.3.

Table 2.3: List of parameters.

Description	Value	Unit	Reference
Electrolyte (1M $KHCO_3$)			
μ ($T = 20\,^{\circ}\mathrm{C}$, $p = 1\,\mathrm{bar}$)	$1001.6 \cdot 10^{-6}$	$\mathrm{Pa\,s}$	[51]
ρ ($T = 20\,^{\circ}\mathrm{C}$, $p = 1\,\mathrm{bar}$)	998.21	$\mathrm{kg\,m^{-3}}$	[51]
γ ($T = 20\,^{\circ}\mathrm{C}$)	72.74	$\mathrm{N\,m^{-1}}$	[51]
D_{CO_2} ($T = 25\,^{\circ}\mathrm{C}$)	$1.97 \cdot 10^{-9}$	$\mathrm{m^2\,s^{-1}}$	[52]
D_{HCO_3-} ($T = 25\,^{\circ}\mathrm{C}$)	$1.185 \cdot 10^{-9}$	$\mathrm{m^2\,s^{-1}}$	[53]
$D_{CO_3^{2-}}$ ($T = 25\,^{\circ}\mathrm{C}$)	$9.23 \cdot 10^{-10}$	$\mathrm{m^2\,s^{-1}}$	[53]
D_{OH} ($T = 25\,^{\circ}\mathrm{C}$)	$5.293 \cdot 10^{-9}$	$\mathrm{m^2\,s^{-1}}$	[53]
H^{cp} ($T = 25\,^{\circ}\mathrm{C}$)	$3.4 \cdot 10^{-4}$	$\mathrm{mol\,m^{-3}\,Pa^{-1}}$	[54]
Electrochemical reaction			
$i_{0,COER}$	0.1098	$\mathrm{A\,m^{-2}}$	[26]
α_{COER}	0.17	-	[26]
E^0_{COER}	-0.11	V	[26]
$i_{0,HER}$	$4.1439 \cdot 10^{-5}$	$\mathrm{A\,m^{-2}}$	[26]
α_{HER}	0.25	-	[26]
E^0_{HER}	0	V	[26]
Homogeneous reaction			
k_{1f}	2.23	$\mathrm{mol^{-1}\,s}$	[55]
k_{1r}	$1.5494 \cdot 10^{-5}$	$\mathrm{s^{-1}}$	[56]
k_{2f}	$6 \cdot 10^6$	$\mathrm{mol^{-1}\,s}$	[55]
k_{2r}	$4.6821 \cdot 10^4$	$\mathrm{s^{-1}}$	[56]
Unit cell geometry			
d	1 - 3	mm	[57]
u_B	0.01 - 0.3	$\mathrm{m\,s^{-1}}$	[35]
β_g	0.25 - 0.75	-	
p	1 - 5	bar	[33]

2.D.2. TAYLOR FLOW FEATURES

Taylor flow is introduced in the cathode chamber of a tubular zero-gap CO_2 electrolyser. The cathode flow channel in this study is modelled through a unit cell approach with the assumption of axisymmetry and steady-state. It is assumed that due to the periodicity of the flow, a single gas bubble surrounded by a liquid film and separated by two liquid half-slugs on either side, called a unit cell (UC), can be considered a representative of the flow [58]. The bubble's diameter can be determined based on the thickness of the lubrication film (δ_F), which forms around the bubble. The bubble (L_B) and slug (L_S) lengths can be obtained from the unit cell length (L_{UC}) and void fraction (β_g). The unit cell length and void fraction depend on the superficial gas and liquid velocities ratio and the cross junction geometry [59, 60]. Therefore, unit cell length and void fraction are directly used as input parameters to arrive at the modelling domain in this study. The unit cell length is given based on the diameter ($L_{UC} = 5d$), while the void fraction gives how much of this unit cell is occupied by gas as the ratio between the gas bubble volume and unit cell volume ($\beta_g = \frac{V_B}{V_{UC}}$). The resulting slug length for each void fraction as well as the geometry properties are summarised in Table 2.4.

Table 2.4: Taylor flow features for axisymmetric unit cell geometry.

Description	Definition	Unit
Film thickness [30]	$\delta_F = d\frac{0.66Ca^{2/3}}{1+3.33Ca^{2/3}}$	m
Bubble diameter	$d_B = d - 2\delta_F$	m
Film length	$L_F = \frac{d^2}{d_B^2}\beta_g L_{UC} - \frac{2}{3}d_B$	m
Bubble length	$L_B = L_F + d_B$	m
Slug length	$L_S = L_{UC} - L_B$	m

2.D.3. GOVERNING EQUATIONS

The unit cell is described by a bubble moving in a round channel with the diameter d. The modelling domain is, therefore, two dimensional and axisymmetric. Only the liquid phase is modelled, and the bubble shape is assumed to remain constant based on the steady-state unit cell approach, which represents a bubble at a fixed location in the reactor. Nonetheless a change in bubble length and bubble velocity is expected based on the diffusion of CO_2 to the reaction side, comparable to the process of dissolution. However, as in this study the reaction products H_2 and CO are formed, which have a low solubility in the liquid electrolyte and are therefore expected to form gas bubbles, it is not evident how the bubble size and composition change over the reactor length. The single-phase flow is described by solving the incompressible Navier-Stokes equation for laminar flow. Mass transfer is modelled by solving the advection-diffusion equation. The

dimensionless governing equations where we use a * for all dimensionless quantities are summarised in Table 2.5. They were obtained by dividing all lengths with the channel diameter d, and all velocities with the liquid phase velocity which is determined under the assumption of a stagnant film [17] $\frac{u_{TP}}{u_B} = 1 - \frac{4\delta_F}{d}$. All concentrations are scaled with the saturation concentration of CO_2 (c_{CO_2}). These choices lead to the normalisation of the pressure by dividing it by $\mu u_{TP}/d$ and the introduction of the Reynolds number $Re = \rho u_{TP} D/\mu$ and Peclét number $Pe = ud/D$ in the governing equations.

Table 2.5: Dimensionless governing equations.

Mass conservation
$\frac{1}{r^*}\frac{\partial}{\partial r^*}\left(r^* u_r^*\right) + \frac{\partial u_z^*}{\partial z^*} = 0$
Momentum conservation
$Re\left[u^*.\nabla^* u^*\right]_r = -\frac{\partial p^*}{\partial r^*} + \left[\nabla^{2*} u^*\right]_r$
$Re\left[u^*.\nabla^* u^*\right]_z = -\frac{\partial p^*}{\partial z^*} + \left[\nabla^{2*} u^*\right]_z$
Species conservation
$Pe\left[u^*.\nabla^* c_i^*\right]_r = \left[\nabla^{2*} c_i^*\right]_r$
$Pe\left[u^*.\nabla^* c_i^*\right]_z = \left[\nabla^{2*} c_i^*\right]_z$

2.D.4. BOUNDARY CONDITIONS AND ELECTROCHEMICAL MODEL

The simulations are taken in the reference frame of the bubble, therefore, the bubble velocity is set as moving wall, and the Hagen-Poiseuille parabolic velocity profile describes the inflow and outflow [61]. A zero slip condition is applied at the interface of the bubble. For the species transport, the interface between bubble and liquid is treated as a free surface, and the saturation concentration, $c^*_{CO_2}$ is obtained from Henry's law ($c^*_{CO_2} = H_i P_B$) assuming constant pressure inside the bubble. The concentration is then corrected for the electrolyte salinity with the Sechenov equation [62]. At the inlet and outlet, the periodic boundary condition assumes that the concentration and fluxes of species are the same [37, 42]. Finally, to complete the model, an electrochemical wall reaction is imposed. The boundary conditions are summarized in Table 2.6.

The surface reaction rate, $R_i = \frac{\nu i_i}{zF}$, is determined based on the electrochemical Butler-Volmer reaction kinetics. It is assumed that the anodic exponential term becomes negligible compared to the cathodic term at herein studied cathode potentials. This gives the partial current density i_{CO} for the reduction of CO_2 to CO as the concentration-

Table 2.6: Boundary conditions for the numerical unit cell model, with $\hat{z}$ denoting the unit vector in the z direction in similarly in r direction for $\hat{r}$.

Boundary	Hydrodynamics	Species Transport
Inlet	$u^* = \left(2\left(1-4r^{*2}\right) - \frac{u_B}{u_{TP}}\right)\hat{z} + 0\hat{r}$	Periodic Boundary
Outlet	$u^* = \left(2\left(1-4r^{*2}\right) - \frac{u_B}{u_{TP}}\right)\hat{z} + 0\hat{r}, P^* = 0$	Periodic Boundary
Interface	Slip condition, $\frac{\partial u^*}{\partial n^*} = 0$ - Free surface	$c_i^* = \frac{c_i^0}{c_{CO_2}^0}$
Wall	No slip, $u^* = -\frac{u_B}{u_{TP}}\hat{z} + 0\hat{r}$	$\nabla_n^* c_i^* = \frac{R_i(\eta)d}{D_{CO_2} c_{CO_2}^0}$

dependent Butler-Volmer equation

$$i_{CO} = -i_{0,COER}\frac{c_{CO_2,wall}}{c_{ref,CO_2}}\exp\left(\frac{-\alpha_{COER}F}{RT}\eta_{COER}\right), \tag{2.20}$$

while the competing hydrogen evolution reaction (HER) is mass transfer independent (see Eq. 10). The kinetic constants like exchange current density $i_{0,COER}$, cathodic transfer coefficient α_{COER}, and reference concentration c_{ref,CO_2} are taken from the study by Wu [26] and are summarised in Table 2.3.

2.E. VALIDATION

2.E.1. HYDRODYNAMICS

For Taylor flow in circular capillaries, only a small portion of the liquid is transported through the film, while the rest of the fluid circulates between the bubbles creating the well-known vortexes[63]. The vortex centre is the position at which the velocity in the liquid slugs becomes zero. Thulasidas et al. [64] derived the position of the vortex centre from the Hagen-Poiseullie parabolic velocity profile inside the liquid slug

$$r_0 = \frac{d}{2\sqrt{2}}\sqrt{2 - \frac{|u_B|}{|u_{TP}|}}. \tag{2.21}$$

They further conducted experiments to determine the vortex centre as a function of capillary number. The velocity profile inside the liquid slug is validated by comparing the simulation results with the experimental work of Thulasidas et al. [64] and the analytical expression in Figure 2.9. The velocity profile in the film is validated against the theoretical model developed by Abiev [65]. The theoretical model is solved in Matlab to determine the velocity profile inside the liquid film and compared with the hydrodynamic simulations in COMSOL. For this a diameter of 3 mm and a velocity of $0.3\,m\,s^{-1}$ is set. Figure 2.9 shows the expected trend of the plug flow behaviour for the theoretical velocity profile, while the numerical simulation slightly deviates from this. This is similar to the results by Martínez et al.[42], while the error remains below 6 %.

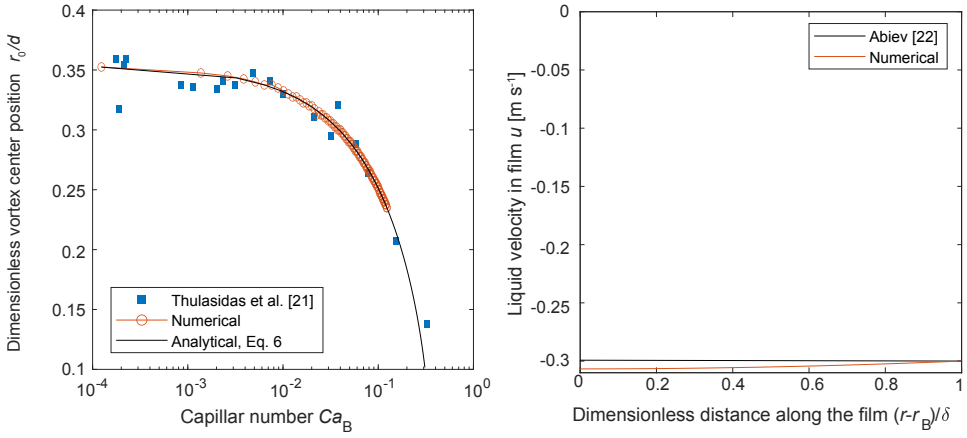

Figure 2.9: Vortex center position (r_0) as a function of the capillary number (left) and velocity profile in the film region (right).

2.E.2. MASS TRANSFER

The mass transfer coefficient over the entire bubble in the unit cell is compared to the results from Martïnez et al. [42]. The unit cell geometry is based on the reference case in their work, and the mesh is obtained with a fluidics controlled mesh in COMSOL. The results in terms of mesh, surface area and mass transfer coefficient are shown in Table 2.7. An error of less than 2 % is found in the calculation of the mass transfer coefficient. This deviation can be attributed to the difference in the mesh.

Table 2.7: Comparison mass transfer

	Martínez [[42]]	This work
Total mesh elements	77 318	52 724
Elements in liquid film	19	22
Surface are (Unit cell)	$7.50 \cdot 10^{-5}$ [m^2]	$7.50 \cdot 10^{-5}$ [m^2]
$k_L a$ (Unit cell)	0.080 [m^3_L/m$^3_{UC}$/s]	0.081 [m^3_L/m$^3_{UC}$/s]

2.E.3. BUFFER REACTION

The homogeneous carbon equilibrium reaction occurs in the liquid electrolyte as soon as carbon dioxide is introduced into the solution. With increasing, production of hydroxide ions from the electrochemical reaction CO_2 starts reacting in a buffer reaction. The following steps commonly describe the buffer reactions

$$CO_2 + OH^- \underset{-\,k_{1r}}{\overset{+\,k_{1f}}{\rightleftharpoons}} HCO_3^- \tag{2.22}$$

$$HCO_3^- + OH^- \underset{-\,k_{2r}}{\overset{+\,k_{2f}}{\rightleftharpoons}} CO_3^{2-} \tag{2.23}$$

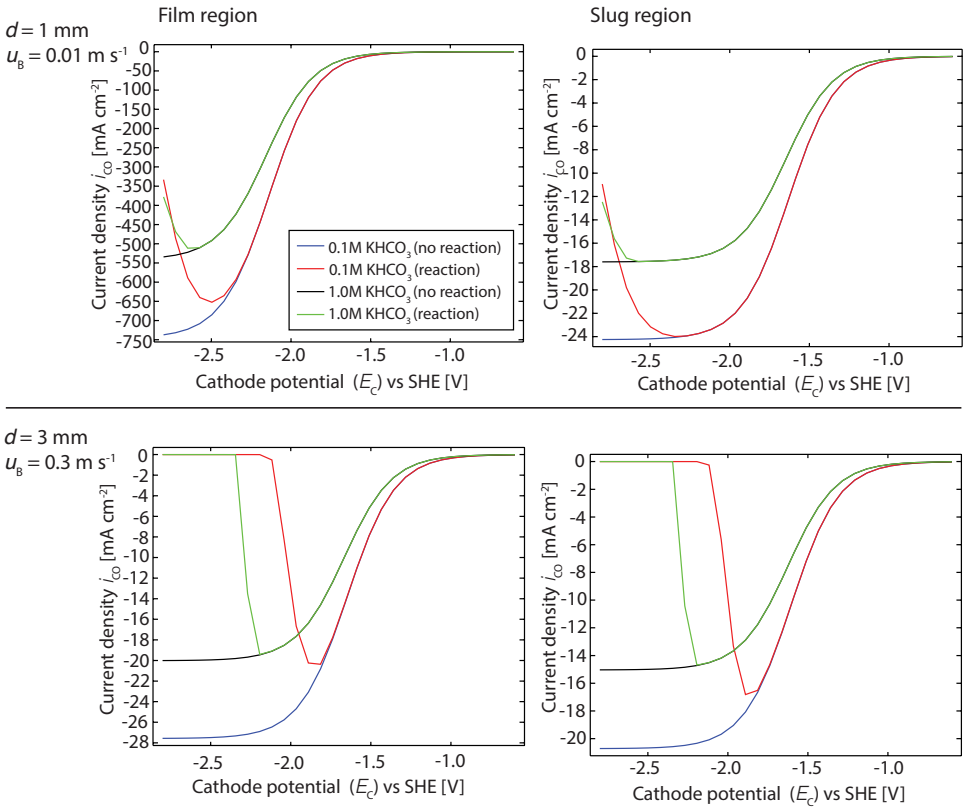

Figure 2.10: Current density over cathode potential from 1D diffusion reaction model with $\delta = \delta_F$.

The forward reaction rates are summarised in Table 2.3, while the backward reaction rates are corrected for the electrolyte salinity [56]. For H-cell and GDE reactors, the species balance is solved in addition to the homogeneous reaction as a source term, while migration is neglected [31, 66–68]. In this work, the transfer of hydroxide ions across the membrane, including migration, is not explicitly modelled to reduce computational costs. Further, as the homogeneous reactions lead to a stiff non-linear system of equations, the computational time and mesh requirements increase drastically. Therefore, the unit cell's geometry is simplified according to the analytical model; the film and slug region are viewed independent and the diffusion layer thickness is set to the film thickness ($\delta = \delta_F$). This leads to a 1D reaction-diffusion system with the saturation concentration and slug concentration as the boundary condition respectively for the two regions. In Figure 2.10 the current density for different electrolyte compositions and cases is displayed. No reaction, in this case, refers to the assumption that the flux of hydroxide ions across the membrane is equal to the production rate at the electrode leading to a current independent pH near the catalyst. Reaction refers to the other extreme case assuming no flux of hydroxide ions across the walls. It becomes evident that for low cathode potentials, the effect of the buffer reaction can be neglected, while for

higher potentials, the buffer reaction leads to a decrease in current density. The onset of this effect depends on the concentration of the electrolyte. As the 1 M $KHCO_3$ electrolyte shows a more significant buffer capacity and the depletion of CO_2 in the homogeneous reaction starts setting in at higher potentials and values close to the theoretical limiting current density, we choose in this work an electrolyte of 1 M $KHCO_3$ and work under the assumption that flux across the membrane equals the production rate. Therefore, the homogeneous buffer reaction is not modelled explicitly, and the potential window is chosen between -0.6 to -2.6 V vs SHE.

2.F. MESH FEATURES AND NUMERICAL SOLVER

A user-controlled mesh with unstructured quadrilateral elements is built, and a boundary layer with controlled element size and growth rate is introduced at the bubble's interface and wall. All meshes guarantee a minimum of 5 elements in the film region for all film thicknesses [69]. The mesh is then optimised to capture all relevant parameter combinations, hydrodynamics and species transport. The different meshes studied are summarised in Table 2.8. Note that the mesh parameters depend on the bubble velocity u_B and channel diameter d. For this study, the lower and upper limits of velocities and diameter are chosen for the mesh study. Relative tolerances of $1 \cdot 10^{-3}$ and $5 \cdot 10^{-4}$ are set for achieving convergence for the velocity profile and species transport, respectively. For hydrodynamics, the velocity profiles inside liquid slugs are observed. In the vortex centre, zero velocity is expected; therefore, the change in velocity at the vortex centre is taken as a point of comparison for the accuracy of the mesh, as shown in Figure 2.12. For the species transport, the local current density at the cathode over the unit cell and the concentration profile of CO_2 in the liquid slug is observed (Figure 2.12). Based on this, Mesh D is chosen for all simulations in this work. The mesh is shown in Figure 2.11.

Note: All simulations for the mesh independence study are performed on a computer with an Intel Core i5-4690 processor, 3.5GHz processor speed, and 24GB RAM. All other simulations are carried out on a cluster with a varying allocation of nodes.

Table 2.8: Mesh details for mesh independence study.

	Total elements	Biggest element (µm)	Smallest element (µm)	Elements in film	Computational effort (seconds)	u(r_0) cm s^{-1}	$i_{Lim,CO}$ mA cm^{-2}
Case A							
(1)	17 291	24 788	3 615	11	23	0.24	28.75
(2)	59 516	25 255	382	11	43	$3.28 \cdot 10^{-3}$	217.26
Case B							
(1)	60 123	10 210	2 869	11	78	0.19	24.13
(2)	121 839	15 923	182	11	79	$2.99 \cdot 10^{-3}$	217.42
Case C							
(1)	69 315	10 210	2 869	19	96	0.19	21.75
(2)	161 335	15 923	142	19	103	$2.99 \cdot 10^{-3}$	217.42
Case D							
(1)	**73 911**	**10 210**	**2 869**	**24**	**119**	**0.19**	**19.04**
(2)	**181 083**	**15 923**	**96**	**24**	**117**	$\mathbf{2.99 \cdot 10^{-3}}$	**217.40**
Case E							
(1)	258 876	5 105	1 094	30	2 238	0.19	17.6
(2)	566 412	8 158	53	30	2 522	$2.18 \cdot 10^{-3}$	217.60
Case F							
(1)	277 260	5 105	1 090	38	2 376	0.18	18.30
(2)	645 342	7 962	63	38	3 465	$2.19 \cdot 10^{-3}$	217.61

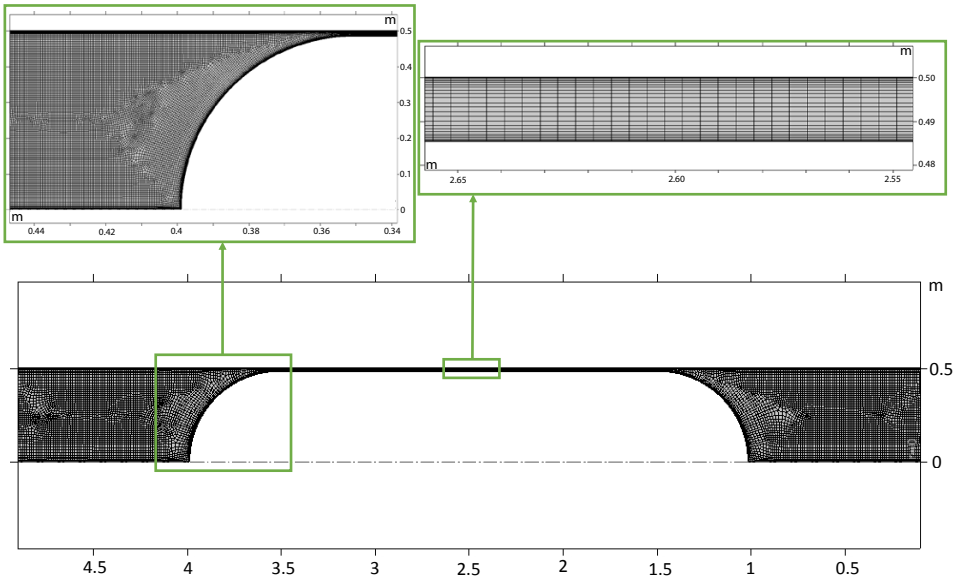

Figure 2.11: Mesh of the liquid domain in the unit cell with zoomed-in regions on bubble cap and film.

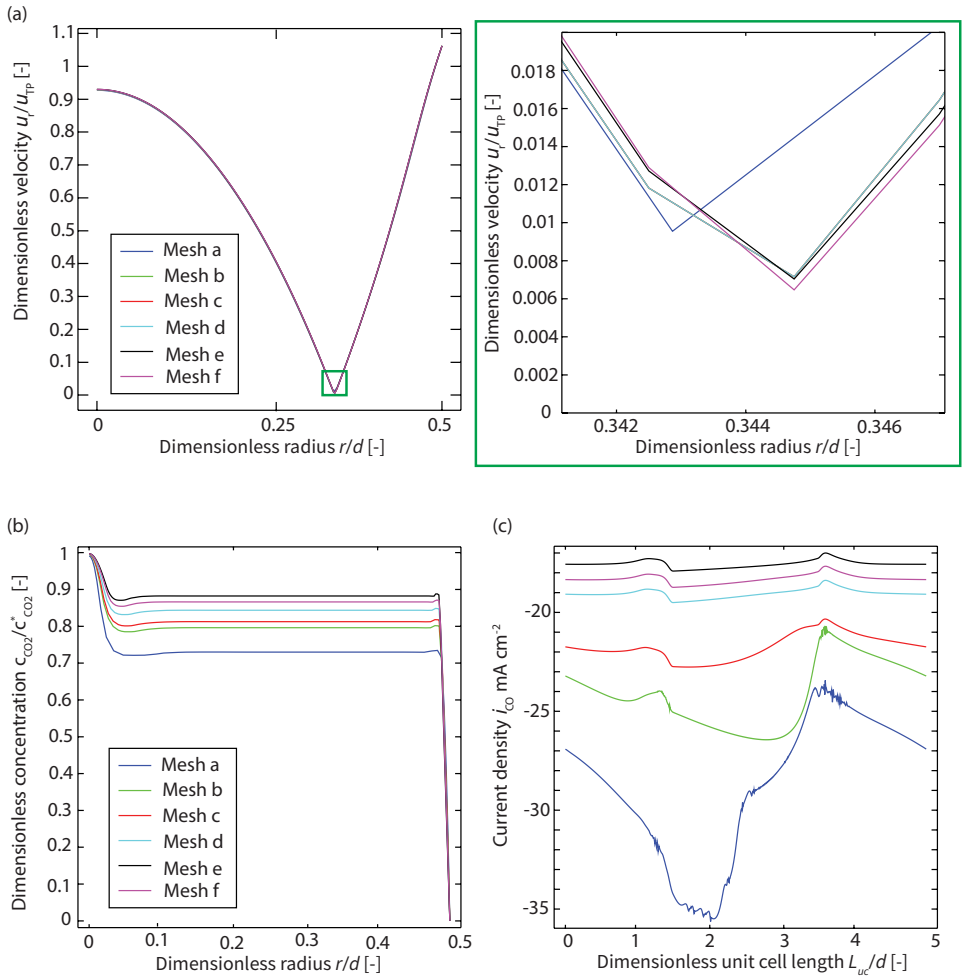

Figure 2.12: Velocity profile in the liquid slug for different meshes with a zoomed-in view of the vortex centre for a capillary with d = 3 mm and a bubble velocity of 0.3 m s^{-1} (a). CO_2 concentration profile (b) and local current density (c) for different meshes for a capillary with d = 3 mm and a bubble velocity of 0.3 m s^{-1}.

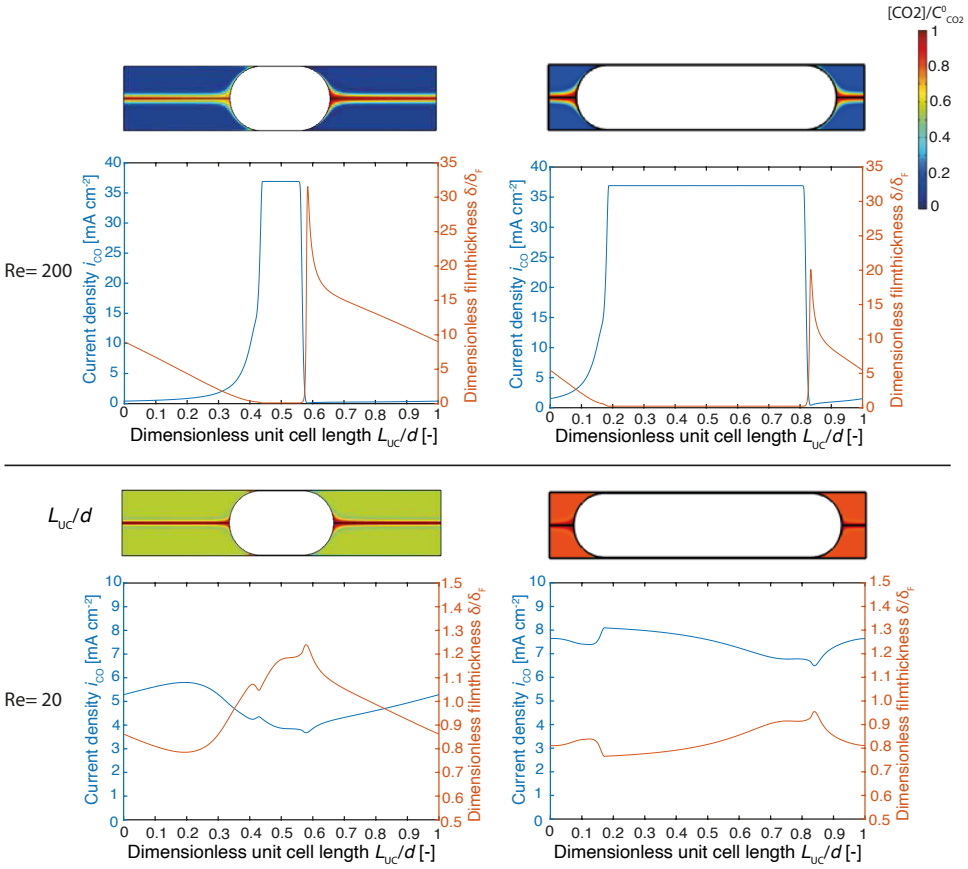

Figure 2.13: Dimensionless concentration of CO_2 for different void fractions and Reynolds-numbers with the limiting current density over the unit cell length and the dimensionless diffusion layer thickness.

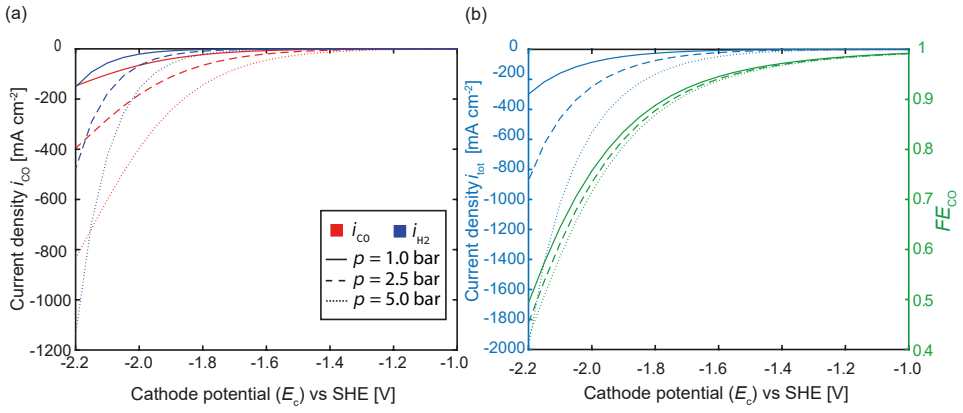

Figure 2.14: The influence of pressure on the partial current densities (a), and the sum of the partial current density and Faradaic efficiency (b). Pressure 1 bar solid line, 2.5 bar dashed and 5 bar doted lines.

REFERENCES

[1] I. Bagemihl, C. Bhatraju, J. R. van Ommen, and V. van Steijn, *Electrochemical reduction of CO_2 in tubular flow cells under gas–liquid Taylor flow,* ACS Sustainable Chemistry & Engineering **10**, 12580 (2022).

[2] G. A. Olah, A. Goeppert, and G. K. S. Prakash, *Chemical recycling of carbon dioxide to methanol and dimethyl ether: From greenhouse gas to renewable, environmentally carbon neutral fuels and synthetic hydrocarbons,* The Journal of Organic Chemistry **74**, 487 (2009).

[3] M. Gattrell, N. Gupta, and A. Co, *Electrochemical reduction of CO_2 to hydrocarbons to store renewable electrical energy and upgrade biogas,* Energy Conversion and Management **48**, 1255 (2007).

[4] W. A. Smith, T. Burdyny, D. A. Vermaas, and H. Geerlings, *Pathways to industrial-scale fuel out of thin air from CO_2 electrolysis,* Joule **3**, 1822 (2019).

[5] E. V. Kondratenko, G. Mul, J. Baltrusaitis, G. O. Larrazábal, and J. Pérez-Ramírez, *Status and perspectives of CO_2 conversion into fuels and chemicals by catalytic, photocatalytic and electrocatalytic processes,* Energy and Environmental Science **6**, 3112 (2013).

[6] M. G. Kibria, J. P. Edwards, C. M. Gabardo, C.-T. Dinh, A. Seifitokaldani, D. Sinton, and E. H. Sargent, *Electrochemical CO_2 reduction into chemical feedstocks: From mechanistic electrocatalysis models to system design,* Advanced Materials **31**, 1807166 (2019).

[7] T. Burdyny and W. A. Smith, *CO_2 reduction on gas-diffusion electrodes and why catalytic performance must be assessed at commercially-relevant conditions,* Energy and Environmental Science **12**, 1442 (2019).

[8] D. M. Weekes, D. A. Salvatore, A. Reyes, A. Huang, and C. P. Berlinguette, *Electrolytic CO_2 reduction in a flow cell,* Accounts of Chemical Research **51**, 910 (2018).

[9] C.-T. Dinh, T. Burdyny, M. G. Kibria, A. Seifitokaldani, C. M. Gabardo, F. P. G. de Arquer, A. Kiani, J. P. Edwards, P. D. Luna, O. S. Bushuyev, C. Zou, R. Quintero-Bermudez, Y. Pang, D. Sinton, and E. H. Sargent, *CO_2 electroreduction to ethylene via hydroxide-mediated copper catalysis at an abrupt interface,* Science **360**, 783 (2018).

[10] J.-B. Vennekoetter, R. Sengpiel, and M. Wessling, *Beyond the catalyst: How electrode and reactor design determine the product spectrum during electrochemical CO_2 reduction,* Chemical Engineering Journal **364**, 89 (2019).

[11] R. Kas, A. G. Star, K. Yang, T. Van Cleve, K. C. Neyerlin, and W. A. Smith, *Along the channel gradients impact on the spatioactivity of gas diffusion electrodes at high conversions during CO_2 electroreduction,* ACS Sustainable Chemistry & Engineering **9**, 1286 (2021).

[12] Z. Yang, D. Li, L. Xing, H. Xiang, J. Xuan, S. Cheng, E. H. Yu, and A. Yang, *Modeling and upscaling analysis of gas diffusion electrode-based electrochemical carbon dioxide reduction systems,* ACS Sustainable Chemistry & Engineering **9**, 351 (2021).

[13] P. Jeanty, C. Scherer, E. Magori, K. Wiesner-Fleischer, O. Hinrichsen, and M. Fleischer, *Upscaling and continuous operation of electrochemical CO_2 to CO conversion in aqueous solutions on silver gas diffusion electrodes,* Journal of CO_2 Utilization **24**, 454 (2018).

[14] S. Garg, M. Li, A. Z. Weber, L. Ge, L. Li, V. Rudolph, G. Wang, and T. E. Rufford, *Advances and challenges in electrochemical CO_2 reduction processes: An engineering and design perspective looking beyond new catalyst materials,* Journal of Materials Chemistry A **8**, 1511 (2020).

[15] K. Yang, R. Kas, W. A. Smith, and T. Burdyny, *Role of the carbon-based gas diffusion layer on flooding in a gas diffusion electrode cell for electrochemical CO_2 reduction,* ACS Energy Letters **6**, 33 (2021).

[16] L. M. Baumgartner, C. I. Koopman, A. Forner-Cuenca, and D. A. Vermaas, *Narrow pressure stability window of gas diffusion electrodes limits the scale-up of CO_2 electrolyzers,* ACS Sustainable Chemistry & Engineering **10**, 4683 (2022).

[17] M. T. Kreutzer, F. Kapteijn, J. A. Moulijn, and J. J. Heiszwolf, *Multiphase monolith reactors: Chemical reaction engineering of segmented flow in microchannels,* Chemical Engineering Science **60**, 5895 (2005).

[18] S. Haase, D. Y. Murzin, and T. Salmi, *Review on hydrodynamics and mass transfer in minichannel wall reactors with gas–liquid Taylor flow,* Chemical Engineering Research and Design **113**, 304 (2016).

[19] R. Gupta, D. Fletcher, and B. Haynes, *Taylor flow in microchannels: A review of experimental and computational work,* The Journal of Computational Multiphase Flows **2**, 1 (2010).

[20] F. Zhang, C. Chen, Y. Tang, and Z. Cheng, *CO_2 reduction in a microchannel electrochemical reactor with gas-liquid segmented flow,* Chemical Engineering Journal **392**, 124798 (2020).

[21] F. Zhang, Z. Jin, C. Chen, Y. Tang, S. A. Mahyoub, S. Yan, and Z. Cheng, *Electrochemical conversion of CO_2 to CO into a microchannel reactor system in the case of aqueous electrolyte,* Industrial and Engineering Chemistry Research **59**, 5664 (2020).

[22] V. Lawlor, S. Griesser, G. Buchinger, A. Olabi, S. Cordiner, and D. Meissner, *Review of the micro-tubular solid oxide fuel cell: Part I. stack design issues and research activities,* Journal of Power Sources **193**, 387 (2009).

[23] Z.-G. Shao, W.-F. Lin, F. Zhu, P. A. Christensen, H. Zhang, and B. Yi, *A tubular direct methanol fuel cell with ti mesh anode,* Journal of Power Sources **160**, 1003 (2006).

[24] T. Hatsukade, K. P. Kuhl, E. R. Cave, D. N. Abram, and T. F. Jaramillo, *Insights into the electrocatalytic reduction of CO_2 on metallic silver surfaces,* Physical Chemistry Chemical Physics **16**, 13814 (2014).

[25] S. Verma, X. Lu, S. Ma, R. I. Masel, and P. J. A. Kenis, *The effect of electrolyte composition on the electroreduction of CO_2 to CO on Ag based gas diffusion electrodes,* Physical Chemistry Chemical Physics **18**, 7075 (2016).

[26] K. Wu, E. Birgersson, B. Kim, P. J. A. Kenis, and I. A. Karimi, *Modeling and experimental validation of electrochemical reduction of CO_2 to CO in a microfluidic cell,* Journal of The Electrochemical Society **162**, F23 (2014).

[27] J. A. Bard, G. Inzelt, and F. Scholz, *Electrochemical dictionary* (Springer-Verlag, Berlin Heidelberg, 2012) p. 182.

[28] J. C. Bui, E. W. Lees, L. M. Pant, I. V. Zenyuk, A. T. Bell, and A. Z. Weber, *Continuum modeling of porous electrodes for electrochemical synthesis,* Chemical Reviews **122**, 11022 (2022).

[29] F. Goodridge and K. Scott, *Electrochemical process engineering: A guide to the design of electrolytic plant* (Plenum Press, New York, 1995) p. 158.

[30] P. Aussillous and D. Quéré, *Quick deposition of a fluid on the wall of a tube,* Physics of Fluids **12**, 2367 (2000).

[31] S. Nitopi, E. Bertheussen, S. B. Scott, X. Liu, A. K. Engstfeld, S. Horch, B. Seger, I. E. L. Stephens, K. Chan, C. Hahn, J. K. Nørskov, T. F. Jaramillo, and I. Chorkendorff, *Calculation for the cathode surface concentrations in the electrochemical reduction of CO_2 in $KHCO_3$ solutions,* Journal of Applied Electrochemistry **36**, 161 (2006).

[32] M. Ramdin, A. R. T. Morrison, M. de Groen, R. van Haperen, R. de Kler, L. J. P. van den Broeke, J. P. M. Trusler, W. de Jong, and T. J. H. Vlugt, *High pressure electrochemical reduction of CO_2 to formic acid/formate: A comparison between bipolar membranes and cation exchange membranes,* Industrial & Engineering Chemistry Research **58**, 1834 (2019).

[33] A. R. T. Morrison, V. van Beusekom, M. Ramdin, L. J. P. van den Broeke, T. J. H. Vlugt, and W. de Jong, *Modeling the electrochemical conversion of carbon dioxide to formic acid or formate at elevated pressures,* Journal of The Electrochemical Society **166**, E77 (2019).

[34] B. Endrődi, E. Kecsenovity, A. Samu, F. Darvas, R. V. Jones, V. Török, A. Danyi, and C. Janáky, *Multilayer electrolyzer stack converts carbon dioxide to gas products at high pressure with high efficiency,* ACS Energy Letters **4**, 1770 (2019).

[35] G. Berčič and A. Pintar, *The role of gas bubbles and liquid slug lengths on mass transport in the Taylor flow through capillaries,* Chemical Engineering Science **52**, 3709 (1997).

[36] R. K. Edvinsson and S. Irandoust, *Finite-element analysis of Taylor flow,* AIChE Journal **42**, 1815 (1996).

[37] J. van Baten and R. Krishna, *CFD simulations of wall mass transfer for Taylor flow in circular capillaries,* Chemical Engineering Science **60**, 1117 (2005).

[38] N. Shao, A. Gavriilidis, and P. Angeli, *Mass transfer during Taylor flow in microchannels with and without chemical reaction,* Chemical Engineering Journal **160**, 873 (2010).

[39] C. Butler, E. Cid, A.-M. Billet, and B. Lalanne, *Numerical simulation of mass transfer dynamics in Taylor flows,* International Journal of Heat and Mass Transfer **179**, 121670 (2021).

[40] M. Woo, S. Tischer, O. Deutschmann, and M. Wörner, *A step toward the numerical simulation of catalytic hydrogenation of nitrobenzene in Taylor flow at practical conditions,* Chemical Engineering Science **230**, 116132 (2021).

[41] J. van Baten and R. Krishna, *CFD simulations of mass transfer from Taylor bubbles rising in circular capillaries,* Chemical Engineering Science **59**, 2535 (2004).

[42] F. L. D. Martínez, C. Julcour, A.-M. Billet, and F. Larachi, *Modelling and simulations of a monolith reactor for three-phase hydrogenation reactions — Rules and recommendations for mass transfer analysis,* Catalysis Today **273**, 121 (2016).

[43] R. S. Abiev, *Gas-liquid and gas-liquid-solid mass transfer model for Taylor flow in micro (milli) channels: A theoretical approach and experimental proof,* Chemical Engineering Journal Advances **4**, 100065 (2020).

[44] Y. Cao, C. Soares, N. Padoin, and T. Noël, *Gas bubbles have controversial effects on Taylor flow electrochemistry,* Chemical Engineering Journal **406**, 126811 (2021).

[45] T. Nijhuis, M. Kreutzer, A. Romijn, F. Kapteijn, and J. Moulijn, *Monolithic catalysts as efficient three-phase reactors,* Chemical Engineering Science **56**, 823 (2001).

[46] L. Zhou, M. Cheng, B. Yi, Y. Dong, Y. Cong, and W. Yang, *Performance of an anode-supported tubular solid oxide fuel cell (SOFC) under pressurized conditions,* Electrochimica Acta **53**, 5195 (2008).

[47] A. Laube, A. Hofer, B. Sánchez Batalla, S. Ressel, A. Chica, S. Fischer, C. Weidlich, J. Bachmann, and T. Struckmann, *Tubular membrane electrode assembly for PEM electrolysis,* International Journal of Hydrogen Energy **47**, 15943 (2022).

[48] W. Jud, C. O. Kappe, and D. Cantillo, *A continuous flow cell for high-temperature/high-pressure electroorganic synthesis,* ChemElectroChem **7**, 2777 (2020).

[49] P. Lobaccaro, M. R. Singh, E. L. Clark, Y. Kwon, A. T. Bell, and J. W. Ager, *Effects of temperature and gas–liquid mass transfer on the operation of small electrochemical cells for the quantitative evaluation of CO_2 reduction electrocatalysts,* Physical Chemistry Chemical Physics **18**, 26777 (2016).

[50] S. Ressel, A. Laube, S. Fischer, A. Chica, T. Flower, and T. Struckmann, *Performance of a vanadium redox flow battery with tubular cell design,* Journal of Power Sources **355**, 199 (2017).

[51] W. Wagner, *VDI-Wärmeatlas,* (Springer Berlin Heidelberg, Berlin, Heidelberg, 2006) Chap. Stoffwerte von Wasser, pp. 133–147.

[52] M. J. W. Frank, J. A. M. Kuipers, and W. P. M. van Swaaij, *Diffusion coefficients and viscosities of CO_2 + H_2O, CO_2 + CH_3OH, NH_3 + H_2O, and NH_3 + CH_3OH liquid mixtures,* Journal of Chemical & Engineering Data **41**, 297 (1996).

[53] J. S. Newmann and K. E. Thomas-Alyea, *Electrochemical Systems,* 3rd ed. (Hoboken, N.J. : J. Wiley, 2012).

[54] R. Sander, *Compilation of Henry's law constants (version 4.0) for water as solvent,* Atmospheric Chemistry and Physics **15**, 4399 (2015).

[55] K. Schulz, U. Riebesell, B. Rost, S. Thoms, and R. Zeebe, *Determination of the rate constants for the carbon dioxide to bicarbonate inter-conversion in pH-buffered seawater systems,* Marine Chemistry **100**, 53 (2006).

[56] F. J. Millero, T. B. Graham, F. Huang, H. Bustos-Serrano, and D. Pierrot, *Dissociation constants of carbonic acid in seawater as a function of salinity and temperature,* Marine Chemistry **100**, 80 (2006).

[57] A. C. Olesen, S. H. Frensch, and S. K. Kær, *Towards uniformly distributed heat, mass and charge: A flow field design study for high pressure and high current density operation of PEM electrolysis cells,* Electrochimica Acta **293**, 476 (2019).

[58] R. K. Edvinsson and S. Irandoust, *Finite-element analysis of Taylor flow,* AIChE Journal **42**, 1815 (1996).

[59] N. Shao, W. Salman, A. Gavriilidis, and P. Angeli, *CFD simulations of the effect of inlet conditions on Taylor flow formation,* International Journal of Heat and Fluid Flow **29**, 1603 (2008).

[60] V. van Steijn, C. R. Kleijn, and M. T. Kreutzer, *Predictive model for the size of bubbles and droplets created in microfluidic T-junctions,* Lab on a Chip **10**, 2513 (2010).

[61] M. T. Kreutzer, F. Kapteijn, J. A. Moulijn, C. R. Kleijn, and J. J. Heiszwolf, *Inertial and interfacial effects on pressure drop of Taylor flow in capillaries,* AIChE Journal **51**, 2428 (2005).

[62] S. Weisenberger and A. Schumpe, *Estimation of gas solubilities in salt solutions at temperatures from 273 K to 363 K,* AIChE Journal **42**, 298 (1996).

[63] G. I. Taylor, *Deposition of a viscous fluid on a plane surface,* Journal of Fluid Mechanics **9**, 218 (1960).

[64] T. Thulasidas, M. Abraham, and R. Cerro, *Bubble-train flow in capillaries of circular and square cross section,* Chemical Engineering Science **50**, 183 (1995).

[65] R. S. Abiev, *Bubbles velocity, Taylor circulation rate and mass transfer model for slug flow in milli- and microchannels,* Chemical Engineering Journal **227**, 66 (2013).

[66] L.-C. Weng, A. T. Bell, and A. Z. Weber, *Modeling gas-diffusion electrodes for CO_2 reduction,* Physical Chemistry Chemical Physics **20**, 16973 (2018).

[67] T. Burdyny and W. A. Smith, *CO_2 reduction on gas-diffusion electrodes and why catalytic performance must be assessed at commercially-relevant conditions,* Energy & Environmental Science **12**, 1442 (2019).

[68] R. Kas, A. G. Star, K. Yang, T. Van Cleve, K. C. Neyerlin, and W. A. Smith, *Along the channel gradients impact on the apatioactivity of gas diffusion electrodes at high conversions during CO_2 electroreduction,* ACS Sustainable Chemistry & Engineering **9**, 1286 (2021).

[69] R. Gupta, D. F. Fletcher, and B. S. Haynes, *On the CFD modelling of Taylor flow in microchannels,* Chemical Engineering Science **64**, 2941 (2009).

3

EXPLORING THE VIABILITY OF A TAYLOR FLOW ELECTROLYSER FOR ENHANCED CO_2 ELECTROLYSIS.

This chapter is in preparation for submission to *Chemical Engineering Journal*.

Electrochemical processes are an important part of the energy transition. A reactor concept that is already available at industrial scale is the zero-gap membrane electrolyser for electrolysis of water. Attempts to adapt this concept for the electrochemical reduction of CO_2 have shown success in alleviating mass transfer limitations, thereby theoretically rendering the process industrially feasible, however challenges persist regarding operational stability. Recent studies suggest a change of flow pattern from single-phase flow to gas-liquid Taylor flow as a potential solution to overcome mass transfer limitations without compromising operational stability. However, operation under Taylor flow has only been studied in tubular reactors that are difficult to scale up to industrially relevant scales. Therefore, in this work, we introduce an experimental setup designed to examine the impact of gas-liquid Taylor flow on the Faradaic efficiency for a range of current densities in a scalable zero-gap membrane electrolyser configuration for CO_2 electrolysis to CO. Our transparent reactor design, featuring an inlet junction that allows the generation of stable Taylor flow over a range of flow velocities and gas-to-liquid ratios, facilitates the investigation of hydrodynamics alongside reactor performance. We demonstrate that, at a constant current density, utilising Taylor flow doubles the Faradaic efficiency towards CO compared to utilising single-phase flow. Additionally, our findings indicate that, within the two-phase velocity range studied ($0.9 - 4.5\,\mathrm{cm\,s^{-1}}$), the Faradaic efficiency towards CO is minimally influenced by the gas-to-liquid ratio, while it increases with flow velocity. Our results further suggest that changes in the pre-treatment and design of the electrode are needed to reach compatible current densities and Faradaic efficiencies for industrial application.

3.1. INTRODUCTION

The energy transition demands an increased use of renewable electricity in the process industry. This includes the (temporary) storage of energy in chemical bonds [1–4], for example in H_2 through electrolysis of H_2O, and the production of base chemicals or its precursors (syngas) through electrolysis [5–7]. Electrolysers at industrial scale, such as polymer electrolyte membrane (PEM) water electrolysers, are designed with a sandwich structure, where the electrodes and membrane are pressed together in a membrane electrode assembly (MEA), and the liquid electrolyte passes by at the anode and cathode side in a rectangular flow channel [8–11]. A similar design has been adapted for the electrochemical reduction of CO_2 [12–15]. Due to the low solubility of CO_2 in the liquid electrolyte, the achievable current densities in liquid-based electrolysers remain low [6, 16, 17]. Naturally, different studies have focused on increasing the solubility of CO_2 in the liquid electrolyte by, for example, increasing the pressure [18–21] or using non-aqueous electrolytes [22–25]. In parallel, possibilities to enhance the mass transfer rate by means of reactor design have been explored, leading to the widely adapted design of MEA electrolysers. These electrolysers are operated either with a humidified or dry gas stream of CO_2, therefore reducing the liquid diffusion pathway of CO_2 to the catalyst [6, 15, 26, 27]. While these electrolysers reach high Faradaic efficiencies (selectivities) at industrially desired current densities (reaction rates), they suffer from operational stability, as the absence of a liquid electrolyte leads to salt precipitation [28–32].

One promising reactor design that increases mass transfer without the challenge of salt precipitation is a microreactor operated under gas-liquid Taylor flow [33, 34]. Microreactors are known to enhance mass transfer in thermo-catalytic and photoelectric

systems due to the high surface-to-volume ratio and short diffusion distances [35–38]. In the field of CO_2 electrolysis, microreactors have been explored as tubular flow cells operated under gas-liquid Taylor flow. In this reactor design, the gaseous CO_2 is pushed through the narrow flow channels in the form of elongated gas bubbles that are separated from the walls by a thin lubrication layer of liquid electrolyte and from each other by liquid slugs [33]. Zhang *et al.* [34] have shown that Taylor flow in annular flow channels generally increases the Faradaic efficiency towards CO_2 reduction products at fixed current densities compared to H-cell experiments. However, the reported Faradaic efficiencies are significantly lower than those achieved in MEA electrolysers. Further, the design and scale-up of tubular electrolysers is not straightforward [39], while successful scale-up of sandwich-structured MEA electrolysers with their rectangular flow channels has already been achieved for water electrolysers [40–42]. It is therefore of interest to understand to what extent gas-liquid Taylor flow can enhance mass transfer in an established reactor design. While there are various studies on the effect of Taylor flow in reactive, rectangular, single-channel microreactors for thermo-catalytic reactions [43–51], there are limited studies on the effect of Taylor flow in rectangular, single-channel microreactors for electrochemical reactions [38, 52, 53]. The available studies vary in reactor design with Taylor flow travelling through the inter-electrode gap instead of passing by the MEA, leading to very specific trade-offs [38], or focus on Taylor flow evolving as a result of gas evolution in water electrolysis [52, 53]. Therefore, there is a lack of knowledge on how Taylor flow influences the Faradaic efficiency for a given current density in mass transfer-limited electrolytic reactions such as the reduction of CO_2.

In this work, we close this gap by studying how gas-liquid Taylor flow affects the CO_2 reduction performance using a transparent, sandwich-structured, MEA electrolyser with a rectangular channel. As a model system, we chose the mass transfer-limited CO_2 reduction reaction to CO on a silver gauze. This choice is motivated by the stability of silver as a catalyst under various conditions with primarily gaseous reaction products (CO and H_2) [54, 55], allowing for easy product analysis during the reaction. Furthermore, due to its porous gauze design, high conductivity, and hydrophilic nature, the silver gauze presents a ready-to-use electrode to achieve stable Taylor flow. We integrated an inlet configuration that allows forming the gaseous CO_2 bubbles directly in the flow channel and gives flexibility to manipulate the two-phase velocity and gas-to-liquid ratio, which are known to influence the mass transfer rate [56, 57]. We study the effect of these two flow features on the Faradaic efficiency (or selectivity) as the mass transfer-related reactor performance parameter for a range of given current densities. We show that for the chosen two-phase velocity range ($0.9 - 4.5\,\mathrm{cm\,s^{-1}}$), the Faradaic efficiency towards CO is minimally influenced by the gas-to-liquid ratio for a fixed current density, while it increases with the two-phase velocity, contrary to most literature. On the one hand, we demonstrate the potential and limitations of Taylor flow for mass transfer-limited electrochemical reactions and on the other hand present a valuable tool to study the mass transfer of Taylor flow in a reactive flow channel.

3.2. EXPERIMENTAL

We designed an electrolyser for the study of the effect of Taylor flow on the performance of the reactor. Such an electrolyser requires: I) the integration of a gas-liquid cross junction where the Taylor bubbles form, II) a flow channel design with corresponding material selection suitable to establish stable Taylor flow (e.g. no irregular bubble formation due to hysteretic effects at partially wetting walls and no bubble coalescence or breakup due to bubbles getting stuck on hydrophobic or rough materials), and III) the selection of a membrane electrode assembly with a good operational stability under the considered flow and reaction conditions. The experimental set-up further requires the continuous monitoring of the reactor performance without disturbing the flow. In the following section we discuss the choices made to meet all of the above requirements for the electrolyser design, followed by a description of the experimental set-up and the electrochemical experiments.

3.2.1. ELECTROLYSER DESIGN

The transparent electrolysis cell used for this study was designed and fabricated in-house and is shown schematically in Figure 3.1a). An anion exchange membrane (AEM) (SELEMION AMVN) is placed in the centre of the cell, sandwiched between the cathode and the anode, with two silicon gaskets for sealing. A silver gauze (Alfa Aesar, 99.9%, 80 mesh woven from 0.115 mm diameter wire) acts as the cathode and a nickel foam (MTI Corporation, EQ-benf-03) as the anode. Straight channels for the electrolytes at the anode and the cathode side are water cut into 2 mm thick titanium plates. The channels are $W = 2$ mm wide, $H = 2$ mm deep, and $L = 85$ mm long. The geometrical area of the electrodes is $A = W \times L = 170\,\text{mm}^2$. The design of the titanium plates provides external electrical contact to control the potential difference between anode and cathode. The

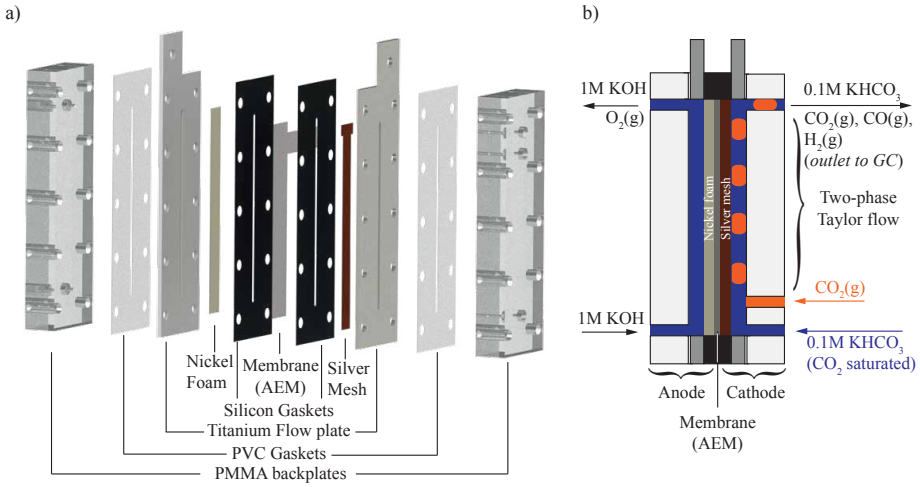

Figure 3.1: Electrolyser design. a) Exploded assembly drawing of the alkaline electrochemical reactor for the reduction of CO_2 to CO on a silver cathode. b) Side view of the reactor operated under gas-liquid Taylor flow forming at a T-junction.

entire assembly is clamped between two 20 mm thick transparent polymethyl methacrylate (PMMA) end-plates using ten M4 screw joints, each tightened to a torque of 1 N m. The screws are electrically isolated from the titanium plates by a layer of Kapton tape. Transparent polyvinylchlorid (PVC) gaskets are placed between the titanium flow plates and the transparent end-plates to prevent leakages. The liquid electrolyte solutions (1M KOH on the anode side and 0.1M $KHCO_3$ on the cathode side) are fed from the bottom of the cell via 1.5 mm wide openings at the end-plate, see Figure 3.1b). On the cathode side, a second inlet with the same dimensions is placed 5 mm away from the liquid electrolyte inlet. This inlet is used to introduce a pure gaseous CO_2 stream. At the T-junction, where the gaseous CO_2 and liquid electrolyte meet, bubbles are formed which travel as gas-liquid Taylor flow through the straight channel at the cathode side.

3.2.2. EXPERIMENTAL SET-UP AND ELECTROCHEMICAL EXPERIMENTS

The transparent electrolytic cell is integrated into the experimental set-up shown in Figure 3.2. This set-up allows to continuously visualise the features of the gas-liquid Taylor flow and measure the reactor performance parameters during the electrochemical reaction. We expect that the mass transfer and hence the reactor performance depends on the three following flow features of the Taylor flow: I) two-phase velocity u_{TP}, II) gas-to-liquid ratio ϵ_g, and III) unit cell length L_{UC}. The two-phase velocity u_{TP} is defined as the sum of the superficial velocity of the gas u_g and liquid u_l phase, i.e.,

$$u_{TP} = u_g + u_l = \frac{\dot{Q}_g}{WH} + \frac{\dot{Q}_l}{WH}, \tag{3.1}$$

with $\dot{Q}_g$ and $\dot{Q}_l$ the volumetric flow rates of gas and liquid. The gas-to-liquid ratio ϵ_g, also known as dynamic gas holdup, is defined as the ratio of superficial gas to two-phase velocity [56, 57], i.e.,

$$\epsilon_g = \frac{u_g}{u_{TP}}. \tag{3.2}$$

The unit cell length L_{UC} is simply defined as the sum of the length of a gas bubble L_B and a liquid slug L_S, i.e.,

$$L_{UC} = L_B + L_S. \tag{3.3}$$

Unlike the length of the gas bubbles and the liquid slugs, and hence the length of the unit cell, which are measured quantities, the two-phase velocity and the gas-to-liquid ratio are input quantities that are directly controlled through the gas and liquid flow rate. The flow rate of the fresh, gaseous CO_2 stream is controlled via a mass flow controller (MFC), while the liquid electrolytes at both the anode and cathode side are recirculated from gas-liquid separators (liquid volume of 100 mL) via HPLC pumps (KNAUER Blue Shadow). The HPLC pumps allow minimising pressure fluctuations, which can affect the formation of the two-phase flow. To further reduce any influence of pressure fluctuations, a 4 cm PEEK tube with an inner diameter of 130 µm is placed at the liquid catholyte inlet, and a 8 cm long PEEK tube with an inner diameter of 25 µm is placed at the gaseous CO_2 inlet. The resulting unit cell length for a fixed two-phase velocity and gas-to-liquid ratio is measured from five different photos captured by the camera through the transparent end-plates of the electrolysis cell at the channel inlet, middle, and outlet.

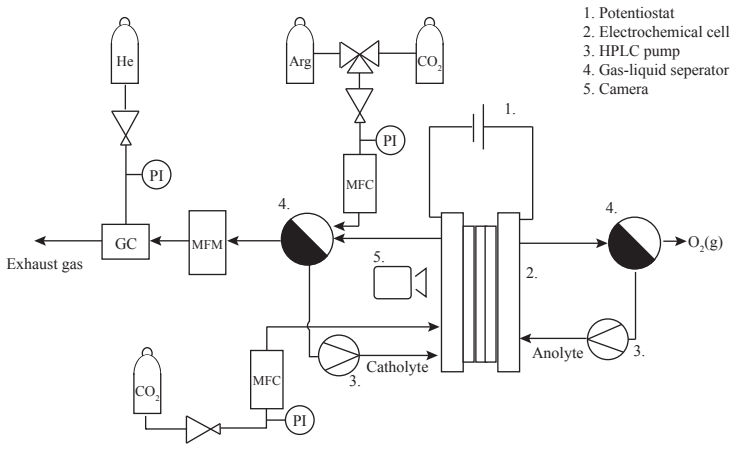

Figure 3.2: Schematic of the experimental set-up for the simultaneous visualisation of the gas-liquid Taylor flow and analysis of the electrochemical performance. The schematic shows all mass flow controllers (MFC) with the adjacent pressure indicators (PI) and mass flow meters (MFM) and gas-liquid separators to enable the recirculation of the liquid electrolytes.

The anode is fed with a 1M KOH electrolyte while the evolving gases are vented out to the atmosphere after leaving the electrolyser. The cathode is fed with a 0.1M $KHCO_3$ electrolyte which is constantly saturated with CO_2 by bubbling pure CO_2 at a flow rate of $8\,mL\,min^{-1}$ into the gas-liquid separator. The evolving gases from the cathode are pushed out of the reservoir (in this study by a constant Argon flow of $6\,mL\,min^{-1}$) to the gas chromatograph (Micro GC, Agilent) where the gas composition is continuously analysed. The mass flow rate, which is measured before the GC, is used to calculate the Faradaic efficiency as further detailed in Section 3.A (appendix). All experiments are carried out at a constant current I resulting in a constant current density $i_{tot} = I/A$ in a two-electrode configuration with a Biologic VMP-300 potentiostat. Prior to each experiment, both electrodes are cleaned ultrasonically in acetone, followed by ethanol and deionised water.

The range of velocities studied in this work is similar to the work by Haase *et al.* [51], i.e., $u_{TP} = 0.9 - 4.5\,cm\,s^{-1}$, allowing a direct comparison of the observed trends to observations for thermo-catalytic Taylor flow reactors. This velocity range results in a catholyte flow rate between $\dot{Q}_l = 0.55 - 10.80\,mL\,min^{-1}$, for a gas-to liquid ratio between 0 - 75 %. The anolyte flow rate is in all cases fixed to $10\,mL\,min^{-1}$ to allow for fast removal of the evolving oxygen bubbles. For reference, we performed measurements in an H-cell as detailed in Section 3.B (appendix).

3.3. RESULTS & DISCUSSION

We first discuss the flow features and stability of the Taylor flow in Section 3.3.1, followed by a discussion on the reactor performance in terms of Faradaic efficiency and current density in Sections 3.3.2-3.3.5. More specifically, first the electrochemical performance of the silver gauze is evaluated in terms of Faradaic efficiency for varying current densi-

ties in a known system (H-cell) and then in the above described flow cell under single-phase and Taylor flow for a single set of flow rates as described in Section 3.3.2. Afterwards, the dependence of the Faradaic efficiency on the Taylor flow features in terms of the gas-to-liquid ratio and two-phase velocity is reported for a range of fixed current densities in Section 3.3.3 and 3.3.4, respectively. Lastly, the influence of electrode design is discussed in Section 3.3.5 from a theoretical point of view, pinpointing avenues towards design optimisation.

3.3.1. ANALYSIS OF THE TAYLOR FLOW FEATURES

We first study how the length of the bubbles, slugs, and unit cell depends on the directly controlled gas-to-liquid ratio and two-phase velocity. In a first set of experiments, we vary the gas-to-liquid ratio by varying the ratio between the gaseous and liquid inlet flow rates, while keeping the sum of the inlet flow rates fixed such that the two-phase velocity is fixed as well. For an increasing gas-to-liquid ratio, we observe longer CO_2 gas bubbles separated by shorter electrolyte slugs for a fixed two-phase velocity of $u_{TP} = 4.5\,\mathrm{cm\,s^{-1}}$, see Figure 3.3a). In a second set, we vary the two-phase velocity, while fixing the gas-to-liquid ratio to $\epsilon_g = 0.75$. For an increased two-phase velocity, we observe Taylor bubbles with a similar length, see Figure 3.3b). The dependence of the unit cell length on the gas-to-liquid ratio and two-phase velocity is shown in Figure 3.3c), with the produced Taylor flow for all states in between detailed in Section 3.C (appendix). For a fixed two-phase velocity, we expect a fixed unit cell length, irrespective of the gas-to-liquid ratio, based on the simple argument that the flow rate of gas $\dot{Q}_g$ equals the volume of an individual bubble V_B multiplied by its generation frequency ν, i.e., $\dot{Q}_g = \nu V_B$. Similarly, $\dot{Q}_l = \nu V_L$, with

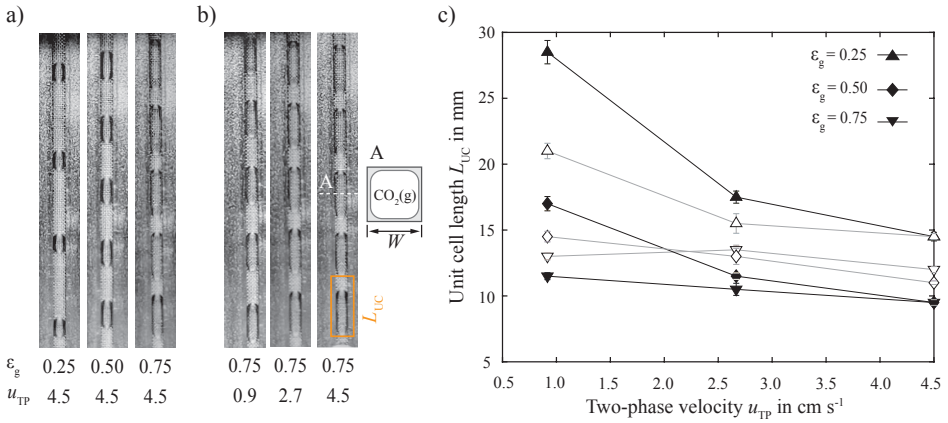

Figure 3.3: Taylor flow characterisation. a) Photographs of the observed Taylor flow for a fixed two-phase velocity u_{TP} in $\mathrm{cm\,s^{-1}}$ a) and a fixed gas-to-liquid ratio ϵ_g b) with the resulting unit cell length L_{UC} in mm c). The unit cell is taken as indicated by the orange box and the expected cross sectional view of the gaseous CO_2 bubble in the rectangular channel are shown in b). The Reynolds number and Capillary number follow as $\mathrm{Re} = \rho_l W u_{TP}/\mu_l = [20 - 100]$ and $\mathrm{Ca} = \mu_l u_{TP}/\gamma = [1.1 - 5.5] \times 10^{-4}$, with ρ_l and μ_l the density and viscosity of the liquid and γ the surface tension between the liquid and gas. All experiments are performed at $T = 293\,\mathrm{K}$ and $p = 0.1\,\mathrm{MPa}$ with the media: CO_2-electrolyte (0.1M $KHCO_3$). Repeats are shown as open symbols and grey lines; the error bars are the standard deviation within one experiment.

V_L the volume of an individual liquid slug. The sum of the flow rates hence is directly proportional to the volume of a unit cell, and hence to its length, such that $u_{TP} \propto L_{UC}$. A roughly constant unit cell length is indeed observed at the highest velocities. At lower velocities, this simple argument does not hold as seen from a strong dependence of the unit cell length on the gas-to-liquid ratio. This behaviour resonates with the findings of Haase *et al.* [51] and is characteristic for the formation of bubbles and slugs in rectangular microchannels at low velocities as explained in Korczyk *et al.* [58].

Over the entire range of two-phase velocities and gas-to-liquid ratios, we observe stable flow with no bubble coalescence/break-up or hysteretic or oscillatory behaviour during formation and flow through the channel, as clear from the well-defined length of the bubbles and slugs over time, evident from the error bars in Figure 3.3c).

3.3.2. ELECTROCHEMICAL PERFORMANCE

The state of the electrode and reactor design essentially determines the Faradaic efficiency and partial current density towards CO. Figure 3.4, therefore, shows the measured performance of the silver gauze in the established batch cell (H-cell (green line)) compared to the herein introduced flow cell. The flow cell is operated under two scenarios i) CO_2-saturated single-phase flow with a velocity of $4.5\,cm\,s^{-1}$ (red line) and ii) Taylor flow with a gas-to-liquid ratio of 0.5 and a two-phase velocity of $4.5\,cm\,s^{-1}$ (blue line). As expected, the Faradaic efficiency towards CO increases when increasing the applied current density (i_{tot}). After reaching a maximum further increasing the current density leads to a decrease in the observed Faradaic efficiency. The highest Faradaic efficiency and current density at which this maximum is reached varies per reactor type and flow condition, with the highest Faradaic efficiency towards CO reached in the H-cell and the lowest in the flow cell operated under CO_2-saturated single-phase flow. Comparing the partial current density towards CO in Figure 3.4b) shows that the partial current density is almost independent of the reactor type and flow conditions below an applied current density of $-9\,mA\,cm^{-2}$ (vertical grey line), indicating that the reaction is mainly controlled by kinetics (reaction rate limited). For higher applied currents, the partial current density for the flow cell operated under CO_2-saturated single-phase flow is approaching a fixed value, showing that mass transfer limits the reaction (mass transfer controlled). For the H-cell and the flow cell operated under gas-liquid Taylor flow a decrease in the slope can be observed for increased applied currents indicating that mass transfer limitations start to influence the electrochemical performance.

The Faradaic efficiency and partial current density for H_2 is highest in the flow cell operated under CO_2-saturated single-phase flow, see Figure 3.4c) and d), respectively. This is expected as CO_2 is not only consumed in the electrochemical reaction, but also in the homogeneous buffer reaction when the local pH increases. We expect that a boundary layer close to the electrode forms with a higher pH compared to the bulk electrolyte therefore decreasing the availability of CO_2 over the channel length. This leads to an increase in the hydrogen evolution reaction over the channel length, which increases with increasing the applied current [59, 60]. In the H-cell and the flow cell operated under gas-liquid Taylor flow, gaseous CO_2 is constantly supplied to the electrolyser. Therefore, a near constant boundary layer over the catalyst length is expected with a thickness of around 50 - 100 μm in the H-cell [61, 62]. Under gas-liquid Taylor flow mass transfer

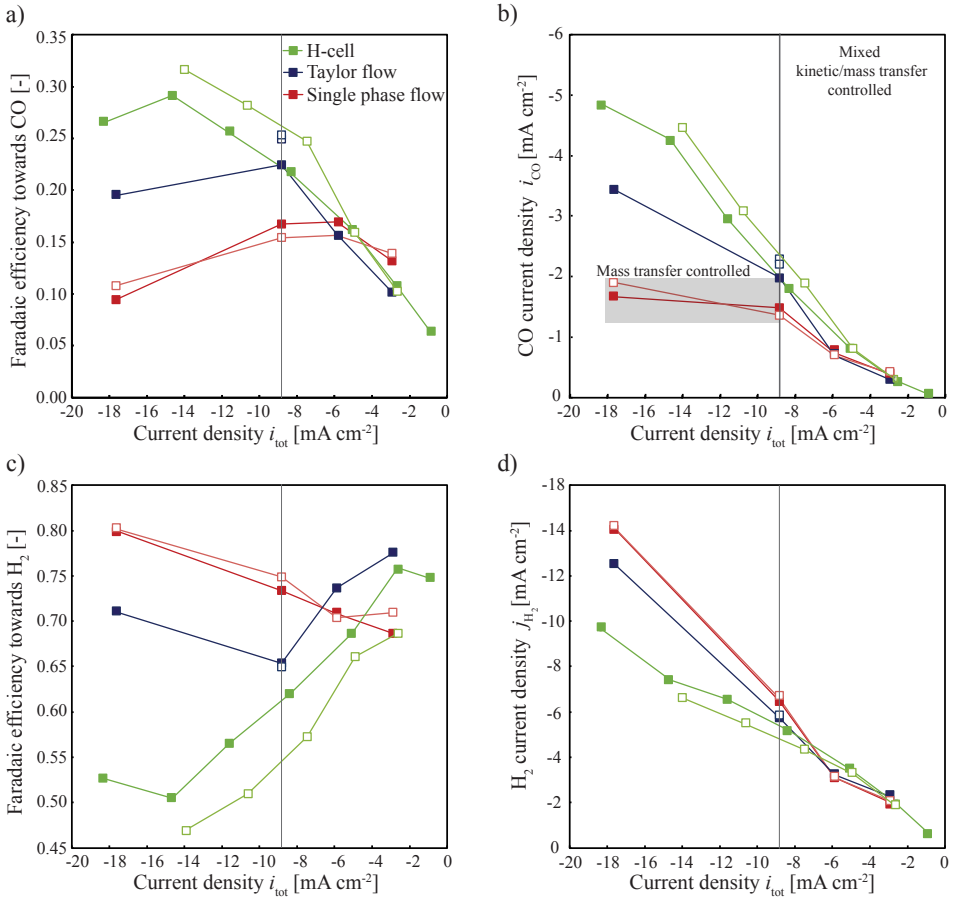

Figure 3.4: Electrochemical performance of CO_2 reduction in the electrochemical flow cell with rectangular millichannel under single-phase flow with $u_l = 4.50\,cm\,s^{-1}$ (red) and under gas-liquid Taylor flow with $u_l = 2.25\,cm\,s^{-1}$ and $u_g = 2.25\,cm\,s^{-1}$ ($u_{TP} = 4.5\,cm\,s^{-1}$ and $\epsilon_g = 0.5$) (blue), together with reference measurements in an H-cell (green). a), c): Faradaic efficiency of CO, H_2 vs. current density. b), d): Partial current densities of CO, H_2 vs. total current density. Repeats are shown as open symbols. The vertical grey lines indicate the current density that was selected for the parametric studies on the influence of the gas-to-liquid ratio and the two-phase velocity, presented in Sections 3.3.3 and 3.3.4, respectively.

occurs through the thin lubrication film around the bubble, which is expected to dominate over the mass transfer from the bubble caps through the liquid electrolyte slugs. For low velocities (Ca < 0.04 and Re < 100), the bubble is expected to flatten out against the channel walls (see Section 3.3.1) with a nearly constant film thickness in the middle of the channel of around 0.05 times the characteristic channel length (herein around 100 µm) [56, 63, 64]. Hence, it is expected that the observed Faradaic efficiency of the H-cell and the flow cell operated under gas-liquid Taylor flow is comparable. While we observe that the H-cell outperforms the Taylor flow cell, we stress that the potential of the flow cell lies in the continuous operation and in increasing mass transfer by increas-

ing the operating pressure or decreasing the film thickness by decreasing the channel dimensions. Further, we note that the overall achieved Faradaic efficiency towards CO for both reactor types remains below reported values on silver foil [65], as further discussed in Section 3.3.5. However, as discussed above the silver gauze depicts the typical behaviour of kinetic and mass transfer controlled operating regimes (Figure 3.4b)) for a varying applied current. Hence, while the absolute Faradaic efficiency likely increases with optimising the electrode design, the reported trends are expected to remain unchanged. Therefore, we proceed in the following with a study on the influence of the gas-to-liquid ratio and two-phase velocity of the Taylor flow on the mass transfer related reactor performance in terms of Faradaic efficiency for a fixed current density of $-8.8\,\mathrm{mA\,cm^{-2}}$ as indicated by the grey lines in Figure 3.4, without further optimisation of the electrode design.

3.3.3. INFLUENCE OF THE GAS-TO-LIQUID RATIO

Figure 3.5 shows the influence of the gas-to-liquid ratio on the Faradaic efficiency at a fixed two-phase velocity $u_{TP} = 4.5\,\mathrm{cm\,s^{-1}}$ and current density $i_{tot} = 8.8\,\mathrm{mA\,cm^{-2}}$. For reference, measurements of CO_2-saturated single-phase flow (gas-to-liquid ratio of 0) are included for the same velocity and current density. In the Taylor flow configuration the Faradaic efficiency is roughly doubled compared to the single-phase flow. The Faradaic efficiency for a gas-to-liquid ratio of 0.25 and 0.5 remains unchanged with a slight increase for a gas-to-liquid ratio of 0.75.

We explain the observed behaviour as follows. The gaseous bubble length increases with increasing the gas-to-liquid ratio, as shown and discussed in Section 3.3.1. Therefore, the interfacial area for mass transfer from the gas bubble to the catalyst increases, while the area of the liquid slugs decreases. The mass transfer rate in the bubble region

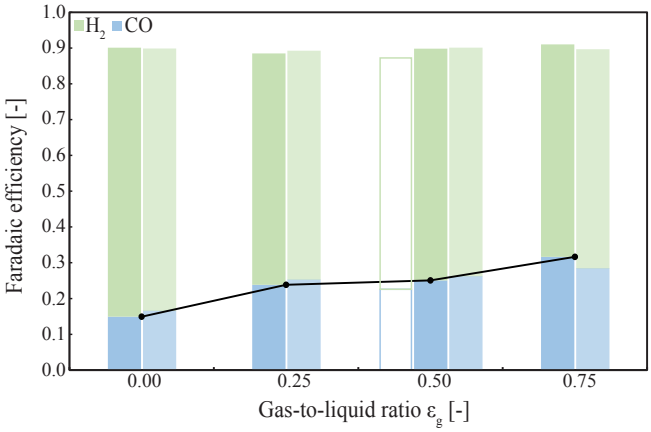

Figure 3.5: Influence of the gas-to-liquid ratio on the Faradaic efficiency towards CO and H_2 at a fixed two-phase velocity $u_{TP} = 4.5\,\mathrm{cm\,s^{-1}}$ ($\dot{Q}_{TP} = 10.8\,\mathrm{mL\,min^{-1}}$). The current was fixed to $I = -15\,\mathrm{mA}$ ($i_{tot} = -8.8\,\mathrm{mA\,cm^{-2}}$). Repeats are shown as the lighter coloured bars. The black line shows the observed trend. The open bars represent the closed data points for Taylor flow at $i_{tot} = -8.8\,\mathrm{mA\,cm^{-2}}$ in Figure 3.4a) and c).

is expected to remain constant for all gas-to-liquid ratios, while the mixing in shorter liquid slugs is intensified leading to an increased mass transfer rate for higher gas-to-liquid ratios. However, the increase in mass transfer rate and decline in liquid slug area seem to equal out such that only a minor influence of the gas-to-liquid on the Faradaic efficiency is observed, especially when considering the experimental error. This aligns with the observations from [35, 51, 66] in a thermocatalytic system. With the low observed conversion for the chosen conditions, no changes in bubble size over the channel length are observed (see Section 3.D (appendix)), such that other influences on the Faradaic efficiency such as residence time, alterations in two-phase velocity due to bubble shrinkage, and the influence of a locally increased pH can be neglected. We conclude that the influence of the bubble and slug region on the measured Faradaic efficiency is almost equal for all gas-to-liquid ratios. Higher gas-to-liquid ratios might still be favourable when operating at higher current densities where pH effects become significant. Therefore, in the following the influence of two-phase velocity on the Faradaic efficiency is studied for the largest gas-to-liquid ratio considered in this work, i.e., $\epsilon_g = 0.75$.

3.3.4. INFLUENCE OF THE TWO-PHASE VELOCITY

Figure 3.6 shows the influence of the two-phase velocity on the Faradaic efficiency at a fixed gas-to-liquid ratio $\epsilon_g = 0.75$ and current density $i_{tot} = -8.8\,\mathrm{mA\,cm^{-2}}$. For reference, measurements of CO_2-saturated single-phase flow (gas-to-liquid ratio of 0) are included for the same velocity and current density. For the single-phase flow and the Taylor flow the Faradaic efficiency towards CO increases when increasing the velocity, while the Faradaic efficiency towards H_2 decreases. Similar trends are observed for lower gas-to-liquid ratios (see Figure 3.12 (appendix)). Further, at the lowest velocities, the Faradaic efficiency towards CO is up to 4 times higher under Taylor flow conditions compared to the single–phase flow.

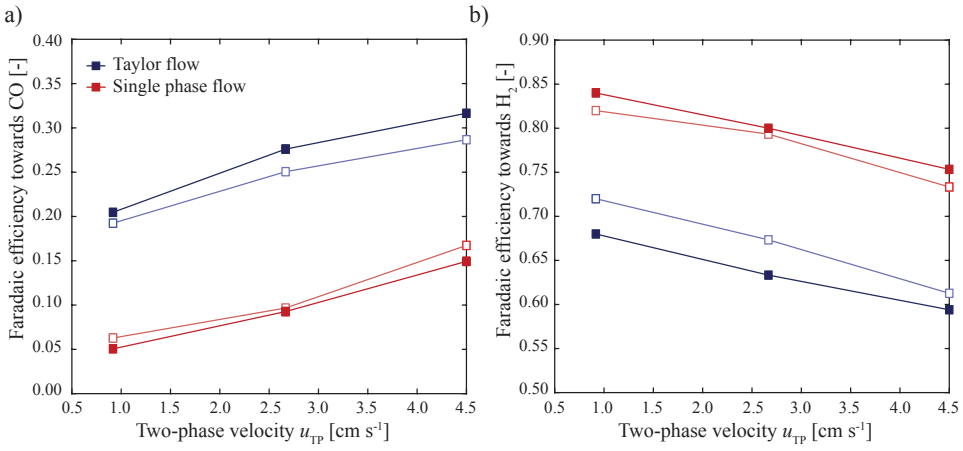

Figure 3.6: Influence of the (two-phase) velocity on the Faradaic efficiency towards CO a) and H_2 b) at a fixed gas-to-liquid ratio of 0 (single-phase flow, red) and of 0.75 (Taylor flow, blue). The current was fixed to $I = -15\,\mathrm{mA}$ ($i_{tot} = -8.8\,\mathrm{mA\,cm^{-2}}$). Repeats are shown as open symbols.

We explain the observed trend as follows. The lubrication film around the bubble is expected to remain nearly constant in thickness for all chosen two-phase velocities, as discussed in the previous Sections 3.3.2 and 3.3.3. However, the liquid slugs are expected to be fully developed with a parabolic flow profile, such that an increase in two-phase velocity intensifies mixing and decreases the diffusive boundary layer in this region leading to an increase in mass transfer rates [56, 57, 67]. This increase in mass transfer can be observed in the increase of the Faradaic efficiency towards CO with increasing the two-phase velocity. This indicates that the mass transfer via the bubble caps through the liquid slugs dominates over the mass transfer through the thin lubrication film, contrary to common observations especially in circular capillaries and the resulting mass transfer theories [56, 57, 68]. However, based on the difficulty to quantify the film thickness, the influence of the corner flow, the concentration in the liquid slugs, and the influence of the local pH, no conclusion on the leading phenomena for this can be drawn. Nonetheless, the experimental set-up with its transparent end plates would allow for more detailed studies of the influence of the velocity profile in the liquid slugs by for example Particle Image Velocimetry (PIV). Determining the CO_2 concentration in the liquid slugs through Fluorescence Lifetime Imaging (FLIM, [69]) measurements can give additional insights in the observed trends.

3.3.5. CONSIDERATIONS FOR THE ELECTRODE DESIGN

The goal of this work was to investigate to what extent injecting CO_2 into an electrolyser in the form of elongated Taylor bubbles enhances the electrochemical performance of the reactor. With the cell design presented, we have established that gas-liquid Taylor flow significantly enhances the Faradaic efficiency compared to CO_2-saturated liquid single-phase flow. To facilitate device design and fabrication, we chose to utilise a silver gauze as the cathode. Although the use of silver gauze facilitated a systematic study of the reactor performance on the Taylor flow features, the Faradaic efficiencies and current densities remained below industrially desired targets in both the H-cell and flow cell ($i_{CO} < 5\,mA\,cm^{-2}$ and $FE_{CO} < 35\%$). Thus, in this section we discuss how selection and design of the cathode can increase the current reactor performance.

As illustrated in Figure 3.7a), the silver gauze is pressed against a glassy carbon plate in the H-cell configuration. The glassy carbon is anticipated to catalyse the hydrogen evolution reaction within the tested potential range [70]. Due to the porous nature of the silver gauze the glassy carbon therefore can participate as a catalyst for the hydrogen evolution reaction, resulting in the increased Faradaic efficiency towards H_2 which we observe in our experiments. We expect that this is the main reason why the Faradaic efficiency towards CO on the silver gauze remains below reported values on silver foils. Lowering the required overpotential to drive the reaction on the silver gauze, for instance, by roughening the catalyst surface [71–73], is expected to further enhance the selectivity. Although these catalyst activation methods are also anticipated to enhance the overall Faradaic efficiency in the flow cell, discrepancies in the local reaction environment between the H-cell and flow cell suggest that additional considerations are necessary when designing the electrode for the flow cell.

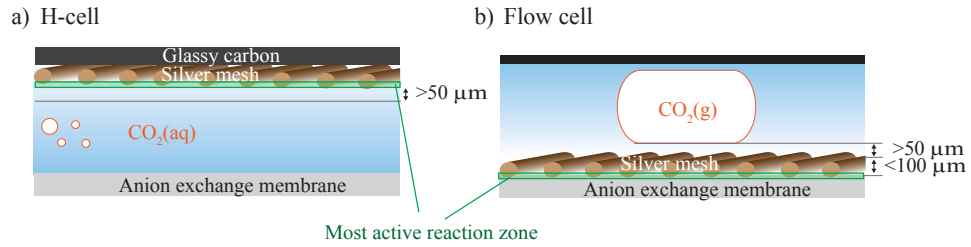

Figure 3.7: Representation of a) the cathode chamber in the H-cell configuration including the expected thickness of the diffusion layer close to the electrode and b) a unit cell with a gaseous CO_2 Taylor bubble flowing past the silver gauze with the expected liquid film and mesh thickness as the diffusion distance for the CO_2 to reach the most reactive zone in the electrolyser.

Typically, the most active reaction zone in the electrolyser is where the reactant CO_2, ions (OH^- or H^+), and electrons meet, which in the flow cell is proximate to the membrane as depicted in Figure 3.7 b). Consequently, we anticipate that the mesh thickness adds an additional resistance to the mass transfer of dissolved CO_2 to the reaction zone, resulting in the previously reported higher partial current densities towards CO observed in the H-cell compared to the flow cell (Figure 3.4). Catalyst-coated membranes [74] could potentially reduce the diffusion distance for CO_2 in the liquid electrolyte to the catalyst sites while concurrently benefiting from improved reactivity on nanoporous catalyst structures [73]. However, ensuring good electrical conductivity and mechanical stability of the catalyst particles under flow conditions while mitigating any additional diffusion layer will pose a challenge.

3.4. CONCLUSION

We demonstrate how gas-liquid Taylor flow influences the Faradaic efficiency (selectivity) for the mass transfer limited electrochemical CO_2 reduction reaction to CO in a zero-gap membrane electrolyser design. We find that a shift from single-phase liquid electrolyte flow to gas-liquid (CO_2-electrolyte) Taylor flow doubles the Faradaic efficiency towards CO formation. Further, we show that the gas-to-liquid ratio (the amount of gaseous CO_2 to liquid electrolyte) does not significantly influence the Faradaic efficiency, while increasing the two-phase velocity increases the Faradaic efficiency towards CO. Our findings indicate that the liquid electrolyte slugs are fully saturated with CO_2 and are the main contributor to mass transfer. Therefore, the observed influence of the flow features is contrary to general trends of Taylor flow in thermo-catalytic flow channels. This resonates with the work from Haase *et al.* [51], who show a similar mismatch between the expected and observed influence of the Taylor flow features on Faradaic efficiency for low Capillary and Reynolds numbers ($Ca < 0.04$ & $Re < 100$). We believe that the presented electrolyser design with its transparent design can be a valuable tool to gain a better understanding of the mass transfer at low two-phase velocities in Taylor flow as it allows to capture the hydrodynamics over the entire channel length during the reaction. The zero-gap membrane electrolyser design can be operated under pressure, which would further increase the mass transfer rate. Additionally, our results indicate

that optimisation of the membrane electrode assembly (MEA) can reduce mass transfer limitations arising from the electrode structure. Further, the current density (reaction rate) can be varied by the applied voltage such that the influence of conversion on the flow could be studied as well. The insights from this are expected to be translatable to applications in the field of electrochemical, photoelectrochemical and thermo-catalytic processes.

Table 3.1: List of symbols.

Symbol	Description	Unit
Latin letters		
A	Electrode area	m^2
Ca	Capillary number	-
Cr_i	Gas correction factor for species i	-
F	Faraday constant	$\mathrm{A\,s\,mol}^{-1}$
FE_i	Faradaic efficiency towards species i	-
H	Channel height	m
I	Applied current	A
i_i	Partial current density towards species i	$\mathrm{A\,m}^{-2}$
i_tot	Applied current density	$\mathrm{A\,m}^{-2}$
L	Channel length of flow cell	m
L_B	Bubble length	m
L_S	Slug length	m
L_UC	Unit cell length	m
$\dot{n}_\mathrm{i}$	Molar flow rate of species i	$\mathrm{mol\,s}^{-1}$
p	Pressure	bar
$\dot{Q}_\mathrm{g}$	Gas flow rate	$\mathrm{mL\,min}^{-1}$
$\dot{Q}_\mathrm{l}$	Electrolyte flow rate	$\mathrm{mL\,min}^{-1}$
$\dot{Q}_\mathrm{TP}$	Sum of gas and liquid inlet flow rate	$\mathrm{mL\,min}^{-1}$
R	Universal gas constant	$\mathrm{J\,mol}^{-1}\,\mathrm{K}^{-1}$
Re	Reynolds number	-
T	Temperature	K
u_g	Superficial gas velocity	$\mathrm{m\,s}^{-1}$
u_l	Superficial electrolyte velocity	$\mathrm{m\,s}^{-1}$
u_TP	Two-phase velocity	$\mathrm{m\,s}^{-1}$
V_B	Volume of the gas bubble	m^3
V_L	Volume of the an individual liquid electrolyte slug	m^3
υ_i	Volume fraction of species i	-
$\dot{V}$	Volumetric flow rate	$\mathrm{m}^3\,\mathrm{s}^{-1}$
W	Channel width	m
x_i	Mol fraction of species i	-
Greek letters		
γ	Interfacial tension	$\mathrm{N\,m}^{-1}$
ϵ_g	Gas-to-liquid ratio	-
μ_l	Dynamic viscosity of liquid electrolyte	Pa s
ν	Bubble generation frequency	s^{-1}
ρ_l	Density of liquid electrolyte	$\mathrm{kg\,m}^{-3}$

APPENDIX

3.A. CALCULATIONS OF THE FARADAIC EFFICIENCY FROM GC MEASUREMENTS

The Faradaic efficiency of the gaseous products are estimated based on the mole fractions of CO_2, Ar, CO, and H_2 from the gas chromatograph (GC) injections. Five GC injections were taken over a time frame of 15 min, 10 min after starting the electrochemical measurement. This time was chosen based on preliminary experiments, which showed that no significant (< 5%) change in volume fraction for all gaseous products was observed after the initial 10 min. The gases are assumed to behave ideal, therefore the volume fraction of gaseous products from the GC is equal to the mole fraction. Since the sum of mole fractions is equal to 1, the mole fraction of water vapour x_{H_2O} in the gas stream is calculated as

$$x_{H_2O} = 1 - (x_{CO_2} + x_{Ar} + x_{CO} + x_{H_2}). \tag{3.4}$$

The molar flow rate $\dot{n}_i$ of each product i is then calculated based on the mole fraction x_i and the volumetric flow rate at the reactor outlet $\dot{V}_{outlet}$, which was measured with the mass flow meter (see Figure 3.2), as

$$\dot{n}_i = \frac{p\dot{V}_{outlet}x_i}{RT}. \tag{3.5}$$

Since the mass flow meter is calibrated for CO_2 the gas flow rate first needs to be corrected based on the gas composition. For this a correction factor Cr_{mix} based on the gas conversion factor Cr_i (see Table 3.2) and volume fraction $v_i = x_i$ for each of the components i in the gas is used

$$\frac{1}{Cr_{mix}} = \sum \frac{v_i}{Cr_i}. \tag{3.6}$$

The correction factor is then used to calculate the outlet flow rate $\dot{V}_{outlet}$ based on the measured flow rate $\dot{V}_{measured}$

$$\dot{V}_{outlet} = \dot{V}_{measured}\frac{Cr_{mix}}{Cr_{CO_2}}. \tag{3.7}$$

The Faradaic efficiency for the gaseous products CO and H_2 is calculated as

$$FE_{CO} = \frac{2\dot{n}_{CO}F}{I}, \tag{3.8}$$

$$FE_{H_2} = \frac{2\dot{n}_{H_2}F}{I}, \tag{3.9}$$

with the molar flow rate $\dot{n}_{CO/H_2}$ of CO/H_2 (Eq. 3.5), the Faraday constant F, the applied current I and 2 as the number of electrons required per reaction. Liquid samples were not taken, such that the Faradaic efficiency towards $HCOOH^-$ could not be determined.

Table 3.2: Gas conversion factors for components in gas stream to the GC [75].

Species	**Conversion factor** Cr_i
CO	1
CO_2	0.74
H_2	1.01
H_2O	0.79
Ar	1.4

3.B. CHARACTERISATION OF THE CATHODE

The silver gauze is tested in a flow-through H-cell [76]. In the cell, the silver gauze is pressed against a glassy carbon plate to ensure electrical contact and avoid leakages. The experiments are performed in a three-electrode configuration using a leakless miniature Ag/AgCl reference electrode and a platinum foil as the anode. The gaseous CO_2 is bubbled into the bottom of the flow cell with a constant flow rate of $8\,mL\,min^{-1}$, and the outlet gas-stream is analysed continuously via GC injections following the same procedure as described in Section 3.2.2. Before each experiment, the ohmic resistance is measured and used to correct the applied cathode potential.

The measured Faradaic efficiency towards CO/H_2 and total current density for each applied potential is shown in Figure 3.8. For all potentials, the sum of the Faradaic efficiency remains around 80%. Since the liquid products were not analysed, we expect that formic acid is formed in the liquid phase. Further, due to the low quantities of product gases, we expect a measurement error in flow rate correction of up to 5%. The highest achieved Faradaic efficiency towards CO is around 30% at a potential of $-1.27\,V$ vs reversible hydrogen electrode (RHE) with a total current density of around $-14\,mA\,cm^{-2}$. Similar to silver foils with a polycrystalline surface, the required overpotential to drive the reaction is higher compared to nanoporous silver catalysts [71–73]. Analysing the surface structure of the silver gauze using a JEOL JSM 6010LA (JEOL, Tokyo, Japan) scanning electron microscope (SEM), utilising both secondary and back-scattered electrons for imaging (SEI and BEC images in Figure 3.9), we do indeed see a defective polycrystalline surface, which remains relatively unchanged after the electrochemical experiments as shown in Figure 3.9. The secondary electron SEM images reveal the rough surface of the silver gauze, which is most likely a result of its production process, and this roughness remains moderately unchanged after electrolysis. The back-scattered electrons SEM images, on the other hand, depict the polycrystalline structure of the employed silver gauze for electrolysis.

However, the Faradaic efficiency towards CO remains way below the commonly observed 80-90% on silver foil [65, 71–73]. We believe that this stems from the glassy carbon participating in the electrochemical reaction forming hydrogen. Han *et al.* [70] showed that the hydrogen evolution has an onset potential of around $-1.00\,V$ vs RHE on bare glassy carbon. Further, the local pH in the porous structure of the silver gauze will certainly be higher compared to the surface near a flat silver foil, further decreasing the availability of CO_2.

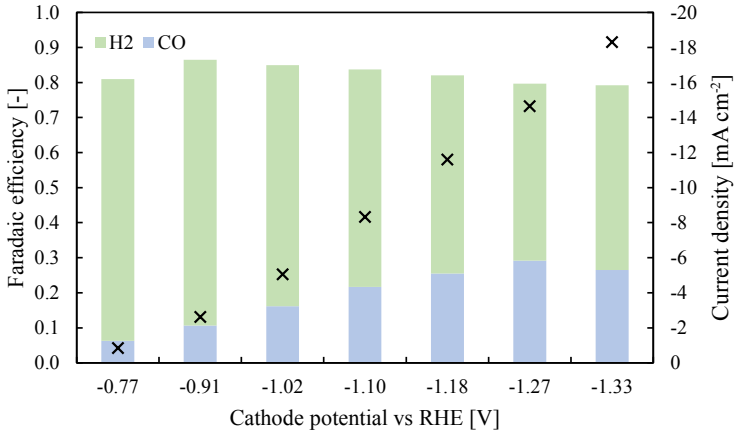

Figure 3.8: Faradaic efficiency (bars) and measured current density (crosses) over cathode potential vs RHE measured in an H-cell configuration for a silver gauze pressed onto a glassy carbon plate.

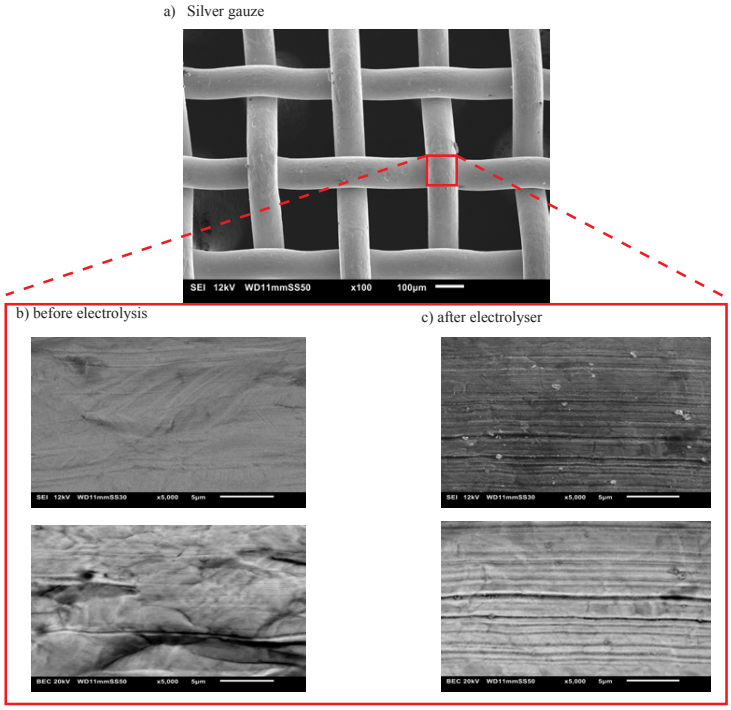

Figure 3.9: SEI and BEC image of silver gauze a), zoomed in region before b) and after c) the electrochemical experiments.

3.C. OBSERVED TAYLOR FLOW

Figure 3.10 shows the stable Taylor flow for a gas-to-liquid ratio ϵ_g of 0.25 and 0.5 for the two-phase velocities $u_{TP} = 0.9$ and $2.7\,\mathrm{cm\,s^{-1}}$.

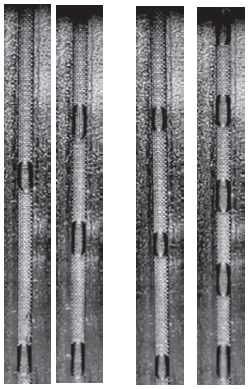

Figure 3.10: Photographs of the observed Taylor flow for a varying gas-to-liquid ratio ϵ_g and a varying two-phase velocity u_{TP}.

3.D. CONVERSION AND FARADAIC EFFICIENCY

The conversion is given by the ratio of CO_2 flow rate into the reactor and the outlet flow rate of CO [77], which for all three cases (H-cell, single phase flow and Taylor flow) remains below 5 %. We further see no significant change in bubble to unit cell length for the Taylor flow set-up before starting the electrolysis and during the electrochemical reduction of CO_2 as shown in Figure 3.11.

The Faradaic efficiency towards CO and H_2 for varying two-phase velocity and gas-to-liquid ratio of 0.25 and 0.5 is shown in Figure 3.12. Similar to the influence for a gas-to-liquid-ratio 0.75 (Section 3.3.4), the Faradaic efficiency towards CO increases when increasing the two-phase velocity.

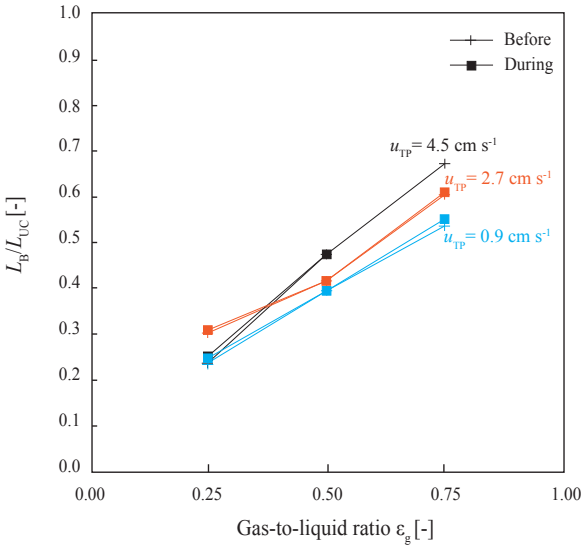

Figure 3.11: Experimentally measured gas bubble to unit cell length ratio at the inlet of the reactor over the gas-to-liquid ratio without the electrochemical reaction (before) and with the electrochemical reaction (during).

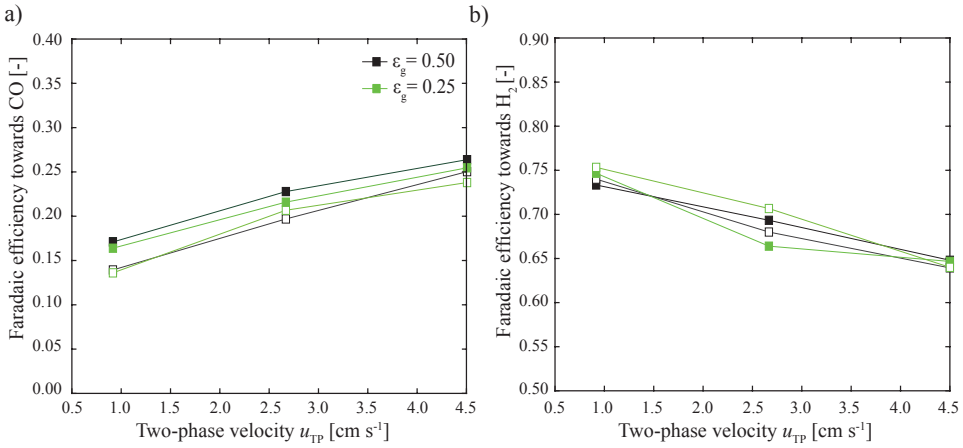

Figure 3.12: Faradaic efficiency towards CO a) and H_2 b) for a gas-to-liquid ratio ϵ_g of 0.25 and of 0.50 (Taylor flow). Repeats are shown as open symbols.

REFERENCES

[1] F. Barbir, *PEM electrolysis for production of hydrogen from renewable energy sources,* Solar Energy **78**, 661 (2005).

[2] R. Clarke, S. Giddey, F. Ciacchi, S. Badwal, B. Paul, and J. Andrews, *Direct coupling of an electrolyser to a solar PV system for generating hydrogen,* International Journal of Hydrogen Energy **34**, 2531 (2009).

[3] D. Tang, G.-L. Tan, G.-W. Li, J.-G. Liang, S. M. Ahmad, A. Bahadur, M. Humayun, H. Ullah, A. Khan, and M. Bououdina, *State-of-the-art hydrogen generation techniques and storage methods: A critical review,* Journal of Energy Storage **64**, 107196 (2023).

[4] D. Niblett, M. Delpisheh, S. Ramakrishnan, and M. Mamlouk, *Review of next generation hydrogen production from offshore wind using water electrolysis,* Journal of Power Sources **592**, 233904 (2024).

[5] B. Kumar, J. P. Brian, V. Atla, S. Kumari, K. A. Bertram, R. T. White, and J. M. Spurgeon, *New trends in the development of heterogeneous catalysts for electrochemical CO_2 reduction,* Catalysis Today **270**, 19 (2016).

[6] M. G. Kibria, J. P. Edwards, C. M. Gabardo, C.-T. Dinh, A. Seifitokaldani, D. Sinton, and E. H. Sargent, *Electrochemical CO_2 reduction into chemical feedstocks: From mechanistic electrocatalysis models to system design,* Advanced Materials **31**, 1807166 (2019).

[7] R. Masel, Z. Liu, H. Yang, J. J. Kaczur, D. Carrillo, R. Shaoxuan, D. Salvatore, and C. P. Berlinguette, *An industrial perspective on catalysts for low-temperature CO_2 electrolysis,* Nature Nanotechnology **16**, 118–128 (2021).

[8] H. Ito, T. Maeda, A. Nakano, Y. Hasegawa, N. Yokoi, C. Hwang, M. Ishida, A. Kato, and T. Yoshida, *Effect of flow regime of circulating water on a proton exchange membrane electrolyzer,* International Journal of Hydrogen Energy **35**, 9550 (2010).

[9] M. Carmo, D. L. Fritz, J. Mergel, and D. Stolten, *A comprehensive review on PEM water electrolysis,* International Journal of Hydrogen Energy **38**, 4901 (2013).

[10] D. Bessarabov and P. Millet, *The individual proton-exchange membrane cell and proton-exchange membrane stack,* in *PEM water electrolysis*, Hydrogen and fuel cells primers series (Elsevier Science & Technology, 2018) pp. 75–116, 1st ed.

[11] A. C. Olesen, S. H. Frensch, and S. K. Kær, *Towards uniformly distributed heat, mass and charge: A flow field design study for high pressure and high current density operation of PEM electrolysis cells,* Electrochimica Acta **293**, 476 (2019).

[12] I. Merino-Garcia, E. Alvarez-Guerra, J. Albo, and A. Irabien, *Electrochemical membrane reactors for the utilisation of carbon dioxide,* Chemical Engineering Journal **305**, 104 (2016).

[13] S. Verma, B. Kim, H.-R. M. Jhong, S. Ma, and P. J. A. Kenis, *A gross-margin model for defining technoeconomic benchmarks in the electroreduction of CO_2,* Chemistry-Sustainability-Energy-Materials **9**, 1972 (2016).

[14] B. Endrődi, G. Bencsik, F. Darvas, R. Jones, K. Rajeshwar, and C. Janáky, *Continuous-flow electroreduction of carbon dioxide,* Progress in Energy and Combustion Science **62**, 133 (2017).

[15] S. Garg, M. Li, A. Z. Weber, L. Ge, L. Li, V. Rudolph, G. Wang, and T. E. Rufford, *Advances and challenges in electrochemical CO_2 reduction processes: An engineering and design perspective looking beyond new catalyst materials,* Journal of Materials Chemistry A **8**, 1511 (2020).

[16] D. M. Weekes, D. A. Salvatore, A. Reyes, A. Huang, and C. P. Berlinguette, *Electrolytic CO_2 reduction in a flow cell,* Accounts of Chemical Research **51**, 910 (2018).

[17] T. Burdyny and W. A. Smith, *CO_2 reduction on gas-diffusion electrodes and why catalytic performance must be assessed at commercially-relevant conditions,* Energy & Environmental Science **12**, 1442 (2019).

[18] K. Hara and T. Sakata, *Large current density CO_2 reduction under high pressure using gas diffusion electrodes,* Bulletin of the Chemical Society of Japan **70**, 571 (2006).

[19] E. J. Dufek, T. E. Lister, S. G. Stone, and M. E. McIlwain, *Operation of a pressurized system for continuous reduction of CO_2,* Journal of The Electrochemical Society **159**, F514 (2012).

[20] B. Endrődi, E. Kecsenovity, A. Samu, F. Darvas, R. V. Jones, V. Török, A. Danyi, and C. Janáky, *Multilayer electrolyzer stack converts carbon dioxide to gas products at high pressure with high efficiency,* ACS Energy Letters **4**, 1770 (2019).

[21] A. Morrison, N. Girichandran, Q. Wols, and R. Kortlever, *Design of an elevated pressure electrochemical flow cell for CO_2 reduction,* Journal of Applied Electrochemistry **53**, 2321–2330 (2023).

[22] Y. Tomita, S. Teruya, O. Koga, and Y. Hori, *Electrochemical reduction of carbon dioxide at a platinum electrode in acetonitrile-water mixtures,* Journal of The Electrochemical Society **147**, 4164 (2000).

[23] J. Shi, F.-X. Shen, F. Shi, N. Song, Y.-J. Jia, Y.-Q. Hu, Q.-Y. Li, J.-X. Liu, T.-Y. Chen, and Y.-N. Dai, *Electrochemical reduction of CO_2 into CO in tetrabutylammonium perchlorate/propylene carbonate: Water effects and mechanism,* Electrochimica Acta **240**, 114 (2017).

[24] Y. Matsubara, D. C. Grills, and Y. Kuwahara, *Thermodynamic aspects of electrocatalytic CO_2 reduction in acetonitrile and with an ionic liquid as solvent or electrolyte,* ACS Catalysis **5**, 6440 (2015).

[25] A. S. Kumar, M. Pupo, K. V. Petrov, M. Ramdin, J. R. van Ommen, W. de Jong, and R. Kortlever, *A quantitative analysis of electrochemical CO_2 reduction on copper in organic amide and nitrile-based electrolytes,* The Journal of Physical Chemistry C **127**, 12857 (2023).

[26] D. Higgins, C. Hahn, C. Xiang, T. F. Jaramillo, and A. Z. Weber, *Gas-diffusion electrodes for carbon dioxide reduction: A new paradigm,* ACS Energy Letters **4**, 317 (2019).

[27] J.-B. Vennekoetter, R. Sengpiel, and M. Wessling, *Beyond the catalyst: How electrode and reactor design determine the product spectrum during electrochemical CO_2 reduction,* Chemical Engineering Journal **364**, 89 (2019).

[28] Endrődi, B. and Samu, A. and Kecsenovity, E. and Halmágyi, T. and Sebők, D. and Janáky,C., *Operando cathode activation with alkali metal cations for high current density operation of water-fed zero-gap carbon dioxide electrolysers,* Nature Energy **6**, 439–448 (2021).

[29] L.-C. Weng, A. T. Bell, and A. Z. Weber, *Towards membrane-electrode assembly systems for CO_2 reduction: A modeling study,* Energy & Environmental Science **12**, 1950 (2019).

[30] A. Reyes, R. P. Jansonius, B. A. W. Mowbray, Y. Cao, D. G. Wheeler, J. Chau, D. J. Dvorak, and C. P. Berlinguette, *Managing hydration at the cathode enables efficient CO_2 electrolysis at commercially relevant current densities,* ACS Energy Letters **5**, 1612 (2020).

[31] D. G. Wheeler, B. A. W. Mowbray, A. Reyes, F. Habibzadeh, J. He, and C. P. Berlinguette, *Quantification of water transport in a CO_2 electrolyzer,* Energy & Environmental Science **13**, 5126 (2020).

[32] K. V. Petrov, J. C. Bui, L. Baumgartner, L.-C. Weng, S. M. Dischinger, D. M. Larson, D. J. Miller, A. Z. Weber, and D. A. Vermaas, *Anion-exchange membranes with internal microchannels for water control in CO_2 electrolysis,* Sustainable Energy Fuels **6**, 5077 (2022).

[33] I. Bagemihl, C. Bhatraju, J. R. van Ommen, and V. van Steijn, *Electrochemical reduction of CO_2 in tubular flow cells under gas–liquid Taylor flow,* ACS Sustainable Chemistry & Engineering **10**, 12580 (2022).

[34] F. Zhang, C. Chen, Y. Tang, and Z. Cheng, *CO_2 reduction in a microchannel electrochemical reactor with gas-liquid segmented flow,* Chemical Engineering Journal **392**, 124798 (2020).

[35] T. Nijhuis, M. Kreutzer, A. Romijn, F. Kapteijn, and J. Moulijn, *Monolithic catalysts as efficient three-phase reactors,* Chemical Engineering Science **56**, 823 (2001).

[36] A. Karim, J. Bravo, D. Gorm, T. Conant, and A. Datye, *Comparison of wall-coated and packed-bed reactors for steam reforming of methanol,* Catalysis Today **110**, 86 (2005).

[37] M. Atobe, H. Tateno, and Y. Matsumura, *Applications of flow microreactors in electrosynthetic processes,* Chemical Reviews **118**, 4541 (2018).

[38] Y. Cao, C. Soares, N. Padoin, and T. Noël, *Gas bubbles have controversial effects on Taylor flow electrochemistry,* Chemical Engineering Journal **406**, 126811 (2021).

[39] V. Lawlor, S. Griesser, G. Buchinger, A. Olabi, S. Cordiner, and D. Meissner, *Review of the micro-tubular solid oxide fuel cell: Part I. stack design issues and research activities,* Journal of Power Sources **193**, 387 (2009).

[40] A. Buttler and H. Spliethoff, *Current status of water electrolysis for energy storage, grid balancing and sector coupling via power-to-gas and power-to-liquids: A review,* Renewable and Sustainable Energy Reviews **82**, 2440 (2018).

[41] I. Vincent and D. Bessarabov, *Low cost hydrogen production by anion exchange membrane electrolysis: A review,* Renewable and Sustainable Energy Reviews **81**, 1690 (2018).

[42] M. Bonanno, K. Müller, B. Bensmann, R. Hanke-Rauschenbach, D. Aili, T. Franken, A. Chromik, R. Peach, A. T. S. Freiberg, and S. Thiele, *Review and prospects of PEM water electrolysis at elevated temperature operation,* Advanced Materials Technologies **9**, 2300281 (2024).

[43] W. Liu, S. Roy, and X. Fu, *Gas–liquid catalytic hydrogenation reaction in small catalyst channel,* AIChE Journal **51**, 2285 (2005).

[44] R. Natividad, J. Cruz-Olivares, R. Fishwick, J. Wood, and J. Winterbottom, *Scaling-out selective hydrogenation reactions: From single capillary reactor to monolith,* Fuel **86**, 1304 (2007).

[45] A. K. Mogalicherla and D. Kunzru, *Effect of gas and liquid superficial velocities on the performance of monolithic reactors,* Industrial & Engineering Chemistry Research **49**, 1631 (2010).

[46] D. Liu, J. Zhang, D. Li, Q. Kong, T. Zhang, and S. Wang, *Hydrogenation of 2-ethylanthraquinone under Taylor flow in single square channel monolith reactors,* AIChE Journal **55**, 726 (2009).

[47] R. P. Fishwick, R. Natividad, R. Kulkarni, P. A. McGuire, J. Wood, J. M. Winterbottom, and E. H. Stitt, *Selective hydrogenation reactions: A comparative study of monolith cdc, stirred tank and trickle bed reactors,* Catalysis Today **128**, 108 (2007).

[48] R. Natividad, R. Kulkarni, K. Nuithitikul, S. Raymahasay, J. Wood, and J. Winterbottom, *Analysis of the performance of single capillary and multiple capillary (monolith) reactors for the multiphase Pd-catalyzed hydrogenation of 2-butyne-1,4-diol,* Chemical Engineering Science **59**, 5431 (2004).

[49] G. Berčič, *Influence of operating conditions on the observed reaction rate in the single channel monolith reactor,* Catalysis Today **69**, 147 (2001).

[50] S. Haase and T. Bauer, *New method for simultaneous measurement of hydrodynamics and reaction rates in a mini-channel with Taylor flow,* Chemical Engineering Journal **176-177**, 65 (2011).

[51] S. Haase, T. Bauer, G. Hilpmann, M. Lange, M. Ayubi, and R. Abiev, *Simultaneous detection of hydrodynamics, mass transfer and reaction rates in a three–phase microreactor,* Theoretical Foundations of Chemical Engineering **54**, 48 (2020).

[52] J. O. Majasan, J. I. Cho, I. Dedigama, D. Tsaoulidis, P. Shearing, and D. J. Brett, *Two-phase flow behaviour and performance of polymer electrolyte membrane electrolysers: Electrochemical and optical characterisation,* International Journal of Hydrogen Energy **43**, 15659 (2018).

[53] I. Dedigama, P. Angeli, K. Ayers, J. Robinson, P. Shearing, D. Tsaoulidis, and D. Brett, *In situ diagnostic techniques for characterisation of polymer electrolyte membrane water electrolysers – flow visualisation and electrochemical impedance spectroscopy,* International Journal of Hydrogen Energy **39**, 4468 (2014).

[54] T. Hatsukade, K. P. Kuhl, E. R. Cave, D. N. Abram, and T. F. Jaramillo, *Insights into the electrocatalytic reduction of CO_2 on metallic silver surfaces,* Physical Chemistry Chemical Physics **16**, 13814 (2014).

[55] S. Verma, X. Lu, S. Ma, R. I. Masel, and P. J. A. Kenis, *The effect of electrolyte composition on the electroreduction of CO_2 to CO on Ag based gas diffusion electrodes,* Physical Chemistry Chemical Physics **18**, 7075 (2016).

[56] M. T. Kreutzer, F. Kapteijn, J. A. Moulijn, and J. J. Heiszwolf, *Multiphase monolith reactors: Chemical reaction engineering of segmented flow in microchannels,* Chemical Engineering Science **60**, 5895 (2005).

[57] S. Haase, D. Y. Murzin, and T. Salmi, *Review on hydrodynamics and mass transfer in minichannel wall reactors with gas–liquid Taylor flow,* Chemical Engineering Research and Design **113**, 304 (2016).

[58] P. Korczyk, V. van Steijn, S. Blonski, D. Zaremba, D. A. Beattie, and P. Garstecki, *Accounting for corner flow unifies the understanding of droplet formation in microfluidic channels,* Nature Communications **10**, 2528 (2019).

[59] R. Kas, A. G. Star, K. Yang, T. Van Cleve, K. C. Neyerlin, and W. A. Smith, *Along the channel gradients impact on the spatioactivity of gas diffusion electrodes at high conversions during CO_2 electroreduction,* ACS Sustainable Chemistry & Engineering **9**, 1286 (2021).

[60] I. Bagemihl, L. Cammann, M. Pérez-Fortes, V. van Steijn, and J. R. van Ommen, *Techno-economic assessment of CO_2 electrolysis: How interdependencies between model variables propagate across different modeling scales,* ACS Sustainable Chemistry & Engineering **11**, 10130 (2023).

[61] R. Gupta, D. F. Fletcher, and B. S. Haynes, *On the CFD modelling of Taylor flow in microchannels,* Chemical Engineering Science **64**, 2941 (2009).

[62] T. Burdyny and W. A. Smith, *CO_2 reduction on gas-diffusion electrodes and why catalytic performance must be assessed at commercially-relevant conditions,* Energy and Environmental Science **12**, 1442 (2019).

[63] T. Thulasidas, M. Abraham, and R. Cerro, *Bubble-train flow in capillaries of circular and square cross section,* Chemical Engineering Science **50**, 183 (1995).

[64] M. T. Kreutzer, *Gas component mass transfer,* in *Hydrodynamics of Taylor flow in capillaries and monolith reactors* (Delft University Press, 2003).

[65] N. Hoshi, M. Kato, and Y. Hori, *Electrochemical reduction of CO_2 on single crystal electrodes of silver Ag(111), Ag(100) and Ag(110),* Journal of Electroanalytical Chemistry **440**, 283 (1997).

[66] M. T. Kreutzer, P. Du, J. J. Heiszwolf, F. Kapteijn, and J. A. Moulijn, *Mass transfer characteristics of three-phase monolith reactors,* Chemical Engineering Science **56**, 6015 (2001).

[67] T. Thulasidas, M. Abraham, and R. Cerro, *Flow patterns in liquid slugs during bubble-train flow inside capillaries,* Chemical Engineering Science **52**, 2947 (1997).

[68] R. Gupta, D. Fletcher, and B. Haynes, *Taylor flow in microchannels: A review of experimental and computational work,* The Journal of Computational Multiphase Flows **2**, 1 (2010).

[69] J. Bleeker, A. P. Kahn, L. M. Baumgartner, F. C. Grozema, D. A. Vermaas, and W. F. Jager, *Quinolinium-based fluorescent probes for dynamic pH monitoring in aqueous media at high pH using fluorescence lifetime imaging,* ACS Sensors **8**, 2050 (2023).

[70] K. Han, P. Ngene, and P. de Jongh, *Structure dependent product selectivity for CO_2 electroreduction on ZnO derived catalysts,* ChemCatChem **13**, 1998 (2021).

[71] L. Q. Zhou, C. Ling, M. Jones, and H. Jia, *Selective CO_2 reduction on a polycrystalline ag electrode enhanced by anodization treatment,* Chemical Communications **51**, 17704 (2015).

[72] M. Ma, B. J. Trześniewski, J. Xie, and W. A. Smith, *Selective and efficient reduction of carbon dioxide to carbon monoxide on oxide-derived nanostructured silver electrocatalysts,* Angewandte Chemie International Edition **55**, 9748 (2016).

[73] H. Mistry, Y.-W. Choi, A. Bagger, F. Scholten, C. S. Bonifacio, I. Sinev, N. J. Divins, I. Zegkinoglou, H. S. Jeon, K. Kisslinger, E. A. Stach, J. C. Yang, J. Rossmeisl, and B. Roldan Cuenya, *Enhanced carbon dioxide electroreduction to carbon monoxide over defect-rich plasma-activated silver catalysts,* Angewandte Chemie International Edition **56**, 11394 (2017).

[74] G. Díaz-Sainz, M. Alvarez-Guerra, J. Solla-Gullón, L. García-Cruz, V. Montiel, and A. Irabien, *Catalyst coated membrane electrodes for the gas phase CO_2 electroreduction to formate,* Catalysis Today **346**, 58 (2020).

[75] Bronkhorst, *General instructions digital mass flow / pressure instruments laboratory style / IN-FLOW,* (2021).

[76] P. Lobaccaro, M. R. Singh, E. L. Clark, Y. Kwon, A. T. Bell, and J. W. Ager, *Effects of temperature and gas–liquid mass transfer on the operation of small electrochemical cells for the quantitative evaluation of CO_2 reduction electrocatalysts,* Physical Chemistry Chemical Physics **18**, 26777 (2016).

[77] S. S. Bhargava, F. Proietto, D. Azmoodeh, E. R. Cofell, D. A. Henckel, S. Verma, C. J. Brooks, A. A. Gewirth, and P. J. A. Kenis, *System design rules for intensifying the electrochemical reduction of CO_2 to CO on Ag nanoparticles,* ChemElectroChem **7**, 2001 (2020).

4

TECHNO–ECONOMIC ASSESSMENT OF CO_2 ELECTROLYSIS: HOW INTERDEPENDENCIES BETWEEN MODEL VARIABLES PROPAGATE ACROSS DIFFERENT MODELLING SCALES.

This chapter has been published in ACS Sustainable Chemistry & Engineering **11**, 27 (2023) [1].

The production of base chemicals by electrochemical conversion of captured CO_2 has the potential to close the carbon cycle, thereby contributing to the future energy transition. With the feasibility of low-temperature electrochemical CO_2 conversion demonstrated at lab scale, research is shifting towards optimising electrolyser design and operation for industrial applications, with target values based on techno-economic analysis. However, current techno–economic analyses often neglect experimentally reported interdependencies of key performance variables such as the current density, the Faradaic efficiency, and the conversion. Aiming to understand the impact of these interdependencies on the economic outlook, we develop a model capturing mass transfer effects over the channel length for an alkaline, membrane electrolyser. Coupling the channel scale with the higher level process scale and embedding this multi–scale model in an economic framework allows us to analyse the economic trade-off between the performance variables. Our analysis shows that the derived target values for the performance variables strongly depend on the interdependencies described in the channel scale model. Our analysis also suggests that economically optimal current densities can be as low as half of the previously reported benchmarks. More generally, our work highlights the need to move towards multi–scale models, especially in the field of CO_2 electrolysis, to effectively elucidate current bottlenecks in the quest toward economically compelling system designs.

4.1. INTRODUCTION

The current anthropogenic carbon economy does not possess the ability to reduce CO_2. Instead, it solely oxidises various fossil-based carbon sources to CO_2, leading to increasing atmospheric concentrations. Closing the carbon cycle by converting waste CO_2 to bulk chemicals is a promising avenue to minimise emissions and fossil-based resource consumption[2, 3]. One technology offering the potential of achieving this transition is the electrochemical conversion of CO_2 [4, 5]. Techno-economic studies have led researchers to identify target values for performance variables [6–8] and pathways toward the profitable deployment of this emerging technology [9–13].

The first techno-economic analyses studied the economic feasibility of electrochemical CO_2 reduction by presenting target values for the performance variables to reach a break-even point[6, 7]. These performance variables include the current density, the Faradaic efficiency, and the cell potential, while the conversion rate is fixed [6, 7, 14, 15]. Importantly, these variables are usually assumed to be independent [6–8, 14, 16]. Under this assumption, the threshold values for the first three variables were derived utilising a generalised electrochemical CO_2 reduction plant model based on a fixed conversion rate and price indication for existing electrolyser technologies [6, 7, 14]. The derived thresholds include current densities above 250-300 $mA\,cm^{-2}$ and cell potentials below 1.8 V to reduce capital and operational costs of the electrolyser unit, respectively [7, 14]. Further, Faradaic efficiencies above 80-90% reduce downstream separation costs of the product [7, 14]. Although these thresholds provide significant guidance for experimental studies, their underlying analyses neglect the interdependencies of current density, Faradaic efficiency, cell potential, and conversion on the mechanistic level [12, 17]. This confines the techno-economic analyses to univariate sensitivity analyses, potentially leading to overestimation of the solution space for feasible performance values and electrolyser designs.

Understanding the interdependencies of the performance variables is thus crucial for electrolyser design, operation, and optimisation. Therefore, experimental studies on electrolyser design have mostly been accompanied by modelling efforts, to capture the interdependencies at the channel scale [18–25]. These models are used to resolve local effects in the electrolyser, for example, to understand concentration gradients and mass transfer limitations due to the change in pH near the catalyst layer [18, 20]. While these models can provide relevant insights into the interdependencies of the performance variables they so far have not been translated into techno-economic analyses. Channel models can additionally account for concentration gradients along the flow channel, taking into account their effect on single-pass conversion [26–28]. For example, the study of Kas *et al.* [26] showed an increased loss of CO_2 to carbonate formation at high current densities due to the limited buffer capacities of the electrolyte. This insight reveals a trade–off between current density and conversion, one of the interdependencies commonly neglected when using fixed performance variables for techno-economic analyses.

This study presents a multi–scale modelling approach ranging from the mechanistic channel scale over the electrolyser stack scale to the process scale (Figure 4.1 a)), assessing interdependencies on the electrolyser design level from an economic perspective. For the multi–scale model, a channel model accurate enough to capture interdependencies between the performance metrics of the electrolyser is developed, which then allows to evaluate and demonstrate the influence of the interdependencies on the selected process economic indicator. The channel model is based on a first-principle model of an alkaline flow–through CO_2 electrolyser for the production of ethylene, capturing the interplay between CO_2 conversion, Faradaic efficiency, and cell voltage for varying current densities. This interplay, in turn, influences the electrolyser and downstream unit investment and operating costs. Employing this multi–scale framework for techno-economic assessment and optimisation allows for computing the desired target performance variables based on mechanistic insights.

4.2. MULTI-SCALE MODEL

The multi–scale modelling framework comprises three scales: the process, the electrolyser, and the channel scale, as shown in Figure 4.1 a). While the multi–scale model is generic and independent of the desired product, we will show the model setup and results for ethylene as the main product with a target production rate of 10,000 $\mathrm{kg\,d^{-1}}$. The choice of this gaseous throughput is motivated by the objective to investigate industrially relevant conditions while ensuring that the financial correlations used for the cost estimate remain applicable. The throughput is used to calculate investment and operating costs for the electrolyser and gas separation, herein considered to be a pressure-swing adsorption unit (PSA). The design of the electrolyser is based on a flow-through gas diffusion electrode (GDE) cell, motivated by its extensive application in experimental studies aiming for high current densities [21, 29, 30]. The electrolyser is operated under ambient pressure and room temperature (see Table 4.1). The liquid catholyte flow rate is fixed to evaluate the electrolyser performance, while the liquid post-processing is not considered in the cost evaluation. It is assumed in the model that the electrolyser is continuously fed with fresh electrolyte and all formed ionic species, for example bicarbonate,

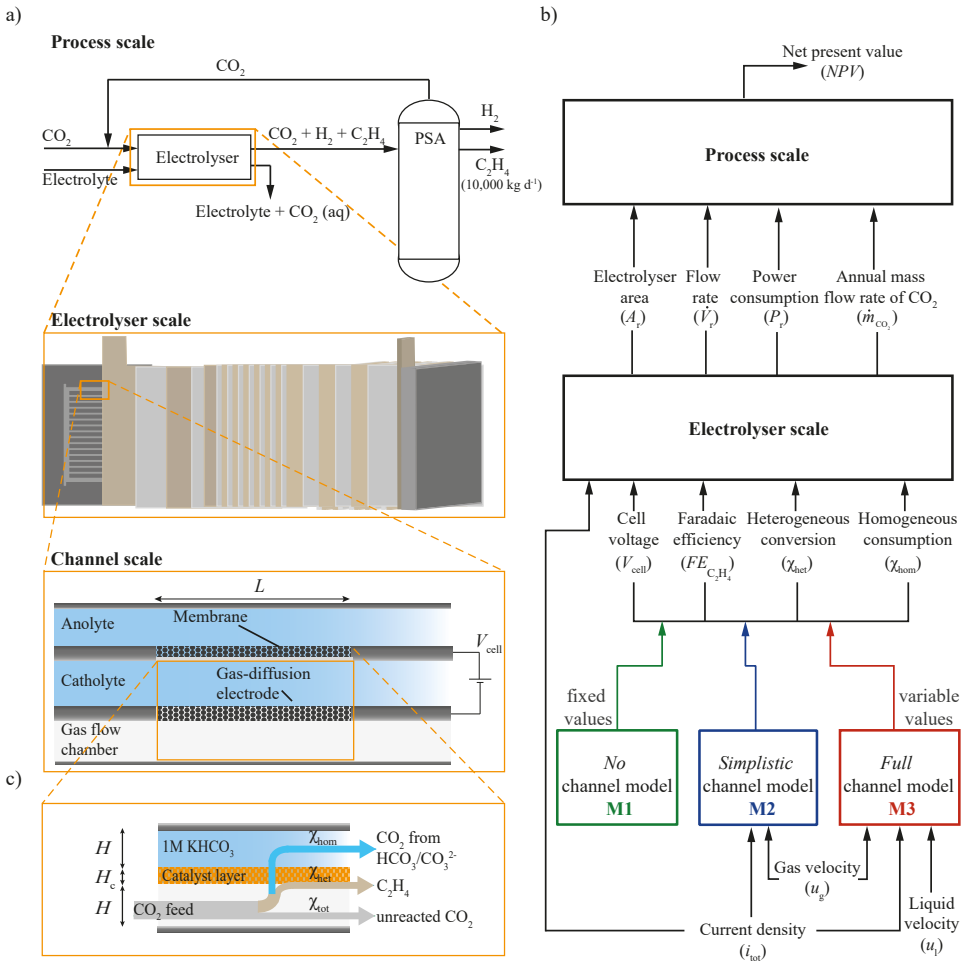

Figure 4.1: Overview of the connection between the process, electrolyser, and channel scale model a) with the relevant in- and output variables and parameters to couple the scales b). The *no* channel model (M1) uses fixed performance variables, while the *simplistic* channel model (M2) and the *full* channel model (M3) capture the different pathways of CO_2 through the electrolyser c) with increasing level of detail.

leave the reactor with the liquid electrolyte stream. The gas phase is solely composed of the reactant CO_2, the target product C_2H_4, and the side product H_2, as shown in the flow chart in Figure 4.1 a).

The electrolyser performance is described based on the following five performance variables (Figure 4.1 b)): the current density i_{tot}, the cell voltage V_{cell}, the Faradaic efficiency $FE_{C_2H_4}$, the heterogeneous conversion χ_{het}, and the homogeneous consumption χ_{hom}. The energy efficiency is not considered separately in this work as it directly follows from the cell voltage and Faradaic efficiency [14]. While the first three are common terms in electrochemistry, the last two are understood as the conversion rates of (i)

CO_2 due to the heterogeneous electrochemical reaction at the catalyst forming the reaction product (often referred to as single pass conversion [30–32]) and (ii) the loss of CO_2 due to the homogeneous carbon equilibrium reactions in the liquid electrolyte, respectively (Figure 4.1 c)). The current state of the art techno-economic assessments rely on a fixed set of these performance variables, which are chosen independently of each other [6, 7, 12, 14]. To illustrate the propagation of the interdependencies across scales we introduce three exemplary models (see Table 4.2) . The *no* channel model (M1) is based on the current state of the art and therefore neglects the interdependencies on the channel scale. For M1, we use a variable current density $i_{\text{tot}} = [50 - 250\,\text{mA}\,\text{cm}^{-2}]$ in combination with fixed electrochemical variables $V_{\text{cell}} = 3.69\,\text{V}$ and $FE_{C_2H_4} = 0.7$, and the fixed conversion rates $\chi_{\text{het}} = 0.5$ and $\chi_{\text{hom}} = 0$. The *simplistic* (M2) and *full* (M3) channel model are governed by the physics at the channel scale with increasing level of detail (Figure 4.2). They, therefore, capture interdependencies between the performance variables as further explained in the following section. All three models are embedded in the same electrolyser and process scale model.

Table 4.1: Overview of channel dimensions and operating parameters.

Parameter	Unit	Value	Description
L	[m]	0.10	Channel length
H	[m]	$1.00 \cdot 10^{-3}$	Channel height
W	[m]	$1.00 \cdot 10^{-2}$	Channel width
H_c	[m]	$3.00 \cdot 10^{-6}$	Catalyst layer thickness
ϵ	[-]	0.70	Porosity
T	[K]	300	Temperature
P	[Pa]	$1.00 \cdot 10^{5}$	Pressure

Table 4.2: Values of performance variables for the *no* (M1), *simplistic* (M2), and *full* (M3) channel model, with a variable current density $i_{\text{tot}} = [50 - 250\,\text{mA}\,\text{cm}^{-2}]$. [1]

Model	V_{cell} [V]	$FE_{C_2H_4}$ [-]	χ_{het} [-]	χ_{hom} [-]
M1	3.69	0.70[29]	0.50[7]	0.00[7]
M2	$f(i_{\text{tot}})$	$f(...)$	$f(...)$	0.13[2]
M3	$f(i_{\text{tot}})$	$f(...)$	$f(...)$	$f(...)$

4.2.1. CHANNEL SCALE MODEL

We consider two-dimensional channel scale models for a GDE-cell, which are most applicable for shallow channels in which the height is much smaller than the width ($W = 10H$ in this work, Table 4.1). The interdependencies between the performance variables i_{tot}, V_{cell}, $FE_{C_2H_4}$, χ_{het}, and χ_{hom} are captured through a mechanistic model of the GDE-cell. The GDE-cell is characterised by a gaseous and a liquid flow channel separated

[1] Performance variables which are depending on more than one other variable are denoted as $f(...)$.

[2] with a fixed additional current density ($i_{\text{hom}} = 50\,\text{mA}\,\text{cm}^{-2}$) and a single channel gas flow rate of 10 sccm, for more details see Section 4.A (appendix).

by a gas diffusion electrode in the cathode compartment. The anode is separated from the cathode side by a proton exchange membrane (Figure 4.1 a), which is not explicitly modelled in this work.

The *simplistic* channel model (M2) solely considers the gas flow channel, with the catalyst layer modelled as an abrupt interface (see Figure 4.2, top). For this the description of the homogeneous consumption (χ_{hom}) is fixed and solely depends on the single channel gas flow rate u_g (see Section 4.A(appendix)). The *full* channel model (M3) considers in addition to the gas flow channel the catalyst and the liquid boundary layer in the electrolyte chamber (see Figure 4.2, bottom). Model M3 hence includes the parasitic homogeneous reactions occurring in the catalyst layer, thereby allowing to fully resolve the homogeneous consumption. The governing equations for M2 and M3 are given in the following sections, together with the relevant assumptions. The chosen channel dimensions and operating parameters are listed in Table 4.1. All other input parameters used in the models M2 and M3 are listed in Section 4.B (appendix). All relevant derivations, boundary conditions, the model validation, and discussion of assumptions for model M3 are given in Section 4.C (appendix).

4

MASS TRANSPORT AND SPECIES BALANCE

We present a model to describe the concentration c_k of species k along the channel length and across the three layers (gas flow channel, catalyst layer, and liquid boundary layer) with the coordinates x and y as defined in Figure 4.2. The *simplistic* channel model M2 and the *full* channel model M3 share the same modelling domain for the gas flow channel. In the gas flow channel pure gaseous CO_2 is introduced and described by plug-flow behaviour. The gaseous mass transport in the porous gas diffusion layer is neglected and the catalyst layer is assumed to be fully flooded. Therefore, the phase transfer of gaseous CO_2 to the liquid electrolyte takes place at the interface of the gas channel and the catalyst layer. The concentration of CO_2 is assumed to be in equilibrium at the gas-liquid interface. The species balance for gaseous compounds (CO_2(g), C_2H_4(g), and H_2(g)) in the gas channel is described by

$$\frac{\partial c_k}{\partial x} = -\frac{\dot{n}_{k,gl}(x)}{u_g H}, \tag{4.1}$$

where u_g is the superficial gas velocity in the gas flow channel and H is the channel height (see Section 4.C.1 (appendix) for derivation). The term $\dot{n}_{k,gl}(x)$ denotes the molar

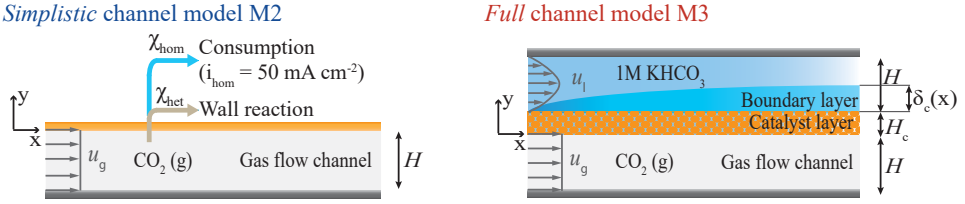

Figure 4.2: The *simplistic* channel model (M2) with an assumed, fixed homogeneous consumption of CO_2 and the *full* channel model (M3) with a fully resolved homogeneous consumption of CO_2.

flux (per unit area) across the gas-catalyst interface. This flux is equal to the molar production or consumption rate of the gaseous compounds over the catalyst layer height H_c at any location x in the single channel

$$\dot{n}_{k,gl}(x) = \int_0^{H_c} \left(\dot{N}_{k,het} + \dot{N}_{k,hom}\right) dy. \tag{4.2}$$

The term $\dot{N}_{k,het}$ denotes the consumption/production rate of CO_2(g), C_2H_4(g), and H_2(g) in $mol\,s^{-1}\,m^{-3}$ due to the heterogeneous electrochemical reactions, while $\dot{N}_{k,hom}$ in Eq. 4.2 denotes the consumption rate of the dissolved CO_2(aq) due to the homogeneous buffer reactions in the liquid electrolyte.

For the *simplistic* channel model (M2) the catalyst layer is not explicitly modelled, with the consumption rate considered as part of the heterogeneous reaction term, adding an additional current density for the homogeneous consumption rate of $i_{hom} = 50\,mA\,cm^{-2}$ (see Section 4.A (appendix)) [12, 27]. By approximating the homogeneous consumption with a fixed additional heterogeneous reaction rate the species balance for dissolved CO_2(aq) and the ionic species does not need to be solved. This approach eliminates $\dot{N}_{k,hom}$ from Eq. 4.2 and therefore allows straightforward calculation of the (single channel gas flow rate dependent) consumption rate (see Section 4.A (appendix)). The concentration of the gaseous compounds CO_2, C_2H_4, and H_2 along the channel length is then fully described by Eqs. 4.1 and 4.2.

For the *full* channel model (M3), the catalyst layer and the liquid boundary layer are fully captured by explicitly solving the species balance for all species (including OH^-, HCO_3^-, and CO_3^{2-} as the ionic species considered in this work) which allows to calculate the homogeneous consumption rate. Similar to previous modelling studies [20, 26] in the following we neglect migration for all ionic species and the cross-over of carbonate and bicarbonate to the anode side [33–35]. The steady state species balance of the dissolved CO_2(aq) and the ionic species in the catalyst layer ($0 \leq y < H_c$) is then governed by diffusion as well as homogeneous and heterogeneous reactions [20]

$$0 = \dot{N}_{k,diff} + \dot{N}_{k,hom} + \dot{N}_{k,het}, \tag{4.3}$$

with the term $\dot{N}_{k,diff}$ accounting for species transport through diffusion. In the catalyst layer, this term is calculated via

$$\dot{N}_{k,diff} = \epsilon^{3/2} D_k \frac{\partial^2 c_k}{\partial y^2}, \tag{4.4}$$

with the diffusion coefficient D_k and the prefactor arising from the porosity ϵ and tortuosity $\tau = \epsilon^{-1/2}$ [36]. Outside the catalyst layer, within the boundary layer ($H_c < y < H_c + \delta_c(x)$), the balance equation of the dissolved CO_2(aq) and the ionic species is only governed by diffusion [26]

$$0 = \dot{N}_{k,diff}, \tag{4.5}$$

with the diffusive transport given as

$$\dot{N}_{k,diff} = D_k \frac{\partial^2 c_k}{\partial y^2}. \tag{4.6}$$

The formation of the diffusive boundary layer on the liquid electrolyte side hinders the transport of fresh electrolyte to the catalyst layer, resulting in an increase in local pH and homogeneous reaction rate in the catalyst layer along the channel length [26]. This effect is included by calculating the thickness of the boundary layer according to the Lévêque approximation [37]

$$\delta_c(x) = 1.022\left(\frac{xHD_{HCO_3^-}}{u_l}\right)^{1/3}, \tag{4.7}$$

with the average liquid electrolyte velocity u_l. The Lévêque approximation entails that two assumptions need to hold for Eq. 4.7 to be a good approximation: *a)* constant concentration at the catalyst-electrolyte interface, and *b)* a developing boundary layer with $\delta_c(x) \ll H$ [38]. Since the supply of HCO_3^- is the limiting factor in retaining the electrolyte buffer capacity in the catalyst layer [26] the length of the boundary layer is equally calculated for all species using the diffusion coefficient $D_{HCO_3^-}$. The concentrations of the ionic species are fixed to the equilibrium concentration in the 1M $KHCO_3$ CO_2 saturated electrolyte at the liquid electrolyte/boundary layer interface and the no flux boundary condition is imposed at the catalyst/gas channel interface. Similarly, the concentration of the dissolved CO_2(aq) is assumed to be in equilibrium with the gaseous CO_2(g) concentration at the catalyst/gas interface and the no flux boundary condition is imposed at the catalyst/boundary layer interface (see Section 4.C.2 (appendix)). This allows the species balance in the catalyst (Eq. 4.3) and boundary layer (Eq. 4.5) to be calculated, which are coupled through Eq. 4.2 to the species balance in the gas channel (Eq. 4.1). The concentration profile in the gas channel, catalyst layer, and liquid boundary layer is thereby fully described, with the calculations of the required heterogeneous production and homogeneous consumption rate given in the following sections.

HETEROGENEOUS REACTIONS

The heterogeneous electrochemical reduction reactions of CO_2(aq) and H_2O(l) take place in the catalyst layer. Copper catalysts form a wide distribution of gaseous and liquid products, which in this work are limited to C_2H_4 and H_2, by considering the following two cathodic reactions:

$$2\,H_2O(l) + 2\,e^- \longrightarrow H_2(g) + 2\,OH^-(aq), \tag{4.8}$$

$$2\,CO_2(aq) + 8\,H_2O(l) + 12\,e^- \longrightarrow C_2H_4(g) + 12\,OH^-(aq). \tag{4.9}$$

Note that this is a simplification in this work, and that, to the best of the authors knowledge, no catalyst for selective ethylene production has been reported. At the anode, the oxygen evolution reaction is facilitated, i.e.

$$4\,OH^-(aq) \longrightarrow O_2(g) + 2\,H_2O(l) + 4\,e^-. \tag{4.10}$$

The electrochemical reaction rate for the species consumed or formed at the electrodes is calculated via Faraday's law [39]

$$\dot{N}_{k,het} = \sum_r \frac{\nu_{k,r} i_k}{z_r F H_c}, \tag{4.11}$$

in which $\nu_{k,r}$ denotes the stoichiometric coefficient for species k in reaction r, z_r the amount of transferred electrons in reaction r, and F the Faraday constant. The current density i_{tot} is calculated via the Tafel equation fitted to experimental data reported by Tan *et al.* [30] (see Section 4.C.3 (appendix))

$$i_{tot} = i_0 \exp\left(-\frac{\alpha_c F}{RT}\eta_c\right), \tag{4.12}$$

with i_0 the exchange current density, α_c the transfer coefficient, R the universal gas constant, and η_c the applied cathode overpotential. In fitting the data for the current density i_{tot}, all reported carbonaceous species are considered to be ethylene, thereby simplifying the kinetic expression. It is further assumed that hydrogen is only produced at the onset of mass transport limitations towards CO_2 [40, 41], which ensures that the current density i_{tot} remains constant over the electrode length (galvanostatically controlled) leading to the following partial current densities of C_2H_4 and H_2:

$$i_{C_2H_4}(x,y) = i_{tot}\frac{c_{CO_2}(x,y)(aq)}{c^{ref}_{CO_2}(aq)}, \tag{4.13}$$

$$i_{H_2}(x,y) = i_{tot} - i_{C_2H_4}(x,y), \tag{4.14}$$

with $c^{ref}_{CO_2}(aq)$ the CO_2 equilibrium concentration within the electrolyte at standard conditions ($P = 1.00 \cdot 10^5$ Pa and $T = 300$ K). The dissolved $CO_2(aq)$ concentration in the liquid electrolyte ($c_{CO_2}(x,y)(aq)$) relates to the gaseous CO_2 concentration along the channel length c_{CO_2} through Henry's law. The changes in the $CO_2(aq)$ concentration over the catalyst layer height is driven by the heterogeneous consumption (Eq. 4.11) and homogeneous conversion (Eq. 4.17). The motivation and limits of these simplified kinetics are discussed in Section 4.C.4 (appendix).

HOMOGENEOUS REACTIONS

In addition to the heterogeneous reaction, CO_2 is also consumed by the homogeneous reactions within the electrolyte in the catalyst layer. These reactions are constituted by the bicarbonate-buffer reactions, balancing the pH of the solution. This reaction mechanism is only considered in model M3 and described by the following equilibrium reactions [20]

$$CO_2(aq) + OH^-(aq) \underset{-\,k_{r1}}{\overset{+\,k_{f1}}{\rightleftharpoons}} HCO_3^-(aq), \tag{4.15}$$

$$HCO_3^-(aq) + OH^-(aq) \underset{-\,k_{r2}}{\overset{+\,k_{f2}}{\rightleftharpoons}} CO_3^{2-}(aq) + H_2O(l), \tag{4.16}$$

where k_{f1} and k_{f2} are the forward reaction rate constants, and k_{r1} and k_{r2} the respective reverse reaction rate constants, the values to all of which are provided in Table 4.7. Under consideration of the above equilibrium reactions, the volumetric homogeneous reaction

terms can be written as [18]

$$\begin{aligned}
\dot{N}_{CO_2(aq),hom} &= -k_{f1}[CO_2][OH^-] + k_{r1}[HCO_3^-] \\
\dot{N}_{OH^-(aq),hom} &= -k_{f1}[CO_2][OH^-] + k_{r1}[HCO_3^-] \\
&\quad - k_{f2}[HCO_3^-][OH^-] + k_{r2}[CO_3^{2-}] \\
\dot{N}_{HCO_3^-(aq),hom} &= k_{f1}[CO_2][OH^-] - k_{r1}[HCO_3^-] \\
&\quad - k_{f2}[HCO_3^-][OH^-] + k_{r2}[CO_3^{2-}] \\
\dot{N}_{CO_3^{2-}(aq),hom} &= k_{f2}[HCO_3^-][OH^-] - k_{r2}[CO_3^{2-}],
\end{aligned} \tag{4.17}$$

with the notation [c] used for the concentration c_k. The significance of the homogeneous reactions can be explained by the increased rate of Eq. 4.15 at higher alkalinity, which inevitably occurs at elevated heterogeneous reaction rates due to increased hydroxide production. For simplicity, it is assumed that the homogeneous reactions occur solely within the catalyst layer, where pH and CO_2(aq) concentration are highest. The void fraction within the catalyst layer is not accounted for.

4.2.2. ELECTROLYSER SCALE MODEL

The electrolyser scale model couples the calculated concentration profiles from the channel scale model to the process scale model (Figure 4.1 b)). Firstly, the input variables χ_{het}, χ_{hom}, $FE_{C_2H_4}$, and V_{cell} are calculated based on the CO_2(g) and C_2H_4(g) concentrations obtained from the channel scale models M2 and M3 for a variable i_{tot}. For this, the electrolyser is assumed to be composed of a number of hydraulically, thermally, and electrically independent channels. The overall conversion achieved in the electrolyser then equals the single-channel conversion, which is calculated assuming a constant pressure as

$$\chi_{tot} = \frac{c_{CO_2}(x=0) - c_{CO_2}(x=L)}{c_{CO_2}(x=0)}, \tag{4.18}$$

with the channel length L. The heterogeneous conversion is calculated as [30–32]

$$\chi_{het} = \frac{2c_{C_2H_4}(x=L)}{c_{CO_2}(x=0)}, \tag{4.19}$$

with 2 being the stoichiometric coefficient (see Eq. 4.9). The homogeneous consumption is then calculated as the difference between those figures, i.e.

$$\chi_{hom} = \chi_{tot} - \chi_{het}. \tag{4.20}$$

The Faradaic efficiency (selectivity) towards ethylene is calculated based on the product concentration and gas velocity u_g at the channel outlet [33] (see Section 4.D (appendix))

$$FE_{C_2H_4} = \frac{c_{C_2H_4}(x=L)12u_gFH}{i_{tot}L}, \tag{4.21}$$

with 12 being the amount of electrons required to reduce CO_2 to C_2H_4. The cell voltage is further related to the current density (see Eq. 4.12) via

$$V_{\text{cell}} = E_{\text{a}}^0 + \eta_{\text{a}}(i_{\text{tot}}) + \left|E_{\text{c}}^0\right| + \left|\eta_{\text{c}}\right|(i_{\text{tot}}) + \eta_{\Omega}(i_{\text{tot}}), \tag{4.22}$$

with the constant anodic and cathodic standard potentials $E_{\text{a,c}}^0$ and the current density dependent overpotentials $\eta_{\text{a,c,}\Omega}$ (see Section 4.E (appendix) for more details). The input variables for the electrolyser scale for models M2 and M3 (Table 4.2) are then fully described by Eqs. 4.18 - 4.22.

Based on these input variables, the required electrolyser area A_{r}, the volumetric gas flow rate $\dot{V}_{\text{r}}$, the annual mass flow rate $\dot{m}_{\text{CO}_2}$, and the power consumption P_{r} are calculated next (see Section 4.D (appendix) for derivations), to estimate the investment and operating costs for the electrolyser and separation unit. The required electrolyser area is calculated taking into account the Faradaic efficiency as well as the current density

$$A_{\text{r}} = \frac{\dot{F}_{\text{C}_2\text{H}_4,\text{target}}\, 12F}{i_{\text{tot}} F E_{\text{C}_2\text{H}_4}}, \tag{4.23}$$

with the daily production target 10,000 kg d^{-1} converted to $\dot{F}_{\text{C}_2\text{H}_4,\text{target}} \approx 4.13\ \text{mol}\,\text{s}^{-1}$. Further, the volumetric flow rate associated with the electrolyser setup is calculated from the heterogeneous conversion and target production rate as

$$\dot{V}_{\text{r}} = \frac{2\dot{F}_{\text{C}_2\text{H}_4,\text{target}}}{\chi_{\text{het}} c_{\text{CO}_2}(x=0)}. \tag{4.24}$$

The annual mass flow rate of CO_2 through the electrolyser then follows from the annual production target ($\dot{m}_{\text{C}_2\text{H}_4,\text{target}} = 3{,}500{,}000\ \text{kg}\,\text{yr}^{-1}$). The corresponding annual consumption rate of CO_2 equals

$$\dot{m}_{\text{CO}_2} = \left(1 + \frac{\chi_{\text{hom}}}{\chi_{\text{het}}}\right) 2\frac{44}{28}\dot{m}_{\text{C}_2\text{H}_4,\text{target}}. \tag{4.25}$$

Finally, the overall power consumption P_{r} follows from the product of the cell voltage and current density, i.e.

$$P_{\text{r}} = V_{\text{cell}}\, i_{\text{tot}} A_{\text{r}}. \tag{4.26}$$

4.2.3. PROCESS SCALE MODEL

The process scale model describes the overall process and its economic performance. This model represents a simplified plant layout based on previous techno-economic analyses [7, 14], with a CO_2 feed source through direct air capture (DAC), an electrolyser unit for the electrochemical CO_2–reduction, and subsequent gas separation in a pressure swing adsorption (PSA) unit (Figure 4.1 a)). Liquid pre– and post–processing steps are not taken into account. The currency used is US dollar (multiple years).

The selected process economic indicator is the end-of-lifetime net present value (NPV) of the overall process, assuming 20 years of continuous operation [7]. The NPV

is calculated by taking into account the cash flow $CF(t)$ on an annual basis as

$$NPV = \sum_{t=1}^{20} \frac{CF(t)}{(1+IR)^t}, \tag{4.27}$$

in which t is the respective year of operation. The term IR denotes the interest rate and is assumed to be 10% throughout the lifetime [7]. It is assumed that the plant is erected within the first year and operates at full capacity for the remaining 19 years of operation with the cash flow calculated as

$$CF(t) = \begin{cases} TCI, & \text{for } t = 0, \\ C_{\text{rev}} - C_{\text{op}} - C_{\text{m}}, & \text{for } t \geq 1, \end{cases} \tag{4.28}$$

where C_{rev}, C_{op}, and C_{m} describe the annual revenue, operating costs, and maintenance costs, respectively. TCI is the total capital investment, which comprises the costs for the electrolyser, the separation unit, and all additional infrastructural facilities (balance of plant). The investment costs for the electrolyser are proportional to the required electrolyser area ($\$920\,\text{m}^{-2}$) [7], while the costs for the PSA unit scale with the overall volumetric flow rate at the electrolyser outlet with a reference cost [42] of 1.99 M$ and a reference flow rate of $1000\,\text{m}^3\,\text{h}^{-1}$. The balance of plant costs are assumed to make up 35/65 of the electrolyser costs [7]. The total capital investment based on the equipment costs can then be calculated as

$$TCI = (\$920\,\text{m}^{-2} A_r)(1+35/65) + \$1.99 \cdot 10^6 \left(\dot{V}_{\text{r}} \frac{3600\,\text{s}\,\text{h}^{-1}}{1000\,\text{m}^3\,\text{h}^{-1}} \right)^{\beta}, \tag{4.29}$$

where A_{r} is the required area (Eq. 4.23) and $\dot{V}_{\text{r}}$ the volumetric flow rate at the electrolyser outlet (Eq. 4.24). The term β is a fitting factor associated with the cost correlation for the PSA unit, assumed to be 0.7 according to the regression function proposed by Paturska *et al.* [42] for flow rates between $500\,\text{m}^3\,\text{h}^{-1}$ and $1400\,\text{m}^3\,\text{h}^{-1}$.

The annual revenue depends on the annual production target, and market price of ethylene (herein taken as $\$1.3\,\text{kg}^{-1}$)[7] as

$$C_{\text{rev}} = \$1.3\,\text{kg}^{-1}\, \dot{m}_{\text{C}_2\text{H}_4,\text{target}}. \tag{4.30}$$

The annual costs are then determined by the CO_2 price (herein taken as $\$0.04\,\text{kg}^{-1}$) [14], which is slightly lower than the most optimistic assumption for commercial DAC units using chemical absorption [43]. For the electricity price, an optimistic value of $\$0.03\,\text{kWh}^{-1}$ is taken based on predictions published by Haegel *et al.* [44]. The operating costs associated to separation are assumed to be only made up of the electricity costs ($0.25\,\text{kWh}\,\text{m}^{-3}$) [42], which allows calculating the overall operating costs based on the annual consumption rate of CO_2 (Eq. 4.25), the overall power consumption (Eq. 4.26) and the volumetric flow rate (Eq. 4.24) as

$$\begin{aligned} C_{\text{op}} = {} & \$0.04\,\text{kg}^{-1}\, \dot{m}_{\text{CO}_2} + \$0.03\,\text{kWh}^{-1} \\ & \times (8400\,\text{h}\,\text{yr}^{-1} P_{\text{r}} + 0.25\,\text{kWh}\,\text{m}^{-3} \\ & \times 30.24 \cdot 10^6\,\text{s}\,\text{yr}^{-1}\, \dot{V}_{\text{r}}). \end{aligned} \tag{4.31}$$

The annual maintenance costs are taken to be 2.5% of the capital investment costs for the electrolyser [7], i.e.

$$C_{\mathrm{m}} = 0.025 \cdot \$920\,\mathrm{m}^{-2} A_r. \tag{4.32}$$

As a comparative figure for the models (M1 to M3) the *relative NPV* is defined as follows

$$NPV_{\mathrm{rel,Mx}} = \begin{cases} \dfrac{NPV_{\mathrm{Mx}}}{\max(NPV_{\mathrm{M1}})} & \text{for } 0 < NPV_{\mathrm{Mx}} \\ \dfrac{\max(NPV_{\mathrm{M1}})}{NPV_{\mathrm{Mx}}} & \text{for } NPV_{\mathrm{Mx}} <= 0, \end{cases} \tag{4.33}$$

for any model $\mathrm{M_x}$ with x $\in [1,2,3]$ (for further detail, see Section 4.F.1 (appendix)). The highest NPV of model M1 is taken as a reference point, as at this value the investment costs for the electrolyser do not influence the overall NPV anymore and the resulting current density is commonly reported as the target value in techno-economic analyses [6, 7, 14].

4.2.4. IMPLEMENTATION

For the *no* channel model M1 the input variables to the electrolyser scale are fixed (Table 4.2) such that the required electrolyser area, the volumetric gas flow rate, the annual mass flow rate of CO_2, and the overall power input required to achieve the target production for C_2H_4 (Eqs. 4.23 - 4.26) can be straightforwardly calculated. The *relative NPV* (Eq. 4.33) is then calculated based on these variables as a comparison metric. For the *simplistic* channel model (M2) and the *full* channel model (M3), the input variables to the electrolyser scale depend on the output of the channel scale. Therefore, the concentration of CO_2, C_2H_4, and H_2 along the channel length needs to be calculated first. The concentrations are then used to calculate the input variables to the electrolyser scale (Eqs. 4.18 - 4.22) and subsequently the input variables to the process scale are calculated (Eqs. 4.23 - 4.26), followed by the NPV and *relative NPV*.

The species balance (Eq. 4.1) in the gas channel is solved for model M2 and M3 via Heun's method for varying current densities (i_{tot}) and gas velocities (u_{g}). For the *simplistic* model (M2) the flux across the gas-catalyst interface (Eq. 4.2) is given as a boundary condition, while for the *full* channel model (M3) the flux across the gas-catalyst interface is updated at every finite difference by solving the governing equations in the catalyst and boundary layer (Eq. 4.3 & 4.5). The solution to these respective domains is found with the `Matlab` R2020a built-in solver `bvp4c`, where the extent of the boundary layer is adapted on each step according to Eq. 4.7 and the solution of the previous step supplied as an initial guess to the current step. The extend of the boundary layer is calculated for a fixed electrolyte flow rate of $0.54\,\mathrm{m\,s^{-1}}$ to minimise the consumption of CO_2 due to the buffer reaction [26], while still ensuring operation in the laminar flow regime. To gain insight into the optimal mode of operation, the model has been constructed to allow for facile use with the `Matlab` built-in non-linear optimiser `fmincon` and `fminsearch`.[3]

[3]The full multi–scale model is available via `https://github.com/IsabellBagemihl/Multi-scaleModelElectrochemicalCO2Reduction.git`

4.3. RESULTS AND DISCUSSION

In this section we first discuss the interdependencies between three performance variables on the channel scale for the *no* channel (M1), the *simplistic* channel (M2), and the *full* channel (M3) model. For this, we consider the heterogeneous conversion χ_{het}, the homogeneous consumption χ_{hom}, and the Faradaic efficiency $FE_{C_2H_4}$ and their dependency on the current density. As the cell voltage V_{cell} can be straightforwardly calculated (Eq. 4.22) it is not explicitly discussed. Secondly, we discuss the propagation of the interdependencies from the channel scale to the process scale model in terms of the *relative NPV* for varying current densities and gas velocities. The contribution of selected technical input variables to the process *NPV*, together with the contribution of economic parameters, are evaluated in a sensitivity analysis in Section 4.F.2 (appendix). Lastly, the optimisation results are presented and discussed in light of current developments in the literature.

4

4.3.1. INTERDEPENDENCY OF PERFORMANCE VARIABLES ON THE CHANNEL SCALE

The heterogeneous conversion (χ_{het}), homogeneous consumption (χ_{hom}), and selectivity ($FE_{C_2H_4}$) with varying current densities (i_{tot}) are presented for models M1 to M3 in Figure 4.3. Contrary to the case of fixed performance variables (M1), using a mechanistic channel scale model results in a dependency of the above-stated variables predicting the expected trend of increased conversion rates with higher current densities as shown in Figure 4.3 a). For low conversions, this trend is linear as the supply of CO_2 to the catalyst is not limited (for more details, see Section 4.G (appendix)). For the *simplistic* channel model M2, the limit of the linear scaling is reached at higher conversions than for the *full* channel model (M3). This can be explained by comparing the trends for the consumption rate of CO_2 for model M2 and M3 in Figure 4.3 b). While the consumption rate is constant in model M2 the consumption of CO_2 in M3 increases with increasing

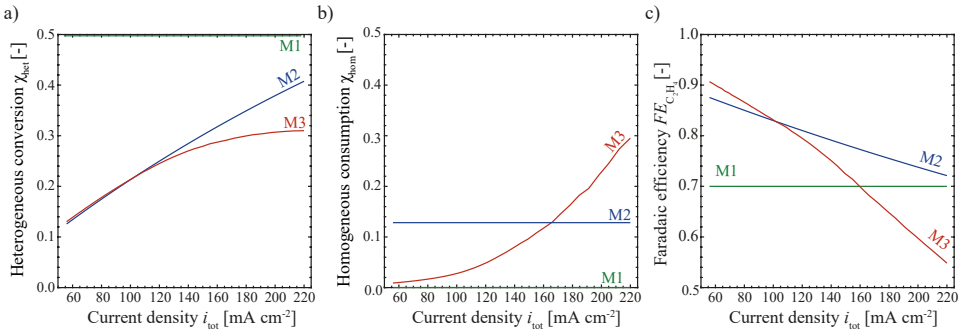

Figure 4.3: Heterogeneous conversion a), homogeneous consumption b) and Faradaic efficiency c) for models M1 to M3 as a function of current density, with a fixed channel geometry (Table 4.1) and a single channel gas flow rate of 10 sccm (u_g = 0.0167 m s^{-1}). For model M2 a fixed additional current density (i_{hom} = 50 mA cm^{-2}) is used to account for the homogeneous reactions, while these are fully resolved in model M3 for a fixed single channel liquid flow rate of 325 mL min^{-1} (u_l = 0.54 m s^{-1}).

the current densities. Increased consumption rates of CO_2 limit the availability of CO_2 at the catalyst site and therefore limit the heterogeneous conversion therefore leading to a deviation from the linear scaling at lower current densities for M3 compared to M2. The steep exponential increase in homogeneous consumption for model M3 can be explained by the dependency of the formation of hydroxide ions on the current density, as seen in Eq. 4.8 and 4.9, paired with the limited buffer capacity of the electrolyte. This eventually leads to higher consumption rates through the homogeneous reaction than through the heterogeneous reaction at high current densities. This, in turn, influences the selectivity, resulting in a steep decrease of $FE_{C_2H_4}$ towards the formation of ethylene with increased current density for M3 as shown in Figure 4.3 c). For a constant consumption rate in M2 the Faradaic efficiency towards ethylene displays a weaker dependency on the current density because the main driver for the depletion of CO_2 at high current densities is the increased heterogeneous conversion instead of the homogeneous consumption.

4.3.2. PROPAGATION OF INTERDEPENDENCIES FROM THE CHANNEL SCALE TO THE PROCESS SCALE MODEL

Having established how the level of detail at the channel scale influences the input for the electrolyser scale (in the form of χ_{het}, χ_{hom}, $FE_{C_2H_4}$, and V_{Cell} for a given i_{tot}, u_g, and i_{hom} (M2) or u_l (M3)), the propagation of the level of detail to the process scale is shown in terms of the *relative NPV* in Figure 4.4. The *relative NPV* (Eq. 4.33) compares the NPV (Eq. 4.27) for each model to the maximum NPV reached with model M1 ($NPV \approx 24$ M\$ at $i_{tot} \approx 600\,mA\,cm^{-2}$). The calculations for the maximum NPV of model M1 can be found in Section 4.F.1 (appendix) with a discussion on the negative NPV in Section 4.H (appendix). Therefore, a decrease or increase of the $NPV_{rel,Mx}$ indicates the same relative change in the NPV, hence both terms will be used interchangeably in the following. In Figure 4.4 a) and b) the green lines depicts the $NPV_{rel,M1}$ calculated with the *no* channel model (M1), with the current density being the only variable input parameter to the electrolyser scale (see Table 4.2 and Figure 4.1). As described in previous literature [7], the current density in M1 solely influences the electrolyser area (Eq. 4.23) and therefore the investment costs leading to the expected trend of a steady increase in the NPV with an increase in current density as shown in Figure 4.4 a), eventually reaching the asymptotic value of 1. Contrary to model M1 an increase in current density leads to a decrease in the NPV for high current densities (see Section 4.F.2 (appendix)), for both mechanistic models (M2 and M3) resulting in a clear optimum within the range of variation of the current density. A similar trend is observed when fixing the current density while varying the single channel gas flow rate as shown in Figure 4.4 b). While the single channel gas flow rate shows no effect on the NPV in model M1 as the input variables are fixed, both mechanistic models display again a clear optimum. The significance of the single channel gas flow rate on the NPV was also observed in the sensitivity analysis in Section 4.F.2 (appendix). This analysis reveals that the interdependencies of the input variables translate to important trade-offs on the process scale, which cannot be captured with fixed variable models like model M1.

The maxima in the NPV for the channel models M2 and M3 are explained through the interdependence of mass transfer limitation, heterogeneous conversion, and homo-

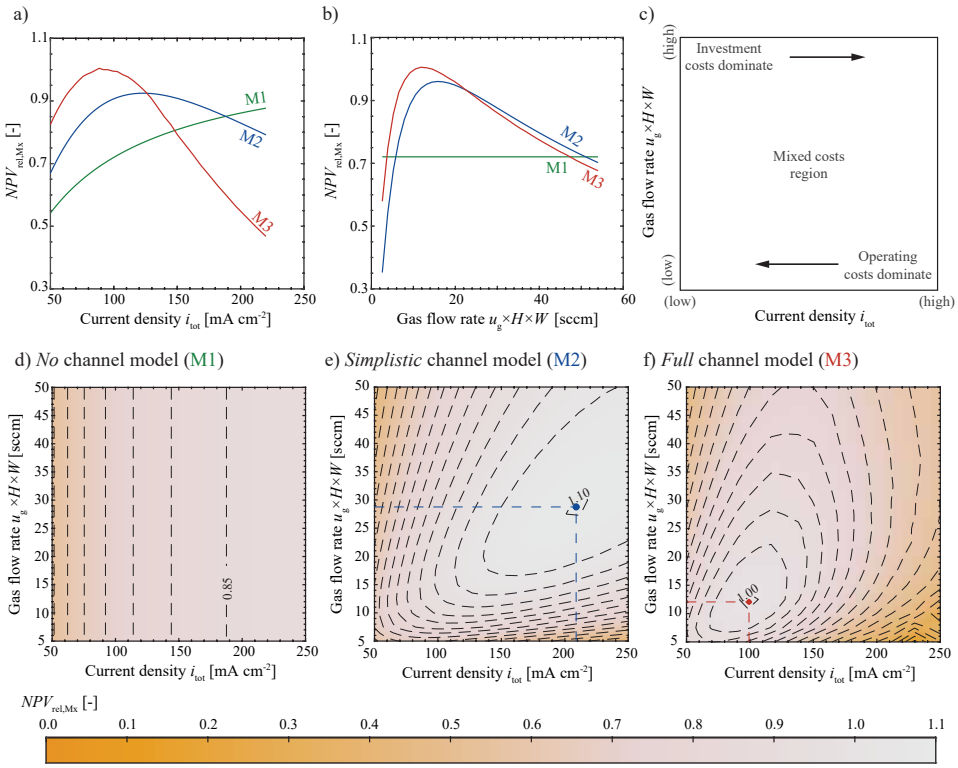

Figure 4.4: *Relative NPV* as a function of current density for a fixed single channel gas flow rate $u_g \times H \times W = 10$ sccm a) and as a function of the single channel gas flow rate for a fixed current density $i_{tot} = 100$ mA cm^{-2} b). Schematic of main cost drivers for varying current densities and single channel gas flow rates with the arrows indicating the direction of decrease of the respective cost unit c). Contours (with an equidistant spacing of 0.05) of the *relative NPV* for varying current densities and single channel gas flow rates for M1 d), M2 e), and M3 f), with the dots indicating the optimum for model M2 and M3. For model M2 a fixed additional current density ($i_{hom} = 50$ mA cm^{-2}) is used to account for the homogeneous reactions, while these are fully resolved in model M3 for a fixed single channel liquid flow rate of 325 mL min^{-1} ($u_l = 0.54$ m s^{-1}).

geneous consumption. Figure 4.4 c) shows this trade-off schematically in terms of investment and operating costs linked to the current density and single channel gas flow rate. From the previous section we learned that low current densities retain low heterogeneous conversion rates and high selectivities. Further the high CO_2 concentrations in the catalyst layer cause the mass transfer related overpotential (Eq. 4.13), and hence the overall cell potential (Eq. 4.22), to decrease. A low cell potential reduces the required power input, translating to lower operating costs for the electrolyser. However, due to the low conversion, larger electrode areas and separation units are required to maintain a specific throughput, which increases the investment costs. High current densities on the other hand increase the heterogeneous conversions rate and therefore reduce investment costs, but also lead to an unwanted expense of electrons through the increased reduction of water in the hydrogen evolution reaction (Eq. 4.8), therefore in-

creasing the operating costs. The trade-off between investment and operating costs is similarly observed for varying single channel gas flow rates. High single channel gas flow rates reduce the residence time in the channel and consequently reduce the heterogeneous conversion rate leading to an increased daily gas throughput to achieve the target production rate of ethylene. This in turn requires a larger separation unit increasing the investment costs. Low single channel gas flow rates, on the other hand, increase the heterogeneous conversion, lowering the daily gas throughput. However lead to a depletion of CO_2 along the channel which results in an increase towards the hydrogen evolution reaction. This in turn increases the operating costs of the electrolyser as electricity is now lost towards the parasitic side reaction.

The insights on the trade-offs explain the difference in the impact of current density and gas flow rate on the costs. The single channel gas flow rate mainly influences the heterogeneous conversion rates through the residence time in the channel and consequently, the investment costs of the gas separation unit and the operating costs of the electrolyser. The current density however influences both, the investment and operating costs of the electrolyser, as well as for the separation unit.

Mapping the *relative NPV* for all three models (M1-M3) over the space of varying current densities and single channel gas flow rates allows us to compare how the optimal operating areas vary with the level of mechanistic detail in the model. Figure 4.4 d) to f) show that for all models low current densities and high single channel gas flow rates are not optimal based on the high investment costs. However, only models M2 and M3 additionally show a higher loss region for high current densities and low single channel gas flow rates. The *no* channel model (M1) does not display this trade-off due to a fixed conversion rate (see Table 4.2) leading to fixed operating costs. Therefore, a clear optimum for the operating conditions is found for the models considering the interdependencies between the performance variables (indicated by the dots in Figure 4.4 e) and f)).

4.3.3. OPTIMISATION RESULTS

The pronounced impact of the current density and single channel gas flow rate on the *NPV* has been discussed in the previous section. It was further shown that considering the interdependencies (model M2 and M3) between the performance variables leads to a trade-off between investment and operating costs which manifests in a clear optimum for the operating conditions. The optimisation results are summarised in Table 4.3. Note that the optimal results for M1 are not shown as the conversion rate is fixed, and the optimal current density always lies at the upper constraint, i.e. at $250\,mA\,cm^{-2}$. Figure 4.5 compares the optimisation results with literature based operating targets. It can be seen that the optimal current density for M2 lies close to the values suggested as minimal-threshold in non-mechanistic techno-economic analysis (above $200\,mA\,cm^{-2}$), while this value is considerably lower when modelling the consumption of CO_2 as a function of the process conditions (M3). Here, the optimal current density lies at $\approx 100\,mA\,cm^{-2}$, roughly half the value that is found for M2 and lower than the threshold values proposed in the literature [6, 7, 14]. This is driven mainly by the prediction of a

[4] For model M3 the obtained optimal values show a dependency on the initial guess with a deviation of less than 5%.

Table 4.3: Overview of the optima for model M2 and M3 as shown in Figure 4.4 e) and f).

Variable	Unit	M2	M3[4]
Input			
i_{tot}	[mA cm^{-2}]	209	99.2
u_g	[m s^{-1}]	0.05	0.02
Channel scale			
V_{cell}	[V]	3.80	3.47
$FE_{C_2H_4}$	[-]	0.89	0.85
χ_{het}	[-]	0.17	0.18
χ_{hom}	[-]	0.04	0.02
Electrolyser scale			
$\dot{V}_r$	[m^3 s^{-1}]	1.23	1.14
A_r	[m^2]	$2.57 \cdot 10^3$	$5.67 \cdot 10^3$
P_r	[MW]	20.4	19.5
$\dot{m}_{CO_2}$	[kg yr^{-1}]	$1.40 \cdot 10^3$	$1.25 \cdot 10^3$
Process scale			
NPV	[M$]	-22.0	-24.0

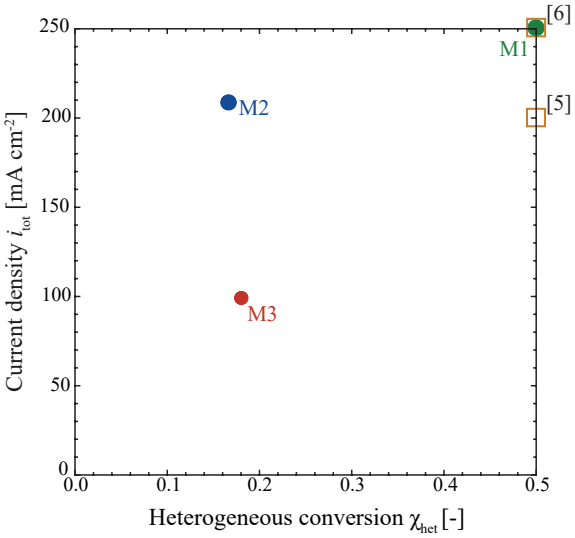

Figure 4.5: Optimal operation points for M1, M2, and M3 (circles) in terms of current density and heterogeneous conversion based on the optimal single channel gas flow rate as presented in Figure 4.4 e) and f). For M1 this point is found at the boundary of its domain (χ_{het} = 0.5). The target values based on literature [6, 7] are denoted as squares.

strong increase in unwanted homogeneous consumption at high current densities, rendering the operation at lower current densities desirable. The observed product distribution for the formation of higher hydrocarbons and the reported increase in selectivity with increasing current density is neglected in this work. As the kinetic expressions (Eqs. 4.11 - 4.14) and the assumptions regarding the separation unit are the same in models M2 and M3, the trade-off for the heterogenous conversion is the same in both models. Hence, the optimiser converges to a single channel gas flow rate which facilitates a similar conversion rate for both models of slightly below 20%. This comparably low conversion is subject to how the kinetics are formulated in this work, leading to a strictly inverse relationship between the conversion and the Faradaic efficiency. Besides the simplification of the kinetics on the findings, other important assumptions are taken. In the remainder of the paper, we discuss their foreseen impact on our findings.

4.3.4. LIMITATIONS OF RESULTS

The presented channel scale model is more advanced than the majority of CO2R models reported previously, yet several phenomena are not included such as liquid product formation and their migration to and oxidation at the anode, migration of bicarbonate/carbonate ions, and hence degassing of CO_2 at the anode side. While we provide a detailed discussion on the influence of these phenomena on our findings in Section 4.I (appendix), we here highlight the influence of migration and degassing of CO_2. In anion exchange membrane electrolysers for example a significant amount of CO_2 crosses over to the anode side in form of carbonate ions as the main charge carrying species under steady-state conditions [33]. This increases the consumption rate of CO_2 compared to the predictions of model M3 [35], leading to lower optimal CO_2 conversions. In bipolar membrane electrolysers this effect can be minimized at the cost of increasing the ohmic resistance and hence required cell potential [34], decreasing the overall *NPV* (see Section 4.H (appendix). Further, we assume the investment and operating costs of the separation unit (PSA) to only depend on the overall required single channel gas flow rate and not on the composition of the gas stream itself. Additionally, the liquid products and potential cleaning steps of the electrolytes are not considered. Conceivably, including detailed models of the required post treatment units leads to higher investment costs and optimal CO_2 conversion rates.

Considering the various assumptions underlying these results the authors would like to stress that the herein reported optimal values shall not be understood as newly proposed target values for the performance variables. Rather, they shall showcase how combining mechanistic and techno-economic models allows for design optimisations in the field of CO_2 electrolysis. More importantly, they show how the level of mechanistic detail in such models strongly influences the resulting recommendations. In this sense, the distance between the optimum points for the models M1, M2, and M3 in Figure 4.5 can be understood as resulting from different levels of mechanistic understanding, while the distance between the optimum points and the literature recommendations results from a discrepancy between required, and currently possible electrolyser performances.

4.4. CONCLUSION AND OUTLOOK

Target values for performance variables for the low-temperature electrochemical conversion of CO_2 have so far been derived from techno–economic analysis based on the assumption that the performance variables such as current density and Faradaic efficiency are independent. In this work, we present a multi–scale framework that incorporates mechanistic models of a GDE–based CO_2 electrolyser to capture the interdependence between the performance variables required as input to the electrolyser scale: heterogeneous conversion, homogeneous consumption, Faradaic efficiency, and cell voltage. This framework is used to perform a techno–economic assesment and optimisation for a CO_2–electrolysis–based process, revealing optimal target values for the performance variables that can strongly deviate from previously reported targets. For the herein chosen electrolyser design this manifests in an optimal current density of around half of commonly reported values. While it should be noted that the optima in this work are derived based on simplified reaction mechanisms and design considerations and therefore should not be taken as fixed optimum values for future electrolyser designs, the used approach nonetheless highlights the dependency of the mechanistic detail and interdependencies between performance variables on the economic viability of an electrolyser design. This work further presents a tool to evaluate electrolyser design choices based on an economic objective, which in its generic form can be applied to various electrolyser designs [19, 45–48] and CO_2–reduction products such as CO or formate [20, 26, 49]. For different electrolyser designs and products, the modelling assumptions, and hence, the economic predictions, are highly dependent on the available data, therefore it is important to *a)* move towards more holistic, multi–scale modelling approaches in the field of CO_2 electrolysis, and to *b)* communicate measured or targeted electrolyser performance with all applicable boundary conditions, including achieved conversions.

Table 4.4: List of symbols.

Symbol	Description	Unit
Roman		
A_r	Required electrolyser area	m^2
$c^{ref}_{\mathrm{CO_2}}(aq)$	Reference concentration	$\mathrm{mol\,m^{-3}}$
c_k	Concentration of species k	$\mathrm{mol\,m^{-3}}$
C_m	Annual maintenance costs	$\mathrm{\$\,yr^{-1}}$
C_op	Annual operational costs	$\mathrm{\$\,yr^{-1}}$
C_rev	Annual revenue	$\mathrm{\$\,yr^{-1}}$
CF	Cash flow	$\mathrm{\$\,yr^{-1}}$
D_k	Diffusion coefficient of species k	$\mathrm{m^2\,s^{-1}}$
E^0_r	Standard potential of the reaction r	V
E_r	Applied potential vs RHE of the reaction r	V
$\dot{F}_{\mathrm{C_2H_4,target}}$	Molar flow rate of targeted C_2H_4 production	$\mathrm{mol\,s^{-1}}$
F	Faraday constant	$\mathrm{A\,s\,mol^{-1}}$
$FE_{\mathrm{C_2H_4}}$	Faradaic efficiency towards ethylene	-
H	Channel height	m
H_c	Catalyst layer thickness	m
H_m	Membrane layer thickness	m
$H_{\mathrm{CO_2,elec.}}$	Henry constant CO_2	-
i_hom	Additional current density for homogeneous consumption	$\mathrm{A\,m^{-2}}$
$i_{0,\mathrm{k}}$	Exchange current density of species k	$\mathrm{A\,m^{-2}}$
i_k	Partial current density of species k	$\mathrm{A\,m^{-2}}$
i_tot	Current density (sum of partial current densities)	$\mathrm{A\,m^{-2}}$
IR	Interest rate	-
k_f	Forward reaction rate constant	$\mathrm{m^3\,mol^{-1}\,s^{-1}}$
k_r	Reverse reaction rate constant	$\mathrm{s^{-1}}$
L	Channel length	m
M_k	Molar mass of species k	$\mathrm{kg\,mol^{-1}}$
$\dot{m}_\mathrm{k}$	Annual mass flow rate of species k	$\mathrm{kg\,yr^{-1}}$
$\dot{n}_{\mathrm{k,gl}}$	Molar flux across the gas-catalyst interface	$\mathrm{mol\,m^{-2}\,s^{-1}}$
$\dot{N}_{\mathrm{k,diff}}$	Diffusive species transport	$\mathrm{mol\,m^{-3}\,s^{-1}}$
$\dot{N}_{\mathrm{k,het}}$	Electrochemical production rate	$\mathrm{mol\,m^{-3}\,s^{-1}}$
$\dot{N}_{\mathrm{k,hom}}$	Homogeneous consumption rate	$\mathrm{mol\,m^{-3}\,s^{-1}}$
NPV	Net present value	\$
P	Pressure	Pa
P_r	Overall power consumption	W
R	Universal gas constant	$\mathrm{J\,mol^{-1}\,K^{-1}}$
t	Time	s
T	Temperature	K
TCI	Total capital investment	\$
u_g	Gas velocity	$\mathrm{m\,s^{-1}}$
u_l	Liquid velocity	$\mathrm{m\,s^{-1}}$
u_x	Flow velocity in x direction	$\mathrm{m\,s^{-1}}$

V_{cell}	Electrolyser cell potential	V
$\dot{V}_{\text{r}}$	Volumetric flow rate through electrolyser	$\text{m}^3\,\text{s}^{-1}$
W	Channel width	m
x	Coordinate in flow direction	m
y	Coordinate perpendicular to the flow direction	m
z_{r}	Amount of transferred electrons in reaction r	-

Greek		
α_{r}	Transfer coefficient of the reaction r	-
β	Fitting factor for the cost correlation of the PSA unit	-
$\delta_{\text{c}}(x)$	Liquid boundary layer thickness	m
ϵ	Porosity	-
η_r	Overpotential of the reaction r	V
η_{Ω}	Ohmic losses	V
κ	Conductivity	$\text{S}\,\text{m}^{-1}$
$\nu_{k,r}$	Stochiometric coefficient of species k in reaction r	-
τ	Tortuosity	-
χ_{het}	Heterogeneous conversion	-
χ_{hom}	Homogeneous consumption	-
χ_{tot}	Overall conversion	-

APPENDIX

4.A. HOMOGENEOUS CONVERSION IN MODEL M2

The *simplistic* channel scale model M2 is represented by a plug flow reactor in which the CO_2 flow is reacting at the channel wall in the electrochemical reaction (Eq. 4.9). The loss of CO_2 in the homogeneous carbonate reaction (Eqs. 4.15 - 4.16) is not explicitly modelled but simplified by introducing a fixed additional current density at the wall (i_{hom}) which leads to the following species balance for CO_2 based on Eq. 4.1 - 4.2

$$\frac{\partial c_{\mathrm{CO_2,M2}}}{\partial x} = -\frac{2\left(i_{\mathrm{C_2H_4}} + i_{\mathrm{hom}}\right)}{12 F u_{\mathrm{g}} H} \tag{4.34}$$

This approach allows to include a homogeneous consumption term, which solely depends on the gaseous flow rate for a fixed additional current density ($i_{\mathrm{hom}} = 50\,\mathrm{mA\,cm^{-2}}$) [12, 27]. To calculate the homogeneous consumption we need to know how much CO_2 is consumed by this additional current density. We determine this by solely considering the reaction due to the additional current density i_{hom} in Eq. 4.34. The change in CO_2 concentration over the channel length based on the additional current density is given by

$$\int_{c_{\mathrm{CO_2,hom,M2}}(x=0)}^{c_{\mathrm{CO_2,hom,M2}}(L)} dc = -\frac{2 i_{\mathrm{hom}}}{12 F u_{\mathrm{g}} H} \int_0^L dx. \tag{4.35}$$

The homogeneous consumption for this simplification equals the total conversion (Eq. 4.18)

$$\chi_{\mathrm{hom}} = \frac{c_{\mathrm{CO_2,hom,M2}}(x=0) - c_{\mathrm{CO_2,hom,M2}}(x=L)}{c_{\mathrm{CO_2,hom,M2}}(x=0)} = \frac{2 i_{\mathrm{hom}} L}{12 F u_{\mathrm{g}} H} \frac{RT}{P}, \tag{4.36}$$

with the concentration of CO_2 at the channel inlet given by the ideal gas law. For a single channel gas flow rate of 10 sccm and the herein used channel geometry the homogeneous consumption comes out to be $\chi_{\mathrm{hom}} = 0.13$ (Table 4.2).

4.B. MODEL PARAMETERS

The parameters for the simulations are summarised in Table 4.5.

Table 4.5: Input parameters for channel scale models.

Parameter	Description	Value	Unit	Reference
Operating conditions				
u_g	Gas velocity	$1.00 \cdot 10^{-3}$	[m s^{-1}]	-
u_l	Liquid velocity	0.54	[m s^{-1}]	-
η_c	Cath. overpotential	-0.70 to -0.90	[V]	30
T	Temperature	300	[K]	-
P	Pressure	$1.00 \cdot 10^{5}$	[Pa]	-
Geometry				
ϵ	Porosity	0.70	[-]	30
H	Channel height	$1.00 \cdot 10^{-3}$	[m]	26
W	Channel width	0.01	[m]	26
L	Channel length	0.10	[m]	-
H_c	Cat. layer thickness	$3.00 \cdot 10^{-6}$	[m]	30
H_m	Mem. layer thickness	$115 \cdot 10^{-6}$	[m]	46
Species/material properties				
D_{CO_2}	Diffusion coeff. CO_2	$1.91 \cdot 10^{-9}$	[m^2 s^{-1}]	50
D_{OH^-}	Diffusion coeff. OH^-	$5.30 \cdot 10^{-9}$	[m^2 s^{-1}]	50
$D_{CO_3^{2-}}$	Diffusion coeff. CO_3^{2-}	$0.92 \cdot 10^{-9}$	[m^2 s^{-1}]	50
$D_{HCO_3^-}$	Diffusion coeff. HCO_3^-	$1.91 \cdot 10^{-9}$	[m^2 s^{-1}]	50
$H_{CO_2,elec.}$	Henry constant CO_2	0.85 [5]	[-]	51
Electrochemical properties				
κ_e	Electrolyte conduct.	5.50	[S m^{-1}]	52
κ_m	Membrane conduct.	9.30	[S m^{-1}]	46
$i_{0,OER}$	Exch. current density OER	$1.00 \cdot 10^{-7}$	[A m^{-2}]	53
$c^{ref}_{CO_2}(aq)$	Reference concentration	34.0	[mol m^{-3}]	-
E^0_c	Standard eq. potential cathode	0.08	[V]	-
E^0_a	Standard eq. potential anode	1.23	[V]	-

[5] Converted to concentration form at standard conditions.

4.C. *Full* CHANNEL SCALE MODEL M3

The electrochemical reactor setup under consideration is the gas diffusion electrode (GDE) cell with an electrolyte gap, as described in Figure 4.6. The channels of the GDE-cell are situated on a flowplate, where the gas-flow is directed co-currently to the electrolyte flow in the liquid flow chamber. The gas- and liquid flow chamber are separated by the gas-diffusion layer and the catalyst layer, whereas the liquid flow chamber itself is separated by a membrane. The *full* channel model M3 formulated in this work only encapsulates the domains which are considered dominant for the transport and reaction of the main reactants and products, those being the gas flow chamber, the catalyst layer, and the liquid boundary layer. Hence it is assumed that the height of the gas diffusion layer can be neglected for gas phase transport and that gaseous species do not diffuse into the bulk electrolyte. Other physical effects necessary to describe the overall cell performance are derived from approximate relationships. The domains in which this is done are shown in Figure 4.6 bordered by dashed red lines, while the compartments which are explicitly modeled are framed by solid red lines.

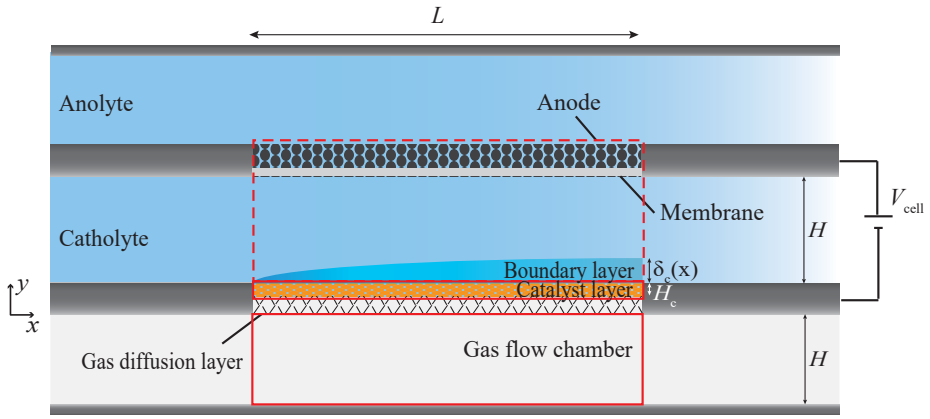

Figure 4.6: Schematic of a single channel in the considered GDE cell. Model domains which are treated explicitly have a solid red border, those for which approximate relationships are used have a dashed red border.

4.C.1. DERIVATION OF GOVERNING GAS CHANNEL EQUATION

In this Section, the derivation of the governing equation for the gas channel (Eq. 4.1) is presented, starting from the generic form of a species balance and simplifying it by assuming unidirectional flow with convective transport dominating diffusive transport in the x-direction,

$$\frac{\partial c_\mathrm{k}}{\partial t} = -\frac{\partial c_\mathrm{k}}{\partial x} u_x(y) + D_\mathrm{k} \frac{\partial^2 c_\mathrm{k}}{\partial y^2}. \tag{4.37}$$

Assuming steady state, and integrating over the channel height (y-direction), hereby exploiting the mean value theorem for integrals, we obtain the following expression

$$\begin{aligned} 0 &= -\frac{1}{H}\int_0^{-H} \frac{\partial c_\mathrm{k}}{\partial x}\, u_x(y)\, dy + \frac{D_\mathrm{k}}{H}\int_0^{-H} \frac{\partial^2 c_\mathrm{k}}{\partial y^2}\, dy, \\ \rightarrow 0 &= -\frac{\partial c_\mathrm{k}}{\partial x}\, u_\mathrm{g} + \frac{D_\mathrm{k}}{H}\left[\frac{\partial c_\mathrm{k}}{\partial y}\right]_0^{-H}. \end{aligned} \tag{4.38}$$

Note that in Eq. 4.38, the definition of the *mixing cup velocity* [38] has been used, denoted as u_g. It is equal to the gas velocity when assuming plug flow behaviour. The integral appearing in the second term can be readily evaluated by realising that at the gas-catalyst interface ($y = 0$) the equality of fluxes is imposed, while at the opposing wall ($y = -H$) a no-flux condition holds, i.e.

$$\begin{aligned} -D_\mathrm{k}\left.\frac{\partial c_\mathrm{k}}{\partial y}\right|_{x,y=0} &= \dot{n}_{\mathrm{k,gl}}(x), \\ \left.\frac{\partial c_\mathrm{k}}{\partial y}\right|_{x,y=-H} &= 0. \end{aligned} \tag{4.39}$$

Inserting these boundary conditions into Eq. 4.38 yields

$$0 = -\frac{\partial c_\mathrm{k}}{\partial x}\, u_\mathrm{g} + \frac{D_\mathrm{k}}{H}\left(-\frac{\dot{n}_{\mathrm{k,gl}}(x)}{D_\mathrm{k}} - 0\right). \tag{4.40}$$

Three species are considered to be present in the gas phase, those being C_2H_4, CO_2, and H_2. Therefore, three initial conditions are required at the channel inlet to solve all concentration profiles. These are given as:

$$c_{\mathrm{CO_2}}(x=0) = \frac{P}{RT}, \quad c_{\mathrm{H_2}}(x=0) = 0, \quad c_{\mathrm{C_2H_4}}(x=0) = 0. \tag{4.41}$$

It is hence assumed that CO_2 is present as a pure ideal gas at the channel inlet.

4.C.2. BOUNDARY CONDITIONS

The governing equations for the gas flow channel, the catalyst layer, and the boundary layer (Eqs. 4.1 - 4.6) give rise to a set of differential equations that are second order in y, each requiring two boundary conditions for a unique solution. These boundary conditions have to be met at the catalyst-gas interface at $y = 0$ and at the boundary layer/electrolyte interface at $y = H_\mathrm{c}+\delta_\mathrm{c}(x)$ (Figure 4.6), making it a boundary value problem. The physical behaviour of the considered species at these boundaries is mainly governed by the aggregate state of the respective species, hence it is sensible to group the boundary conditions accordingly. Since it is assumed that the gaseous products are instantly transported into the gas channel upon formation, only CO_2 needs to be accounted for. For the CO_2 solvated within the catalyst layer, thermodynamic equilibrium with the gas-phase is assumed at the catalyst-gas interface (computed via Henry's law), while no crossover is assumed at the extent of the boundary layer (no-flux condition). It

is known that crossover of CO_2 into the electrolyte may occur, however this is neglected in this case. Hence, the boundary conditions for CO_2 can be written as

$$\begin{aligned} c_{CO_2}(x, y = 0) &= c_{CO_2,g}(x) H_{CO_2,elec.}, \\ \left.\frac{\partial c_{CO_2}}{\partial y}\right|_{x,y=H_c+\delta_c(x)} &= 0 \end{aligned} \tag{4.42}$$

The Henry constant $H_{CO_2,elec.}$ is hereby approximated to be that of CO_2 in pure water at ambient conditions. For ionic species, the boundary conditions are opposed to those of the gaseous species. Ionic species cannot diffuse from the catalyst into the gas-phase, hence a no flux condition is imposed on the catalyst-gas channel interface. The concentration of ionic species at the extent of the boundary layer is set to be the equilibrium concentration in the bulk electrolyte, which depends on the concentration of the electrolyte. The boundary conditions for ionic species follow as

$$\begin{aligned} \left.\frac{\partial c_k}{\partial y}\right|_{x,y=0} &= 0, \\ c_k(x, y = H_c + \delta_c(x)) &= c_{k,elec.}. \end{aligned} \tag{4.43}$$

Figure 4.7 qualitatively depicts the concentration profiles of CO_2 and an exemplary ionic species in the catalyst and boundary layer together with the corresponding boundary conditions at two different x-positions along the channel. Note how the boundary layer is further extended at the second position and how the gas phase concentration of CO_2 is further depleted at that point.

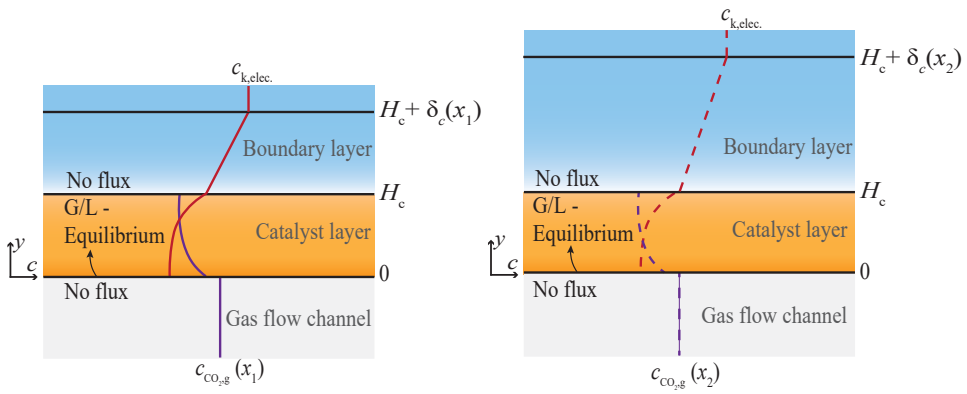

Figure 4.7: Qualitative depiction of the boundary conditions at two different channel positions, x_1 and x_2, with x_2 being further downstream. Axis are not at scale.

4.C.3. KINETIC PARAMETERS

Heterogeneous reactions. Given that C_2H_4 and H_2 are considered as the only products (i.e. not including the whole range of carbonaceous products which can form on a copper catalyst) it is refrained from estimating the heterogeneous reactions parameters for every possible reaction, and instead, an overall current-voltage relationship for the cathode side of the cell is used. The reason for this simplification is twofold:

1. The local reaction environment is known to strongly influence product distribution. To the best of the author's knowledge, there exists no kinetic framework which can account for this.

2. A simplistic kinetic approach is deemed favourable for comparing different operational modes for large scale CO_2 electrolysers, as intended in this work.

To obtain the desired estimate of a possible *i-E* curve for the single channel models M2 and M3, experimental data reported by Tan *et al.* [30] is fitted through the Butler-Volmer equation

$$i_{\text{tot}} = i_0 \exp\left(-\frac{\alpha_c F}{RT}\left(E_c - E_c^0\right)\right) \tag{4.44}$$

using a least squares minimisation with α_c and i_0 as fitting parameters. The experiments were conducted with a GDE-based flow electrolyser with copper nanoparticles on carbon paper and 1M $KHCO_3$ as catholyte [30]. This study has been chosen as the experimental setup is well defined and representative of the modelling domain considered herein. The obtained values of the fitting parameters and their 95% interval are presented in Table 4.6. The resulting *i-E* curve together with the 95% confidence is plotted in Figure 4.8. Contrary to the experimental data ethylene is considered as the only carbonaceous product. The fitted kinetic constants shown in Table 4.6 are taken as the kinetic constants for calculating the total current density. Since CO_2 is mass transfer limited the partial current density for ethylene is then given by the mass-transfer dependent Butler-Volmer equation which includes the concentration overpotential based on the Nernst equation (Eq. 4.13) and shares the same Butler-Volmer constants as the total current density and the partial current density for the hydrogen formation. This simplifying assumption for the kinetic constants is motivated by the difficulty in fixing the individual kinetic constants for each cathode reaction in the Butler-Volmer equation as discussed by Brée *et al.* [46]. The uncertainty in determining the kinetic constants arises from the data scarcity and that reported values vary drastically for different experimental studies,

Table 4.6: Fitting parameters and their 95% confidence interval obtained by fitting the Butler-Volmer equation (Eq. 4.44) to the experimental $i-E$ curve by Tan *et al.* [30].

Parameter	Unit	Value
α_c	[-]	0.26
$\alpha_{c,95}$	[-]	−0.28 to 0.79
i_0	[mA cm^{-2}]	0.022
$i_{0,95}$	[mA cm^{-2}]	−0.41 to 0.46

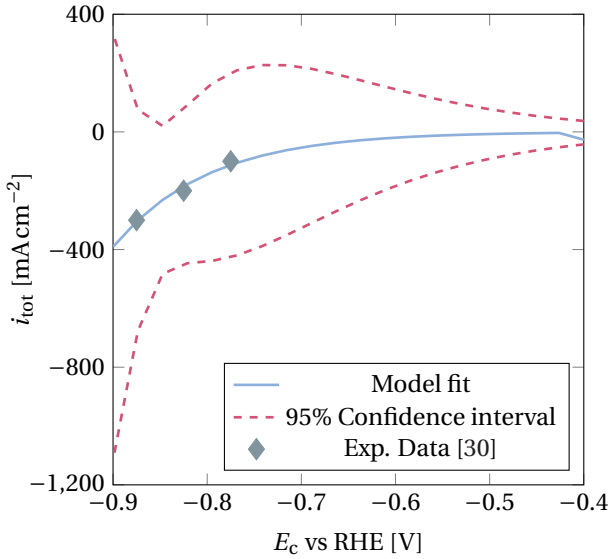

Figure 4.8: Experimental data [30] and model fit together with 95% confidence interval.

as the kinetic constants are difficult to decouple from the mass transport phenomena occurring in the cell [54]. By simplifying the kinetic constants as explained above the partial current densities in this study can be directly calculated with the one set of fitted kinetic constants. The influence of this assumption is discussed in the following Section 4.C.4 (appendix). It can be seen that, while the experimental data points seem to be well represented with the Butler-Volmer equation with $\alpha_c = 0.26$ and $i_0 = 0.022\,\mathrm{mA\,cm^{-2}}$ as fit parameters, the confidence intervals $\alpha_{c,95}$ and $i_{0,95}$ are rather large. In fact, the 95 % confidence interval $\alpha_{c,95}$ exceeds the lower limit drops below 0. These large values for the confidence intervals of both fit parameters can be attributed to the small number of data points, a problem also encountered in similar CO_2RR modelling studies [46]. While many kinetic studies of CO_2RR on copper electrodes have been conducted, the number of studies utilising GDE cells at high current densities is still limited and therefore, few studies are available containing more data points. Considering the restricted pool of reported experiments, the data provided by Tan *et al.* [30] seem the best fit for the current purpose.

Homogeneous reactions. The kinetic constants for the homogeneous buffer reaction are taken from Schulz *et al.* [55] and are corrected for the electrolyte salinity [56]. A summary of the values can be found in Table 4.7 for 1M $KHCO_3$ electrolyte solution.

4.C.4. COMPARISON OF THE PREDICTION OF MODEL M3 WITH LITERATURE

The two modelling studies [26, 49] on CO_2 electrolyser designs which similar to this work resolve the local effects along the channel length are not straightforwardly comparable to the herein presented results as they consider a different catalyst and therefore products with a different amount of electrons transferred per reaction. Yang *et al.* [49] consider the

Table 4.7: Reaction rate constants for homogeneous buffer reactions.

Forward rate [$m^3\,mol^{-1}\,s^{-1}$]	Reverse rate [s^{-1}]
$k_{f1} = 5.93$	$k_{r1} = 1.34 \cdot 10^{-4}$
$k_{f2} = 1.00 \cdot 10^{-5}$	$k_{r2} = 2.15 \cdot 10^{-4}$

formation of $HCOO^-$, while Kas *et al.* [26] consider a silver catalyst with the main product being CO. Both of these reduction products require a 2 electron transfer reaction while the reaction chosen in this study towards ethylene requires a 12 electron transfer reaction. Further, the kinetics for the heterogeneous electrochemical reaction are simplified under the assumption that either CO_2 is reduced or H_2 is formed which is comparable to a constant current (galvanostatic) control (see Section 4.2.1). Kas *et al.* [26] presented for the first time the trade-off between heterogeneous conversion and homogeneous consumption of CO_2. As this trade-off is the main driver for the herein acquired results, their study was chosen as a point of comparison to validate the single channel model. For this purpose, the liquid flow rate and the channel length are adapted in this Section to the ones presented by Kas *et al.* [26] to $1\,mL\,min^{-1}$ and 1 cm. Further, the model developed in this work is adjusted from a 12 electron transfer to 2 electron transfer reaction for the purpose of comparison in this Section. The predicted heterogeneous conversion and homogeneous consumption for different single channel gas flow rates are compared in Figure 4.9. Additionally, to compare the impact of the simplified reaction kinetics on the overall trends, the reaction kinetics in model M3 are changed to the Butler-Volmer kinetics and its constants, as presented in the work by Kas *et al.* [26] and referred to as BV kinetics in Figure 4.9.

The results of this work and the work by Kas *et al.* [26] show a comparable trend for varying single channel gas flow rates, while the heterogeneous conversion for increasing current densities is lower in this work. As expected, the homogeneous consumption rate is then overpredicted. This is most likely rooted in the assumption of a fully flooded catalyst layer in this work compared to an ideally wetted catalyst layer in the work by Kas *et al.* [26]. Weng *et al.* [20] show that for a fully flooded catalyst layer the CO_2 concentration, and hence, Faradaic efficiency, decrease for higher current densities compared to an ideally wetted catalyst layer due to an increase in local pH and the bicarbonate buffer reaction. It is therefore, no surprise that the homogeneous consumption due to the bicarbonate buffer reaction is predicted higher with our model compared to the work by Kas *et al.* [26], leading similarly to a decreased heterogeneous conversion rate. Whether, the catalyst layer is fully flooded, partially flooded, or ideally wetted, depends on multiple parameters such as GDE fabrication, operating conditions, and duration of the reaction. Generally, a fully or partially flooded catalyst layer is expected under long term operation. Sisler *et al.* [12] note that the loss of CO_2 due to the homogenous consumption is often underestimated. Therefore a fully flooded catalyst layer, which present the most restricted operating regime, was chosen for this work.

Comparing the predictions for conversion and consumption of this work for the incorporation of the full Butler-Volmer kinetics (dashed line) and the simplified Butler-Volmer kinetics (dotted line) in Figure 4.9, we observe that the conversion is predicted

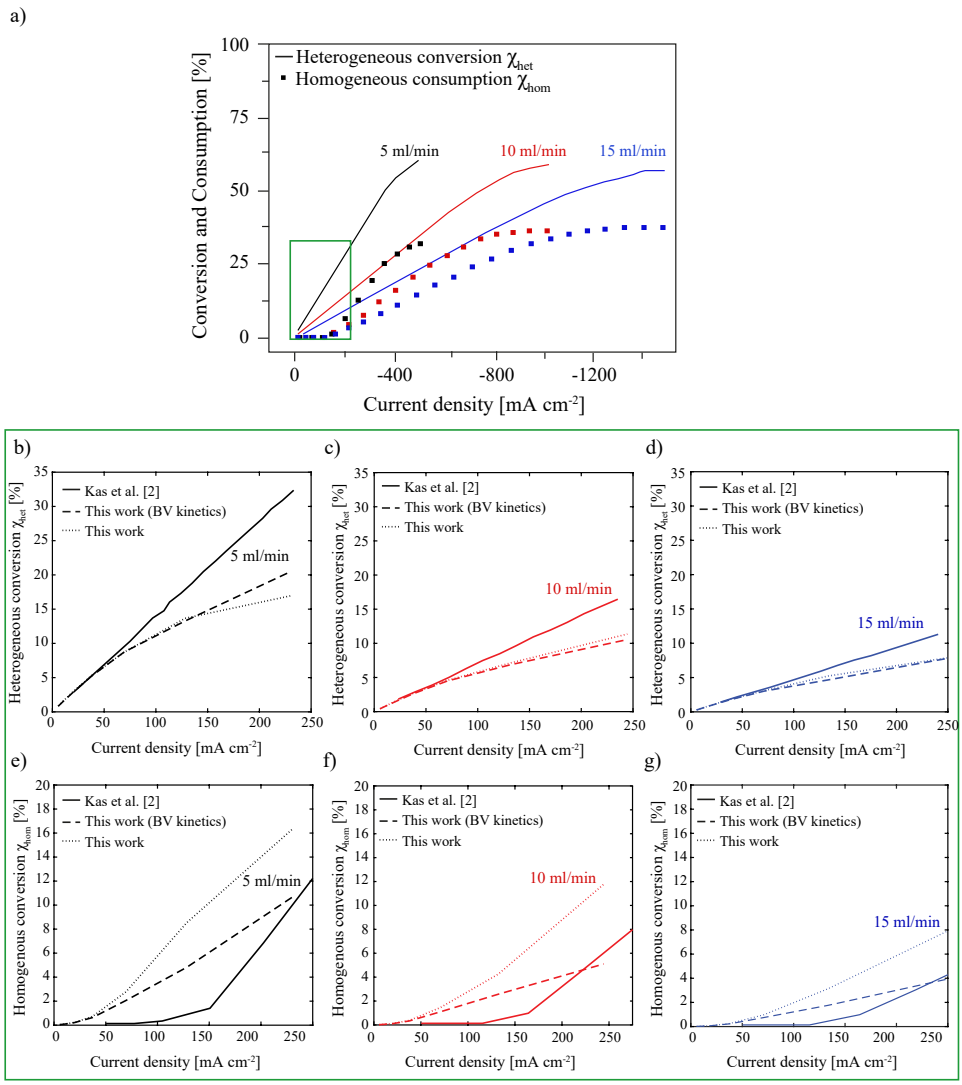

Figure 4.9: Numerical results for the heterogeneous electrochemical conversion from CO_2 to CO and the homogeneous consumption of CO_2 in the carbon equilibrium reaction from Kas *et al.* [26] a). Zoomed in region for the relevant current density range used in this study comparing the numerical results from Kas *et al.* [26] with the numerical results obtained with the *full* channel model M3 in this work for varying single channel gas flow rates b)-g). The numerical results for M3 considering the Butler-Volmer kinetics uses the values reported by Kas *et al.* [26] (dashed lines), while the simplified kinetics (dotted line) are selected and used in this work.

similar by both approaches while the consumption is overestimated in the case of the simplified kinetics. This is expected as for the full Butler-Volmer kinetics a fixed electrode potential is applied leading to a fixed partial current density for hydrogen and hence a fixed flux of OH^- along the electrode. The partial current density towards CO is changing

along the electrode with the change in CO_2 concentration. This leads to a varying total current density for the full Butler-Volmer kinetics, which is averaged over the length for varying cathode potentials. The simplified Butler-Volmer kinetics similarly predict a varying partial current density of CO depending on the CO_2 concentration, leading to a similar prediction in heterogeneous conversion. Contrary, to the full Butler-Volmer kinetics, in the current paper, a fixed total current density is assumed over the electrode length. This assumption leads to an increase in hydrogen formation and production of OH^-. The increase in pH is believed to be the main reason for the observed increased homogeneous consumption rate. It is further interesting to note that even though this also affects the local CO_2 concentration, the impact on the heterogeneous conversion is negligible.

To further test the validity of the herein taken assumption and the simplification of the Butler-Volmer kinetics, the predicted partial current density towards ethylene with varying flow rates is compared to the experimental data by Tan *et al.* [30] in Figure 4.10 a). In the work by Tan *et al.* [30] a copper catalyst, which forms various C1 and C2+ products, is studied. In the current study ethylene is considered as the only CO_2 reduction product (which allows to simplify the post-process steps). We note that a catalyst which selectively produces ethylene has so far not been reported and hence presents a simplification in this study. For a point of comparison the sum of the partial current densities for the C1 and C2+ products from Tan *et al.* [30] is taken and compared to the predicted current density towards ethylene. Figure 4.10 a) shows that for a total current density of 100 mA cm^{-2}, the partial current density with varying flow rate is predicted well, while for a total current density of 200 mA cm^{-2}, especially for low single channel gas flow rates, the partial current density towards ethylene is underpredicted. We note that the amount of electrons transferred varies widely for the individual C1 and C2+ products which could be a reason for the observed difference in partial current densities. Comparing the predicted heterogeneous conversion for varying single channel gas flow rates with the ex-

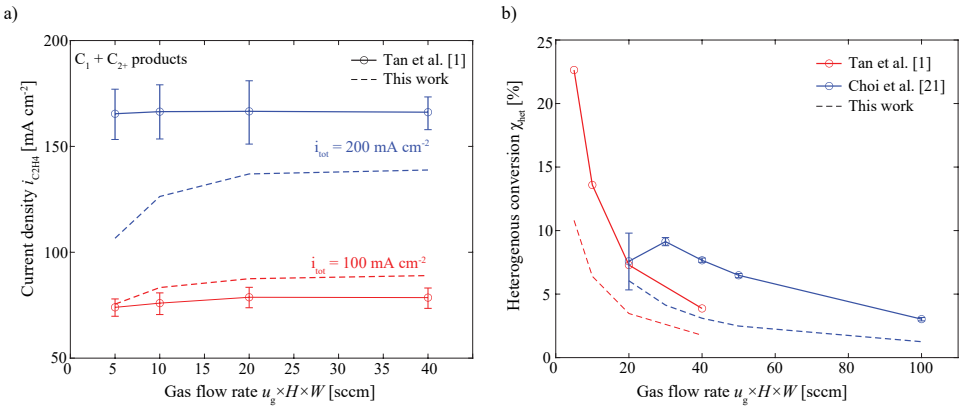

Figure 4.10: Numerical results for varying flow rates of a) the partial current density of ethylene in comparison to the sum of the partial current densities of C products obtained experimentally in the work by Tan *et al.* [30], b) the heterogeneous conversion in comparison to the experimental data by Tan *et al.* [30] and Choi *et al.* [32].

perimental data by Tan *et al.* [30] and Choi *et al.* [32] shows a similar trend while the absolute values are being under predicted. This has already been observed in Figure 4.9 for the comparison with the data from Kas *et al.* [26] and the discrepancy in absolute values might similarly be due to the assumption of a fully flooded catalyst layer which might not be the case for the reported experimental values.

Conclusively, we note that while the absolute values cannot be predicted with the herein presented model and assumptions, the trends and trade-offs follow the experimentally and numerically observed trends. In this light, we reiterate that the current paper aims to show the trade-offs between conversion and consumption and their impact across scales and does not aim to provide new target values for electrolyser development as absolute values highly depend on the modelling assumptions, as shown above and throughout this study. Therefore, the sensitivity and accuracy of the proposed model is adequate to the purpose of the current paper.

4.D. ELECTROLYSER SCALE MODEL

The required electrolyser area, A_r is the most important variable for the capital investment costs and depends on the desired production rate according to

$$\dot{F}_{\mathrm{C_2H_4,target}} = A_\mathrm{r} \int_0^{H_\mathrm{c}} < \dot{N}_{\mathrm{C_2H_4,het}} > dy, \tag{4.45}$$

with $< \dot{N}_{\mathrm{C_2H_4,het}} >$ the channel length-averaged rate. Solving the integral in Eq. 4.45 with Eq. 4.11 leads to

$$\dot{F}_{\mathrm{C_2H_4,target}} = A_\mathrm{r} \frac{< i_{\mathrm{C_2H_4}} >}{12F}, \tag{4.46}$$

with $< i_{\mathrm{C_2H_4}} >$ the channel length-averaged current density. The required electrolyser area A_r as presented in Eq. 4.21 is obtained by combing Eq. 4.46 with the definition of the Faradaic efficiency

$$FE_{\mathrm{C_2H_4}} = \frac{i_{\mathrm{C_2H_4}}}{i_\mathrm{tot}}. \tag{4.47}$$

Assuming that the number of channels linearly scales with the reactor performance the relation between the required electrolyser area A_r and the volumetric gas flow rate $\dot{V}_\mathrm{r}$ leaving the electrolyser is given as

$$\dot{V}_\mathrm{r} = u_\mathrm{g} H \frac{A_\mathrm{r}}{L}. \tag{4.48}$$

Knowing that $\dot{F}_{\mathrm{C_2H_4,target}} = c_{\mathrm{C_2H_4}}(x = L)\dot{V}_\mathrm{r}$ the Faradaic efficiency can further be expressed in terms of the gas velocity and product concentration at the channel outlet (Eq. 4.21) by rearranging Eq. 4.47 with Eq. 4.48. The volumetric gas flow rate $\dot{V}_r$ (Eq. 4.24) leaving the electrolyser and entering the PSA unit can further be expressed from the definition of the heterogeneous conversion (Eq. 4.19)

$$\chi_\mathrm{het} = \frac{2c_{\mathrm{C_2H_4}}(x = L)}{c_{\mathrm{CO_2}}(x = 0)} \frac{\dot{V}_\mathrm{r}}{\dot{V}_\mathrm{r}} = \frac{2\dot{F}_{\mathrm{C_2H_4,target}}}{c_{\mathrm{CO_2}}(x = 0)\dot{V}_\mathrm{r}}. \tag{4.49}$$

The electrolyser unit is embedded in a Reaction-Separation-Recycle process (see Figure 4.11), in which the flowrate fed into the reactor is composed of an external stream ($\dot{m}_{CO_2,in}$) and a recycle stream ($\dot{m}_{CO_2,recycle}$). The magnitude of the recycle stream depends on the purity of the end product and the achieved conversion within the reactor itself. Perfect separation for the CO_2 stream in the PSA unit is assumed. For the current purpose, assuming a perfect separation is justifiable since this is *a)* commonly done for preliminary design optimisations [57] and *b)* the separation efficiencies for PSA are reported to be quite high for similar feed streams [58]. The required CO_2 supply $\dot{m}_{CO_2}$ then depends on the achieved conversion rate. Rewriting the conversion equations (Eqs. 4.18 - 4.19) with $c_i = \dot{m}_i/(M_i\dot{V}_r)$ in terms of mass flow rates under the assumption that the flow velocity is not changing from the electrolyser inlet to outlet (see Section 4.C) gives

$$\chi_{het} = 2\frac{\dot{m}_{C_2H_4,target}}{M_{C_2H_4}}\frac{M_{CO_2}}{\dot{m}_{CO_2}+\dot{m}_{CO_2,recycle}}, \tag{4.50}$$

$$\chi_{tot} = \frac{\dot{m}_{CO_2}}{\dot{m}_{CO_2}+\dot{m}_{CO_2,recycle}}. \tag{4.51}$$

Inserting Eq. 4.50 in Eq. 4.51 and rearranging yields the required supply of fresh CO_2 to the electrolyser

$$\dot{m}_{CO_2} = 2\dot{m}_{C_2H_4,target}\frac{\chi_{tot}}{\chi_{het}}\frac{M_{CO_2}}{M_{C_2H_4}}, \tag{4.52}$$

which together with Eq. 4.20 gives the annual consumption rate of CO_2 (Eq. 4.25).

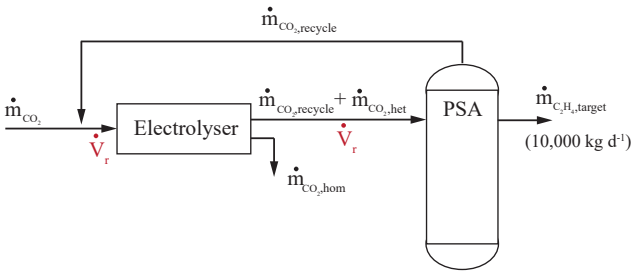

Figure 4.11: Conceptual flow configuration showing the CO_2 containing streams.

4.E. ADDITIONAL CONSTRAINTS

Mitigating voltage losses is crucial for effective cell operation. These losses are constituted by required overpotentials to drive the reactions at the desired rate, as well as ohmic losses and make up the required cell voltage according to Eq. 4.22. At the cathode side, concentration overpotential $\eta_{con,c}$ does not have to be taken into account due to the use of the concentration dependent Butler-Volmer equation (see Eq. 4.13). The activation overpotential is hence given as

$$\eta_c = E_c - E_c^0, \tag{4.53}$$

with the cathode potential E_c vs RHE (reversible hydrogen electrode). The cathode overpotential can be calculated for a given current density i_{tot} from the Butler-Volmer kinetics (Eq. 4.12).

For the OER occurring at the anode, modelling studies have reported negligible contributions of the concentration overpotential $\eta_{con,a}$, which is herein neglected [46, 49]. The anodic activation overpotential on the other hand can become considerable, and must be taken into account. It can be approximated via the following expression

$$\eta_a = \frac{RT}{0.5F} \sinh^{-1}\left(\frac{i_{tot}}{2i_{0,OER}}\right), \tag{4.54}$$

which is referred to as the *hyperbolic sine approximation*. This approximation is exact if the anodic and cathodic charge transfer coefficients in the Bulter-Volmer equation are equal [59]. Note that the OER is the only reaction occurring at the anode, meaning that $i_{0,OER}$ is equal to the cell current density. Ohmic losses are calculated via Ohm's law accounting for the conductivity of the membrane and the electrolyte

$$\eta_\Omega = i_{tot}\left(\frac{H}{\kappa_e} + \frac{H_m}{\kappa_m}\right), \tag{4.55}$$

in which H_m is the membrane thickness, and κ_e, and κ_m are the conductivity of the electrolyte and membrane, respectively. Values can be found in Table 4.5.

4.F. PROCESS SCALE MODEL

4.F.1. LIMITING NPV FOR MODEL M1

As a comparative figure between models M1 to M3, the *relative NPV* (Eq. 4.33) is introduced, which uses max(NPV_{M1}) as a reference value. The *NPV* for each model is calculated based on the multi-scale model introduced in the main manuscript in the section "Multi-scale model". In Figure 4.12 the *NPV* for the *no channel* model M1 is plotted against the current density showing that the *NPV* reaches 99% of its final value at ≈ 600 mA cm^{-2} at ≈ -24 M$, which is taken as max($NPV_{M1}$) in Eq. 4.33.

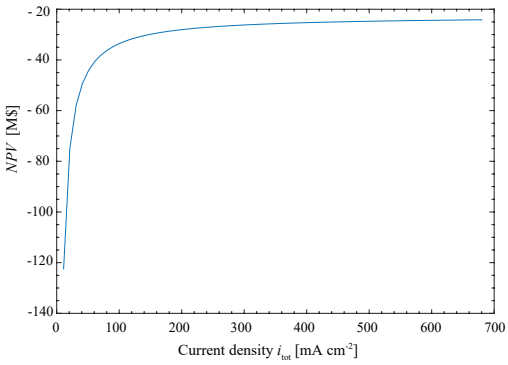

Figure 4.12: *NPV* for the *no channel* model M1 as a function of current density.

4.F.2. SENSITIVITY ANALYSIS

A sensitivity analysis is performed to evaluate the influence of selected process variables and economic parameters on the economic indicator, the NPV. These parameters and their ranges of variation are listed in Table 4.8. The results for the *simplistic* (M2) and *full* (M3) channel model are shown in Figure 4.13.

The NPV is negative for all (individual) ranges of variation. The flow rate and total current density show a significant influence on the obtained NPV, especially for model M3. The sensitivity analysis also shows a significant influence of the electricity costs on the NPV. This matches with conclusions from previous techno-economic studies, which conclude that low electricity prices are essential for the profitable production of higher hydrocarbons via electrochemical CO_2 reduction. The variation in selling price, CO_2 price, and production rate show a lower but also significant influence on the NPV.

Incorporating the channel scale model allows to study the influence of flow rate compared to other studies as this variable now influences the conversion and consumption rates, which are commonly fixed model inputs. The total current density influences the cell voltage, conversion, consumption and Faradaic efficiency. An increase in total current density shows a negative effect on the NPV, while a decrease in total current density seems to improve the NPV. This observation is contrary to results reported in other techno-economic studies [6, 7, 14] in which an increase in current density generally increases the NPV. The influence of the current density and single channel gas flow rate on the NPV is further discussed in Section 4.3.

Table 4.8: Base case and variation ranges for sensitivity analysis.

Sensitivity variables	better	base	worse
Gas flow rate [sccm]	50	10	5
Total current density [$mA\,cm^{-2}$]	300	200	100
Selling price ethylene [$\$\,kg^{-1}$]	+15%	1.3	-15%
Electricity price [$\$\,kW^{-1}\,h$]	0.02	0.03	0.04
CO_2 price [$\$\,kg^{-1}$]	0	0.04	0.07
Electrolyser cost [$\$\,m^{-2}$]	450	920	1840
PSA cost [$\$\,m^{-2}$]	-20%	1990000	+20%
Interest rate [-]	+20%	0.1	-20%
Production rate [$kg\,d^{-1}$]	-20%	10000	+20%
Electrolyser lifetime [yr^{-1}]	-20%	20	+20%

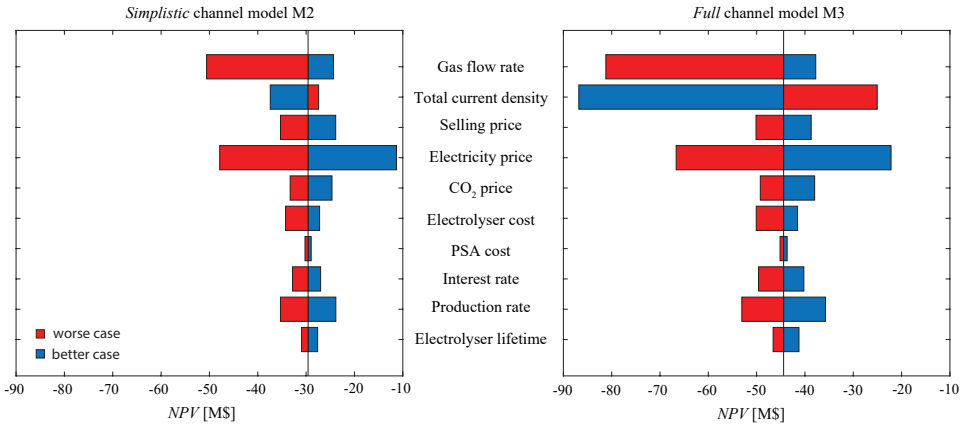

Figure 4.13: Sensitivity analysis of results for CO_2 to ethylene (Table 4.8).

4.G. SCALING RELATION BETWEEN HETEROGENEOUS CONVERSION AND CURRENT DENSITY

The *simplistic* model M2 does not explicitly model the catalyst layer and describes the electrolyser solely as channel flow with a reacting wall. The reaction rate at the wall is described by the partial current density towards C_2H_4 (Eq. 4.13). Combining Eq. 4.34 (omitting the i_{hom} term) and Eq. 4.13 gives

$$\frac{\partial c_{CO_2}}{\partial x} = -\frac{i_{tot}}{6F}\frac{c_{CO_2}}{c^{ref}_{CO_2}(aq)}\frac{1}{u_g H}. \tag{4.56}$$

Integrating over the reactor length x with the boundary condition $c_{CO_2}(x=0) = c^0_{CO_2}$ gives the expected exponential trend for the concentration of CO_2 over the reactor length

$$c_{CO_2}(x) = c^0_{CO_2}\exp\left(-\frac{i_{tot}}{6Fc^{ref}_{CO_2}(aq)}\frac{x}{u_g H}\right). \tag{4.57}$$

For low conversions, the CO_2 concentration drops almost linearly with the total current density i_{tot} for a fixed gas velocity u_g. With the heterogeneous conversion rate in turn depending linearly on the CO_2 concentration (Eq. 4.19), this explains the observed linear trend between heterogeneous conversion rate and total current density.

4.H. FIXED PERFORMANCE VARIABLES FOR MODEL M1

Within this work, all NPVs for the electrochemical CO_2 reduction process to C_2H_4 are found to be negative. This stands in contrast to other publications, such as the seminal paper of Jouny *et al.* [7]. The discrepancy can be explained upon inspection of the employed fixed performance variables for the electrolyser. While prior studies have attempted to find fixed performance variables which render the electrolysis process profitable, this study takes into account their interdependency. While the performance variables are not resolved through the channel scale model of the *no channel* model M1, the interdependencies are taken into account by choosing the fixed performance variables based on a combination of experimental results ($FE_{C_2H_4}$ = 0.70)[29] and calculations taken in this work for the cell potential (V_{cell} = 3.69 V, Eq. 22 in the main manuscript), which is based on the threshold current density of 200 mA cm^{-2} from Jouny *et al.* [7]. Table 4.9 directly compares the selected performance targets used by Jouny *et al.* [7] to the ones used in model M1 of this work. These performance targets act as an input to the electrolyser scale. The *NPV* is then calculated according to the Eqs. 4.18 - 4.27, similar to the *no channel* model M1. As stated, no positive NPV were obtained for the values used in this work as illustrated by the black line in Figure 4.14. To confirm that our electrolyser and process models also yield positive NPVs we computed the NPVs with model M1 for the targets used by Jouny *et al.* [7] as listed in Table 4.9 (red line in Figure 4.14). To illustrate the importance of V_{cell}, we also computed the NPVs for the fixed cell voltage chosen in this work of V_{cell} = 3.69 V (green line in Figure 4.14) instead of the 2.00 V from Jouny *et al.* [7]. Figure 4.14 shows that even with relatively optimistic values used by Jouny *et al.* [7] for both the heterogeneous conversion and the Faradaic efficiency, only the calculations with a cell voltage of 2.00 V achieve a positive NPV for a current density above 100 mA cm^{-2}. The NPV increases with increasing the current density, as the capital investment costs decrease with increasing current density for a fixed cell potential. An increase in fixed cell potential reduces the overall NPV, while the trend with varying current density does not change. The cell potential drives the capital investment costs and is closely linked to the electricity price. When the cell potential is not fixed but its dependency on current density is considered (black line in Figure 4.14) a clear trade-off for increasing current densities is observed. The intersect at around 200 mA cm^{-2}, which equals a cell potential of V_{cell} = 3.69 V shows that an increasing cell voltage decreases the *NPV*. Conclusively, the choice of the fixed performance variables has a strong influence on the NPV of the electrolysis process, with the cell voltage being one of the main cost drivers. This is in line with the sensitivity results reported by Jouny *et al.* [7].

Table 4.9: Comparison of performance targets used in prior work by Jouny *et al.* [7] and in model M1 of this study.

	χ_{het} [-]	$FE_{C_2H_4}$ [-]	V_{cell} [V]	χ_{hom} [-]
Jouny *et al.* [7]	0.50	0.90	2.00	0.00
This work	0.50	0.70[29]	3.69	0.00

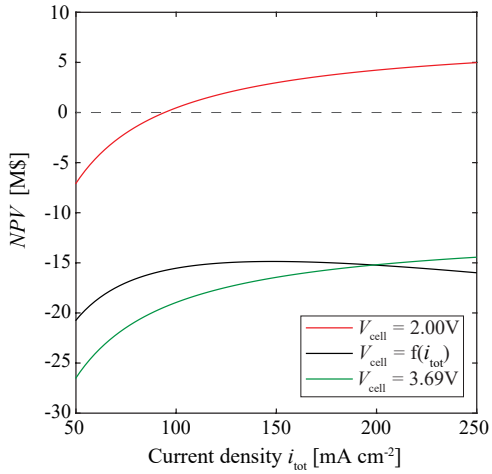

Figure 4.14: Comparison of the *NPV* for model M1 with the performance targets used by us for $V_{cell} = 3.69$ V (green line, reported in the bottom row of Table 4.9) and by Jouny *et al.* [7] for $V_{cell} = 3.69$ V (red line, reported in the top row of Table 4.9) and a variable cell voltage (see Section 4.E, black line)

4.I. SUMMARY OF ASSUMPTIONS AND THEIR IMPACT ON THE RESULTS

The aim of this work is to define a channel scale model which can sufficiently capture the interdependencies between the performance metrics (Faradaic efficiency, current density, cell voltage, heterogeneous conversion, and consumption) to study their influence on the different scales and economic outlook. The constraints for this model include a fast run time to make it suitable for optimisation studies and the limited available data from experimental results, which makes the validation and extraction of kinetic constants difficult [46]. These constraints lead to the following assumptions discussed throughout the main manuscript and summarised below, together with their justification. Further, the foreseen impact of these assumptions on the *NPV* and the optimal operating conditions is discussed.

Assumptions of the *full* channel model M3. In this work only the cathode compartment of a GDE cell is modelled (see Section 4.C). The simplifications in regard of the geometry include that the gas diffusion layer of the cathode electrode is neglected. This layer adds an extra transport resistance for the gases to reach and leave the catalyst layer, since the purpose of this layer is to facilitate their transport. The work by Weng *et al.* [20] shows that the influence on local concentration in the catalyst layer is minimal, justifying that we neglected this layer in this work. Further, species transport is only explicitly modelled in the gas channel, the cathode catalyst layer, and the liquid boundary layer. The extent of the liquid boundary layer is approximated through the Lévêque approximation [37] (Eq. 4.7). The transport in the membrane, the electrolyte flow channels, and at the anode are not modelled. The ohmic resistance of the catholyte chamber and membrane as well as the expected overpotential at the anode are approximated through Ohm's law and the *hyperbolic sine approximation* [59] (Eq. 4.54), respectively. Transport in the gas

channel in the axial direction is dominated by convection. Pressure loss is expected to be small and its effect on flow velocity is therefore neglected. It is further assumed that the chosen catalyst only produces ethylene from CO_2 or hydrogen from water. However, a catalyst which can selectively produce ethylene is so far not known. The most common catalyst used to produce higher hydrocarbons via electrochemical CO_2 reduction is copper, which produces a variety of gas and liquid CO_2 reduction products. Including a specific catalyst in the channel scale model, requires the kinetics of all products to be described by the Butler-Volmer equation (Eq. 4.12) with all individual kinetics constants. Nevertheless, most of the kinetic constants reported in literature vary significantly between different studies and reactor designs as it is difficult to decouple them from the mass transfer and local reaction conditions in the reactor [54]. Therefore the reaction kinetics in this work are simplified with the only carbonaceous product being ethylene and therefore neglecting any additional gas and liquid products forming from CO_2. The catalyst layer is assumed to be fully flooded, while stability issues like gas breakthrough due to a pressure difference between the gas and liquid channel [60] are neglected. Transport in the liquid phase is therefore mainly given by diffusion. Diffusion is further corrected for the porosity of the catalyst layer. The phase-transfer occurs at the gas-liquid boundary at the gas channel side. In the catalyst layer the electrochemical reaction and the homogeneous carbonate buffer reaction take place and act as a sink term for the CO_2. It is assumed that the reactor is constantly fed with fresh 1M $KHCO_3$ electrolyte, while recycling and post-treatment of the electrolyte is not considered in the costs. Further, migration of bicarbonate/carbonate ions is neglected [20, 26] as only the cathode compartment is modelled. The resulting carbon balance from these assumptions is shown in Figure 4.15 a). The CO_2 lost to the carbonate buffer reaction is not recovered. Hence an increase in bicarbonate/carbonate formation leads to a decrease in the *NPV*.

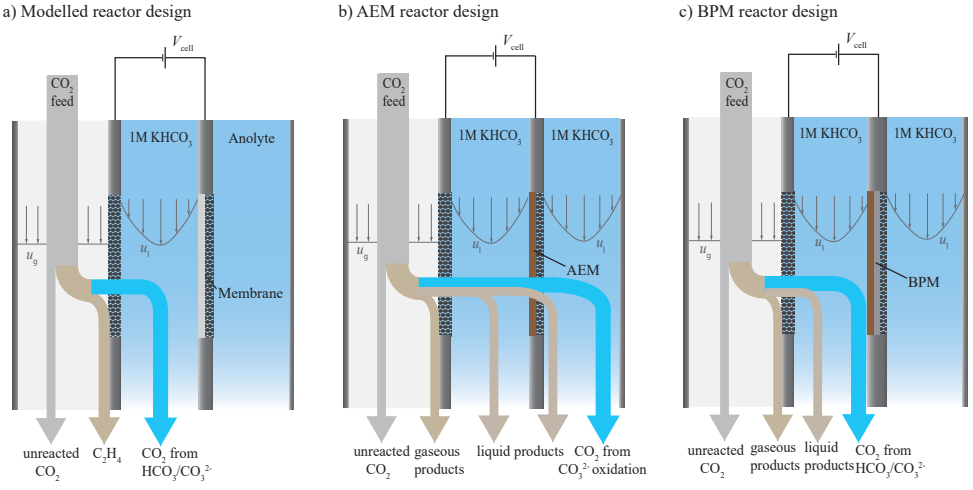

Figure 4.15: Carbon balance for the modelled a), an anion exchange membrane (AEM) b), and a bipolar membrane (BPM) c) GDE reactor.

Impact of assumptions on results. In comparison to the carbon balance resulting from the modelling assumptions (Figure 4.15 a)) the expected carbon balance for GDE reactors with a fixed type of membrane and anolyte are shown in Figure 4.15 b) and c). For a copper catalyst at the cathode various gaseous and liquid carbonaceous products are expected to form. Considering additional gaseous products increases the required post-treatment steps for the cathode gas stream to separate the products, which adds additional investment and operating costs. It is expected that the profit from these products does not balance the additional costs therefore leading to a decrease of the overall *NPV*. Considering the effect of gas composition and the effect on separation efficiency further leads to higher optimal conversion rates compared to our study. The electrolytes are commonly recirculated, therefore liquid products need to be separated from the liquid streams to avoid accumulation. For anion exchange membrane (AEM) reactors up to 30 - 40% of the liquid products can crossover the membrane to the anode side and be oxidised [61]. The effect of oxidation on the overall cell potential is generally low, therefore no changes in the predicted optimal current density and gas flow rate are expected. The AEM further allows for bicarbonate and carbonate ions to migrate to the anode side. It was found that under steady-state conditions the catholyte pH becomes alkaline and the main charge carrier is carbonate [33]. The carbonate ions which migrate from the cathode to the anode then react in the liquid anolyte with the H^+ ions from the water splitting reaction. This leads to the formation of CO_2 gas in the anolyte. Considering this effect the loss of CO_2 is expected to increase [35]. An increase in the consumption rate of CO_2 intensifies the trade-offs shown between model M2 and M3 and shifts the optimal performance to lower CO_2 conversions. One approach to minimise liquid product and carbonate crossover to the anode is the use of bipolar membranes [34, 62]. However for these membrane types the ohmic loss and hence the overall cell voltage increase. An increase in cell voltage leads to a decrease of the overall *NPV* as discussed in Section 4.H (appendix).

Overall it is expected that the absolute values for the *NPV* decrease if the required additional cleaning steps for the gas and liquid streams are considered. Further, the optimal operating conditions are expected to vary when considering a variety of products or additional loss terms for CO_2 such as degassing due to migration. However, the presented trade-offs and sensitivity towards the process economics are expected to be similar. Including the channel scale model into existing process models which consider additional pre- and post-treatment units presents an interesting next step and could for example give clarity under which conditions the recovery of the degassed CO_2 is desirable.

REFERENCES

[1] I. Bagemihl, L. Cammann, M. Pérez-Fortes, V. van Steijn, and J. R. van Ommen, *Techno-economic assessment of CO_2 electrolysis: How interdependencies between model variables propagate across different modeling scales,* ACS Sustainable Chemistry & Engineering **11**, 10130 (2023).

[2] G. A. Olah, A. Goeppert, and G. K. S. Prakash, *Chemical recycling of carbon dioxide to methanol and dimethyl ether: From greenhouse gas to renewable, environmentally carbon neutral fuels and synthetic hydrocarbons,* The Journal of Organic Chemistry **74**, 487 (2009).

[3] E. V. Kondratenko, G. Mul, J. Baltrusaitis, G. O. Larrazábal, and J. Pérez-Ramírez, *Status and perspectives of CO_2 conversion into fuels and chemicals by catalytic, photocatalytic and electrocatalytic processes,* Energy & Environmental Science **6**, 3112 (2013).

[4] B. Kumar, J. P. Brian, V. Atla, S. Kumari, K. A. Bertram, R. T. White, and J. M. Spurgeon, *New trends in the development of heterogeneous catalysts for electrochemical CO_2 reduction,* Catalysis Today **270**, 19 (2016).

[5] B. Endrődi, G. Bencsik, F. Darvas, R. Jones, K. Rajeshwar, and C. Janáky, *Continuous-flow electroreduction of carbon dioxide,* Progress in Energy and Combustion Science **62**, 133 (2017).

[6] S. Verma, B. Kim, H.-R. M. Jhong, S. Ma, and P. J. A. Kenis, *A gross-margin model for defining technoeconomic benchmarks in the electroreduction of CO_2,* ChemistrySustainability-Energy-Materials **9**, 1972 (2016).

[7] M. Jouny, W. Luc, and F. Jiao, *General techno-economic analysis of CO_2 electrolysis systems,* Industrial and Engineering Chemistry Research **57**, 2165 (2018).

[8] M. J. Orella, S. M. Brown, M. E. Leonard, Y. Román-Leshkov, and F. R. Brushett, *A general technoeconomic model for evaluating emerging electrolytic processes,* Energy Technology **8**, 1900994 (2020).

[9] J. M. Spurgeon and B. Kumar, *A comparative technoeconomic analysis of pathways for commercial electrochemical CO_2 reduction to liquid products,* Energy & Environmental Science **11**, 1536 (2018).

[10] M. H. Barecka, J. W. Ager, and A. A. Lapkin, *Economically viable CO_2 electroreduction embedded within ethylene oxide manufacturing,* Energy & Environmental Science **14**, 1530 (2021).

[11] M. Ramdin, A. R. T. Morrison, M. de Groen, R. van Haperen, R. de Kler, E. Irtem, A. T. Laitinen, L. J. P. van den Broeke, T. Breugelmans, J. P. M. Trusler, W. d. Jong, and T. J. H. Vlugt, *High-pressure electrochemical reduction of CO_2 to formic acid/formate: Effect of pH on the downstream separation process and economics,* Industrial & Engineering Chemistry Research **58**, 22718 (2019).

[12] J. Sisler, S. Khan, A. H. Ip, M. W. Schreiber, S. A. Jaffer, E. R. Bobicki, C.-T. Dinh, and E. H. Sargent, *Ethylene electrosynthesis: A comparative techno-economic analysis of alkaline vs membrane electrode assembly vs CO_2–CO–C_2H_4 tandems,* ACS Energy Letters **6**, 997 (2021).

[13] M. Ramdin, B. De Mot, A. R. T. Morrison, T. Breugelmans, L. J. P. van den Broeke, J. P. M. Trusler, R. Kortlever, W. de Jong, O. A. Moultos, P. Xiao, P. A. Webley, and T. J. H. Vlugt, *Electroreduction of CO_2/CO to C_2 products: Process modeling, downstream separation, system integration, and economic analysis,* Industrial & Engineering Chemistry Research **60**, 17862 (2021).

[14] M. G. Kibria, J. P. Edwards, C. M. Gabardo, C.-T. Dinh, A. Seifitokaldani, D. Sinton, and E. H. Sargent, *Electrochemical CO_2 reduction into chemical feedstocks: From mechanistic electrocatalysis models to system design,* Advanced Materials **31**, 1807166 (2019).

[15] P. D. Luna, C. Hahn, D. Higgins, S. A. Jaffer, T. F. Jaramillo, and E. H. Sargent, *What would it take for renewably powered electrosynthesis to displace petrochemical processes?* Science **364**, eaav3506 (2019).

[16] J. M. Spurgeon, N. Theaker, C. A. Phipps, S. S. Uttarwar, and C. A. Grapperhaus, *Comparative technoeconomic analysis of pathways for electrochemical reduction of CO_2 with methanol to produce methyl formate,* ACS Sustainable Chemistry & Engineering **10**, 12882 (2022).

[17] A. Somoza-Tornos, O. J. Guerra, A. M. Crow, W. A. Smith, and B.-M. Hodge, *Process modeling, techno-economic assessment, and life cycle assessment of the electrochemical reduction of CO_2: a review,* iScience **24**, 102813 (2021).

[18] S. Nitopi, E. Bertheussen, S. B. Scott, X. Liu, A. K. Engstfeld, S. Horch, B. Seger, I. E. L. Stephens, K. Chan, C. Hahn, J. K. Nørskov, T. F. Jaramillo, and I. Chorkendorff, *Calculation for the cathode surface concentrations in the electrochemical reduction of CO_2 in $KHCO_3$ solutions,* Journal of Applied Electrochemistry **36**, 161 (2006).

[19] K. Wu, E. Birgersson, B. Kim, P. J. A. Kenis, and I. A. Karimi, *Modeling and experimental validation of electrochemical reduction of CO_2 to CO in a microfluidic cell,* Journal of The Electrochemical Society **162**, F23 (2014).

[20] L.-C. Weng, A. T. Bell, and A. Z. Weber, *Modeling gas-diffusion electrodes for CO_2 reduction,* Physical Chemistry Chemical Physics **20**, 16973 (2018).

[21] T. Burdyny and W. A. Smith, *CO_2 reduction on gas-diffusion electrodes and why catalytic performance must be assessed at commercially-relevant conditions,* Energy & Environmental Science **12**, 1442 (2019).

[22] D. G. Wheeler, B. A. W. Mowbray, A. Reyes, F. Habibzadeh, J. He, and C. P. Berlinguette, *Quantification of water transport in a CO_2 electrolyzer,* Energy & Environmental Science **13**, 5126 (2020).

[23] M. Heßelmann, B. C. Bräsel, R. G. Keller, and M. Wessling, *Simulation-based guidance for improving CO_2 reduction on silver gas diffusion electrodes,* Electrochemical Science Advances **3**, 2100160 (2023).

[24] C. McCallum, C. M. Gabardo, C. P. O'Brien, J. P. Edwards, J. Wicks, Y. Xu, E. H. Sargent, and D. Sinton, *Reducing the crossover of carbonate and liquid products during carbon dioxide electroreduction,* Cell Reports Physical Science **2**, 100522 (2021).

[25] O. Romiluyi, N. Danilovic, A. T. Bell, and A. Z. Weber, *Membrane-electrode assembly design parameters for optimal CO_2 reduction,* Electrochemical Science Advances **3**, e2100186 (2023).

[26] R. Kas, A. G. Star, K. Yang, T. Van Cleve, K. C. Neyerlin, and W. A. Smith, *Along the channel gradients impact on the apatioactivity of gas diffusion electrodes at high conversions during CO_2 electroreduction,* ACS Sustainable Chemistry & Engineering **9**, 1286 (2021).

[27] S. Subramanian, J. Middelkoop, and T. Burdyny, *Spatial reactant distribution in CO_2 electrolysis: Balancing CO_2 utilization and faradaic efficiency,* Sustainable Energy Fuels **5**, 6040 (2021).

[28] S. A. Hawks, V. M. Ehlinger, T. Moore, E. B. Duoss, V. A. Beck, A. Z. Weber, and S. E. Baker, *Analyzing production rate and carbon utilization trade-offs in CO2RR electrolyzers,* ACS Energy Letters **7**, 2685 (2022).

[29] C.-T. Dinh, T. Burdyny, M. G. Kibria, A. Seifitokaldani, C. M. Gabardo, F. P. G. de Arquer, A. Kiani, J. P. Edwards, P. D. Luna, O. S. Bushuyev, C. Zou, R. Quintero-Bermudez, Y. Pang, D. Sinton, and E. H. Sargent, *CO_2 electroreduction to ethylene via hydroxide-mediated copper catalysis at an abrupt interface,* Science **360**, 783 (2018).

[30] Y. C. Tan, K. B. Lee, H. Song, and J. Oh, *Modulating local CO_2 concentration as a general strategy for enhancing C-C coupling in CO_2 Electroreduction,* Joule **4**, 1104 (2020).

[31] S. S. Bhargava, F. Proietto, D. Azmoodeh, E. R. Cofell, D. A. Henckel, S. Verma, C. J. Brooks, A. A. Gewirth, and P. J. A. Kenis, *System design rules for intensifying the electrochemical reduction of CO_2 to CO on Ag nanoparticles,* ChemElectroChem **7**, 2001 (2020).

[32] B.-U. Choi, Y. C. Tan, H. Song, K. B. Lee, and J. Oh, *System design considerations for enhancing electroproduction of formate from simulated flue gas,* ACS Sustainable Chemistry & Engineering **9**, 2348 (2021).

[33] M. Ma, E. L. Clark, K. T. Therkildsen, S. Dalsgaard, I. Chorkendorff, and B. Seger, *Insights into the carbon balance for CO_2 electroreduction on Cu using gas diffusion electrode reactor designs,* Energy & Environmental Science **13**, 977 (2020).

[34] M. Ma, S. Kim, I. Chorkendorff, and B. Seger, *Role of ion-selective membranes in the carbon balance for CO_2 electroreduction via gas diffusion electrode reactor designs,* Chemical Science **11**, 8854 (2020).

[35] J. Rabinowitz and M. Kanan, *The future of low-temperature carbon dioxide electrolysis depends on solving one basic problem,* Nature Communications **11**, 5231 (2020).

[36] D. A. G. Bruggeman, *Berechnung verschiedener physikalischer konstanten von heterogenen substanzen. i. dielektrizitätskonstanten und leitfähigkeiten der mischkörper aus isotropen substanzen,* Annalen der Physik **416**, 636 (1935).

[37] A. Lévêque, *Les Lois de la transmission de chaleur par convection* (Dunod, 1928).

[38] W. Deen, *Analysis of Transport Phenomena*, Topics in Chemical Engineering (Oxford University Press USA, New York City, 1998).

[39] M. Faraday, *VI. experimental researches in electricity.-seventh series,* Philosophical Transactions of the Royal Society of London **124**, 77 (1834).

[40] T. Hatsukade, K. P. Kuhl, E. R. Cave, D. N. Abram, and T. F. Jaramillo, *Insights into the electrocatalytic reduction of CO_2 on metallic silver surfaces,* Physical Chemistry Chemical Physics **16**, 13814 (2014).

[41] K. P. Kuhl, E. R. Cave, D. N. Abram, and T. F. Jaramillo, *New insights into the electrochemical reduction of carbon dioxide on metallic copper surfaces,* Energy & Environmental Science **5**, 7050 (2012).

[42] A. Paturska, M. Repele, and G. Bazbauers, *Economic assessment of biomethane supply system based on natural gas infrastructure,* Energy Procedia **72**, 71 (2015).

[43] A. Raksajati, M. T. Ho, and D. E. Wiley, *Reducing the cost of CO_2 capture from glue gases using aqueous chemical absorption,* Industrial & Engineering Chemistry Research **52**, 16887 (2013).

[44] N. M. Haegel, R. Margolis, T. Buonassisi, D. Feldman, A. Froitzheim, R. Garabedian, M. Green, S. Glunz, H.-M. Henning, B. Holder, I. Kaizuka, B. Kroposki, K. Matsubara, S. Niki, K. Sakurai, R. A. Schindler, W. Tumas, E. R. Weber, G. Wilson, M. Woodhouse, and S. Kurtz, *Terawatt-scale photovoltaics: Trajectories and challenges,* Science **356**, 141 (2017).

[45] J.-B. Vennekoetter, R. Sengpiel, and M. Wessling, *Beyond the catalyst: How electrode and reactor design determine the product spectrum during electrochemical CO_2 reduction,* Chemical Engineering Journal **364**, 89 (2019).

[46] L. C. Brée, M. Wessling, and A. Mitsos, *Modular modeling of electrochemical reactors: Comparison of CO_2–electolyzers,* Computers and Chemical Engineering **139**, 106890 (2020).

[47] L.-C. Weng, A. T. Bell, and A. Z. Weber, *A systematic analysis of Cu-based membrane-electrode assemblies for CO_2 reduction through multiphysics simulation,* Energy & Environmental Science **13**, 3592 (2020).

[48] I. Bagemihl, C. Bhatraju, J. R. van Ommen, and V. van Steijn, *Electrochemical reduction of CO_2 in tubular flow cells under gas–liquid Taylor flow,* ACS Sustainable Chemistry & Engineering **10**, 12580 (2022).

[49] Z. Yang, D. Li, L. Xing, H. Xiang, J. Xuan, S. Cheng, E. H. Yu, and A. Yang, *Modeling and upscaling analysis of gas diffusion electrode-based electrochemical carbon dioxide reduction systems,* ACS Sustainable Chemistry & Engineering **9**, 351 (2021).

[50] E. E. Hills, M. H. Abraham, A. Hersey, and C. D. Bevan, *Diffusion coefficients in ethanol and in water at 298K: Linear free energy relationships,* Fluid Phase Equilibria **303**, 45 (2011).

[51] P. Linstrom, *Nist chemistry webbook, nist standard reference database 69,* (1997).

[52] W. Haynes, *CRC Handbook of Chemistry and Physics*, 95th ed. (CRC Press, Boca Raton, FL, 2014).

[53] A. Damjanovic, A. Dey, and J. Bockris, *Kinetics of oxygen evolution and dissolution on platinum electrodes,* Electrochimica Acta **11**, 791 (1966).

[54] K. R. M. Corpus, J. C. Bui, A. M. Limaye, L. M. Pant, K. Manthiram, A. Z. Weber, and A. T. Bell, *Coupling covariance matrix adaptation with continuum modeling for determination of kinetic parameters associated with electrochemical CO_2 reduction,* Joule **7**, 1289 (2023).

[55] K. Schulz, U. Riebesell, B. Rost, S. Thoms, and R. Zeebe, *Determination of the rate constants for the carbon dioxide to bicarbonate inter-conversion in pH-buffered seawater systems,* Marine Chemistry **100**, 53 (2006).

[56] F. J. Millero, T. B. Graham, F. Huang, H. Bustos-Serrano, and D. Pierrot, *Dissociation constants of carbonic acid in seawater as a function of salinity and temperature,* Marine Chemistry **100**, 80 (2006).

[57] P. Dragnea and C. Bildea, *Process optimization of a butane-butene alkylation plant,* UPB Scientific Bulletin, Series B: Chemistry and Materials Science **76** (2014).

[58] A. D. Wiheeb, Z. Helwani, J. Kim, and M. R. Othman, *Pressure swing adsorption technologies for carbon dioxide capture,* Separation & Purification Reviews **45**, 108 (2015).

[59] D. Noren and M. Hoffman, *Clarifying the butler–volmer equation and related approximations for calculating activation losses in solid oxide fuel cell models,* Journal of Power Sources **152**, 175 (2005).

[60] L. M. Baumgartner, C. I. Koopman, A. Forner-Cuenca, and D. A. Vermaas, *Narrow pressure stability window of gas diffusion electrodes limits the scale-up of CO_2 electrolyzers,* ACS Sustainable Chemistry & Engineering **10**, 4683 (2022).

[61] J. Zhang, W. Luo, and A. Züttel, *Crossover of liquid products from electrochemical CO_2 reduction through gas diffusion electrode and anion exchange membrane,* Journal of Catalysis **385**, 140 (2020).

[62] N. Wang, R. K. Miao, G. Lee, A. Vomiero, D. Sinton, A. H. Ip, H. Liang, and E. H. Sargent, *Suppressing the liquid product crossover in electrochemical CO_2 reduction,* SmartMat **2**, 12 (2021).

5

CONCLUSION AND OUTLOOK

5.1. ELECTROREDUCTION OF CO_2 UNDER TAYLOR FLOW

The utilisation of flow-through electrolysers with gas-diffusion electrodes (GDEs) has been a prevalent approach for the reduction of CO_2 to mitigate mass transfer limitations within liquid electrolytes. Despite its conceptual similarity to fuel cells, this design poses challenges for long term operation and scale-up such as flooding and salt precipitation within the GDE. Addressing these challenges is imperative for realising the full potential of this electrolyser type. An alternative approach involves operating electrolysers under gas-liquid Taylor flow, potentially enhancing mass transfer without the need for a GDE. Chapter 2 and 3 aimed to explore the viability of gas-liquid Taylor flow as an alternative for the electrochemical conversion of CO_2.

First, a numerical model to evaluate the reactor performance of Taylor flow in a tubular electrolyser was developed in Chapter 2. The numerical model allowed to investigate the influence of velocity and void fraction on current density and Faradaic efficiency within a tubular flow cell for the reduction of CO_2 to CO. Our findings highlight the significance of the thin liquid film around the gaseous CO_2 bubbles in facilitating mass transfer, particularly at low velocities. Consequently, enhancing the Faradaic efficiency towards CO production favours operation under Taylor flow with long gaseous CO_2 bubbles at low velocities. Moreover, the tubular design's compatibility with high pressure operation presents an opportunity for further enhancing the current density towards CO, potentially making it a promising alternative to conventional GDE designs.

The influence of gas-liquid Taylor flow on the Faradaic efficiency and current density was then experimentally tested in Chapter 3. For this we adapted a common zero-gap electrolyser design with a membrane electrode assembly (MEA), introducing a silver gauze on the cathode side to allow for the reduction of CO_2 to CO. Operating this flow cell with a pure CO_2-saturated liquid electrolyte feed compared to introducing gaseous CO_2 Taylor bubbles in the rectangular channels shows a significant increase in Faradaic efficiency at a fixed current density. Contrary to previous findings in tubular reactors, increasing the gas-to-liquid ratio did not significantly affect Faradaic efficiency, while an increase in two-phase velocity correlated with an increase in Faradaic efficiency.

The analysis from Chapter 2 and 3 indicates a need to explore the impact of electrode design and increased pressure on structured electrolysers operated under gas-liquid Taylor flow for CO_2 reduction. Here, we discuss some future research directions.

Catalyst-coated membranes are proposed as an alternative to the silver gauze used in Chapter 3 to reduce additional diffusion resistance for CO_2. The silver gauze was chosen for its convenient integration in the electrolyser, not for being the best catalyst design in terms of current density and Faradaic efficiency. A pre-treatment of the gauze similar to silver foils as for example through forced oxidation by plasma treatment is expected to increase the overall observed Faradaic efficiency. Challenges in stable electrode design under Taylor flow, particularly with tubular designs, have been explored in the master thesis project of Hortensius [1]. It was concluded that chemical bonding of the catalyst to a substrate is necessary to prevent washing off the catalyst layer. Coating techniques like atomic layer deposition (ALD) are suggested, although challenges remain in deposition efficiency as explored in the master thesis work from Angistali [2]. Therefore, first determining a "wish-list" for the electrode design by using established coating methods such as airbrushing and then exploring techniques like ALD for longer operational stability of the electrode could be a viable option to explore this research gap. Knowledge gained from catalyst fabrication via ALD for the application in water electrolysers can then potentially be adapted.

Conversion dynamics, especially bubble behaviour, directly affect mass transfer and reactor length. Consideration of a tandem catalyst system, where CO_2 is first reduced and then passed over a copper catalyst for higher hydrocarbon production, is suggested. These aspects could be explored in the electrochemical set-up by adjusting the applied voltage and introducing a copper catalyst either as a sequence with a copper gauze or by coating copper on the silver gauze.

Integrating back-pressure regulators into the electrochemical set-up could facilitate operation under pressure, albeit limited to a few bars due to current design constraints. Safety considerations would need adjustment for this modification.

Scaling up the tubular and the filter-press electrolyser for the operation under gas-liquid Taylor flow requires addressing feed uniformity and velocity optimisation for mass transfer and heat management. Incorporating heat transfer and Joule heating into numerical models could aid in analysing trade-offs, though with increased computational complexity. Research gaps associated with scaling up tubular or filter-press electrolyser designs, not limited to Taylor flow operation, are identified as following:

1. How can an equal feed of stable Taylor flow across multiple channels be ensured?
2. What are the trade-offs for achieving optimal velocity in terms of mass transfer rates and heat management?

Ensuring uniform Taylor flow distribution across multiple channels is a challenge not unique to CO_2 electrolysers, and it is being explored in other research areas [3]. Solutions from these endeavours could potentially be adapted for implementation here. Incorporating heat transfer and joule heating into the numerical model presented in Chapter 2 may help address mass transfer and heat management concerns. However, extending this model to longer channels would increase computational demands. Initially, the established model could undergo sensitivity analysis to identify relevant trade-offs. Research gaps unique to scaling up tubular or filter-press electrolyser designs, not only in the context of Taylor flow operation, are identified and briefly discussed in subsequent sections.

5.1.1. TUBULAR ELECTROLYSERS

Tubular electrolysers have garnered attention across various electrochemical applications, including high-temperature solid oxide fuel cells and low-temperature polymer electrolyte membrane (PEM) fuel cells [4] and water electrolysers [5], due to their enhanced surface-area to volume ratio, uniform contact pressure, and potential for cost reduction. In the realm of CO_2 electrolysis, tubular GDEs, known as hollow fibres, have gained traction driving experimental development and scale-up efforts [6].

However, there is limited knowledge on the scale-up of tubular electrolysers with Laube *et al.* [5] proposing to bundle the individual tubes of a proton exchange membrane water electrolyser cells similar to tubular heat exchanges or in a stack. The patent by Meerkerk [7] (NEWES BV, NL) similarly describes a stacked design for the multiple tubes. As a first step this design could be adapted for CO_2 electrolysis and scaled to a small test cell with a few tubes if proven successful in a singular tube. This test set-up could than aid in understanding current distribution, energy efficiency, and the potential of operation under fluctuating energy input through pairing it with a modelling approach. Due to the complexity of modelling CO_2 electrolysers, as described in the following section in some more detail, these research gaps are likely best to be tackled first for water electrolyser cells or fuel cells before transferring the knowledge to CO_2 electrolyser.

5.1.2. FILTER-PRESS ELECTROLYSERS

Filter-press electrolysers incorporating zero-gap membrane electrode assemblies (MEAs) have emerged as a promising design for scaling up CO_2 electrolysers. These electrolysers consist of flow plates at the anode and cathode to distribute reactants and remove products. Situated between these flow plates, separating the anode and cathode is a polymeric membrane. Despite the challenge of enhancing the selectivity of the anion exchange membrane for CO_2 electrolyser, as also pursued in water electrolysis, the design of the flow plate plays a crucial role in scaling up.

When scaling up CO_2 electrolysers operated under gas-liquid Taylor flow, addressing the influence of under-rib flow (convection through the porous electrode between flow channel zones) on flow stability becomes important in flow plate design. Initial steps to address this research gap were undertaken in the master thesis work by Uche [8]. Combining the electrolyser cell design from Schneider's master thesis [9] with the Taylor-flow setup described in Chapter 3 would enable an assessment of the extent to which under-rib flow disrupts Taylor flow and how this disruption affects reactor performance. Additionally, the honeycomb-like electrolyser design proposed by Rajaei and Haverkort [10] presents an intriguing avenue for scaling up CO_2 electrolysers under Taylor flow, given its resemblance to monolithic reactors commonly used for Taylor flow reactors in thermo-catalysis.

Further, achieving a uniform distribution of reactants, heat, and current to enhance the operational stability of CO_2 electrolysers, requires optimisation of the flow field design and operating conditions. Numerical modelling combined with experimental insights, as demonstrated by Subramanian *et al.*[11] for CO_2 electrolysis and Olesen *et al.* [12] for water electrolysers, holds promise for assessing these parameters. However, owing to the complexity of numerically solving all relevant governing equations in CO_2 electrolysis [13], careful consideration is necessary to evaluate how phenomena can be de-

coupled, and estimates of the magnitude of effects should be prioritised. First steps in this direction have been made in the thesis work from Weisser Lopez and Jacobs [14, 15]. Experimental techniques that enable observation of an operating electrolyser and assessment of heat distribution [16] and local pH development [17] are invaluable tools for evaluating relevant phenomena and represent an important initial step in determining which phenomena to incorporate into future large-scale models.

5.2. THE ASSESSMENT OF CO_2 ELECTROLYSERS

The assessment of electrochemical reactors for CO_2 conversion typically revolves around key performance metrics such as current density (reaction rate), Faradaic efficiency (selectivity) towards the desired product, and cell potential (required energy input/energy efficiency). Techno-economic studies have set threshold values that an electrochemical reactor must achieve for economic viability. However, these studies often overlook experimentally reported interdependencies among these performance metrics. In Chapter 4, we demonstrated how these interdependencies impact the economic outlook through a multi–scale model. For this we built a framework that captures mass transfer effects across the channel length of an alkaline, gas-diffusion electrode (GDE) membrane electrolyser with a flowing catholyte. By coupling the channel-scale dynamics with higher-level process scales and embedding this multi–scale model within an economic framework, we revealed that the derived target values for performance variables strongly depend on the interdependencies described in the channel-scale model. Notably, economically optimal current densities can be significantly lower than previously reported benchmarks, possibly half as low.

Future research on the distribution of reactants, temperature and current density becomes pivotal during scale-up. Integrating these insights at the channel/electrolyser scale could facilitate the derivation of scale-up rules and aid in identifying optimal operational parameters. Beyond the research gaps pertaining to electrolyser design, the broader process and technology surrounding it exert significant influence on desired reactor performance from an economic standpoint. Notably, pre- and post-processing of electrolytes can substantially affect optimal reactor performance and the economic outlook. Moreover, exploring processes for forming higher hydrocarbons and comparing implementation strategies, such as bioreactors versus electro-catalytic and thermo-catalytic methods, holds promise. These research gaps can potentially be addressed through the integration of electrolyser models (e.g., from COMSOL or Matlab) in detailed process modelling (e.g., in Aspen), as explored in the conceptual design project [18] and master thesis work by Kroes [19]. This framework could facilitate the utilisation of superstructured optimisation or serve as an evaluation tool for AI-generated process designs to bring technology development, implementation strategies and economics together. This framework could then be adapted to include studies on process control and operation under a variable energy input.

Despite these technological and economic uncertainties, achieving successful decarbonisation of the process industry necessitates synergy across sectors and countries. Therefore, fostering knowledge exchange across departments and industries, as envisioned by initiatives like the TU Delft e-refinery institute, becomes increasingly vital.

REFERENCES

[1] R. Hortensius, *Design and experimental production of a cylindrical CO_2 reduction reactor using Taylor flow conditions*, Master's thesis, Delft University of Technology (2021).

[2] K. Angistali, *Optimizing the Membrane Electrode Assembly (MEA) for liquid CO_2 electrolysers through ALD*, Master's thesis, Delft University of Technology (2022).

[3] D. A. Hoang, C. Haringa, L. M. Portela, M. T. Kreutzer, C. R. Kleijn, and V. van Steijn, *Design and characterization of bubble-splitting distributor for scaled-out multiphase microreactors,* Chemical Engineering Journal **236**, 545 (2014).

[4] W. Hwang and Y.-E. Sung, *Recent developments of polymer electrolyte membrane fuel cell design,* Journal of Electrochemical Science and Technology **14**, 120 (2023).

[5] A. Laube, A. Hofer, B. Sánchez Batalla, S. Ressel, A. Chica, S. Fischer, C. Weidlich, J. Bachmann, and T. Struckmann, *Tubular membrane electrode assembly for PEM electrolysis,* International Journal of Hydrogen Energy **47**, 15943 (2022).

[6] N. Weber, M. Möntmann, M. Wessling, and R. Keller, *A continuous flow reactor for tubular gas diffusion electrodes,* Chemical Engineering Journal **486**, 150031 (2024).

[7] A. Meerkerk, *High-pressure electrolysis device,* (NL2023635B1, Feb. 2021).

[8] A. I. A. Uche, *The effect of electrolyte composition and concentration on Taylor flow and mass transfer in an electrochemical cell*, Master's thesis, Delft University of Technology (2021).

[9] M. Moreno Schneider, *Carbon dioxide electro-catalyst activation strategy for improved ethylene production*, Master's thesis, Delft University of Technology (2023).

[10] H. Rajaei and J. Haverkort, *Compact monopolar electrochemical stack designs using electrode arrays or corrugated electrodes,* Electrochimica Acta **332**, 135470 (2020).

[11] S. Subramanian, K. Yang, M. Li, M. Sassenburg, M. Abdinejad, E. Irtem, J. Middelkoop, and T. Burdyny, *Geometric catalyst utilization in zero-gap CO_2 electrolyzers,* ACS Energy Letters **8**, 222 (2023).

[12] A. C. Olesen, S. H. Frensch, and S. K. Kær, *Towards uniformly distributed heat, mass and charge: A flow field design study for high pressure and high current density operation of PEM electrolysis cells,* Electrochimica Acta **293**, 476 (2019).

[13] T. Moore, T. Y. Lin, T. Roy, S. E. Baker, E. B. Duoss, C. Hahn, and V. A. Beck, *Simplified models of the bicarbonate buffer for scaled simulations of CO_2 electrolyzers,* Industrial & Engineering Chemistry Research **62**, 16291 (2023).

[14] J. M. Weisser Lopez, *Effect of scale-up on the electrochemical performance of CO_2 electrolysers*, Master's thesis, Delft University of Technology (2022).

[15] B. M. Jacobs, *Designing a simplified model for predicting CO_2 utilization in gas fed electrolyzers in pursuit of industrial applications*, Master's thesis, Delft University of Technology (2023).

[16] H.-P. Iglesias van Montfort and T. Burdyny, *Mapping spatial and temporal electrochemical activity of water and CO_2 electrolysis on gas-diffusion electrodes using infrared thermography,* ACS Energy Letters **7**, 2410 (2022).

[17] L. M. Baumgartner, A. Kahn, M. Hoogland, J. Bleeker, W. F. Jager, and D. A. Vermaas, *Direct imaging of local pH reveals bubble-induced mixing in a CO_2 electrolyzer,* ACS Sustainable Chemistry & Engineering **11**, 10430 (2023).

[18] A. Kolbeins, I. van der Heiden, J. de Mooij, M. Xu, S. van't Hoff, and T. Scholts, *Integration of electrochemical CO_2 reduction reactor into a process system,* (2001).

[19] M. Kroes, *Design of a large-scale electrochemical CO_2 reduction process*, Master's thesis, Delft University of Technology (2023).

PROPOSITIONS

1. Film theory fails to describe mass transfer in Taylor flow at low flow rates in rectangular channels.
   This proposition pertains to Chapter 3 of this thesis and Haase et al., Theoretical Foundations of Chemical Engineering, 2020, 54, 48–63.

2. At low flow rates the mass transfer coefficient in gas-liquid Taylor flow is independent of the void fraction.
   This proposition pertains to Chapter 3 of this thesis.

3. Neither current density nor Faradaic efficiency alone is sufficient to predict profitability of CO_2 electrolysers.
   This proposition pertains to Chapter 4 of this thesis.

4. A multiscale approach in modelling of CO_2 electrolysis is crucial to identify bottlenecks and optimal process parameters.
   This proposition pertains to Chapter 4 of this thesis.

5. Producing base chemicals from seawater is the only sustainable route for the chemical industry.

6. A key challenge in CO_2 and water electrolysis is not material optimization but reactor design.

7. Transport phenomena courses must include transport of charged species.

8. Institutional and personal biases make universities the ideal environment for discrimination and exclusion.

9. The academic career path is not made for family-oriented people.

10. Governments should prohibit any gender-related advertisement for children's products to provide the foundation for equal career chances.

ACKNOWLEDGEMENTS

Life need not be easy, provided only that it is not empty. – Lise Meitner

The past four years have held their unique set of challenges but have also been filled with wonderful people and experiences. First of all, I would like to thank Ruud and Volkert for their support and invaluable feedback during this time. I have always enjoyed the autonomy you gave me in conceptualising and refining project ideas, coupled with insightful discussions on their practicality. Ruud, your creation of opportunities beyond my research project, such as diving into university teaching by taking over the electrochemistry part of the multi-phase reactor engineering course, has been very valuable to me. I am grateful as it allowed me to find my passion for teaching, one I aspire to nurture in the future. Volkert, your eye for detail and insatiable curiosity have motivated me to continuously challenge and improve my understanding of various concepts. In this, I cherish the approach you taught me of developing an "umbrella picture".

I was fortunate to work on a project which fostered collaboration with various research groups. Ruud K., Tom, and Mar, I am very thankful for the scientific discussions, which helped to shape and strengthen my understanding and approach in tackling the research gaps in the CO_2 electrolysis world. Leslie, Maryam, and John, thank you for your support in communicating our research beyond the borders of TU Delft, for example, organising fun days-out with the project partners or filming a short movie. Asvin, I enjoyed exploring how we can combine the electrolyser model with process simulations through multiple student projects.

The experimental part of this dissertation was quite an adventure for me, and I am very thankful to all the people who made this a success in the end. Christiaan, Mojgan, and Stephan, thank you for your patience and guidance in setting up the lab, writing safety reports, and designing the test cell. Saeed, Erdem, Jorrit, Lorenz, and Nandalal, thank you for sharing your wealth of knowledge on analysis and experimental techniques.

I am very thankful to the group of BSc. and MSc. students I got to work with. You did not just help push the scientific projects forward but also made me grow in the role of your advisor. Sayujya, Chaitanya, Frederike, Ada, Lucas, Iulian, Ruben, Kleio, Max, Julia, Mateo, Berend, Matthijs, I have enjoyed getting to know each one of you.

I got to meet wonderful people who joined my journey for a smaller or a greater part as fellow PhD students, exchange students, and postdocs. Thank you all for your encouragement when things failed, the fun scientific and non-scientific discussions during the lunch break, and the warm office environment you created. I am lucky enough that I met so many great people that it's just too much to mention you all here, but I hope you are all aware of my appreciation towards you.

I am especially thankful for the people that went from office mates to friends. Dominik, Zaid, Aswin I will forever cherish our Corona-walks through Delft and anything within 2h walking distance. Exploring the to-go options of almost any restaurant or cook outs and game nights have been something to look forward to on the weekends. Mag you joined when Corona was becoming a thing of the past but with your lively attitude it quickly felt like you have always been around. I enjoyed our trip to Hamburg and am looking forward to establishing the tradition of a yearly weekend trip together.

Aswin, you have somehow been my ride or die through these past four years. Starting from watching me click the submit button for my first paper submission to helping me defend my thesis. I am already missing our bike rides back home talking about life and science.

Zum Schluss möchte ich meiner Familie und meinen Freunden die eigentlich auch schon als Familie zählen danken. Keiner kennt mich besser als ihr und Euer unaufhörlicher Glaube an mich und meine Fähigkeiten hat mich über jedes noch so hohe Hindernis getragen. Sven, deine Begeisterung und deine Motivation Lösungen für jegliches Problem zu finden sind ansteckend. Doris, du hast mir beigebracht "Misserfolge" zu feiern für den Versuch etwas zu lernen. Kester, deine Gelassenheit und dein Pragmatismus geben mir immer ein Gefühl von Sicherheit und Zuversicht. Lukas, diese Dissertation ist wohl genauso dein Erfolg wie meiner. Nächtelang hast du manchmal neben mir gesessen wenn ich nicht schlafen konnte weil eine Gleichung kein Sinn ergab oder ich noch "kurz" etwas zuenden schreiben musste. Ich bin unendlich dankbar mit dir an meiner Seite das Abenteur Leben zu bestreiten und freu mich darauf die Welt mit Dir und unser wundervollen kleinen Tochter in den kommenden Jahren nocheinmal ganz neu zu entdecken.

CURRICULUM VITÆ

Isabell Bagemihl was born on August 6th, 1994 in Hamburg, Germany. In 2016, she completed her B.Sc. degree in process engineering at Hamburg University of Applied Sciences. She then moved to Stuttgart and majored in chemical and plastics engineering during her M.Sc. program at the University of Stuttgart. She completed her studies in 2019 in the group of Prof. dr. C. Bonten working on the prediction of structural mechanical properties of fiber reinforced plastic parts by means of coupled process simulations considering the fiber microstructure and matrix plasticity. Part of this work was carried out at the group of Prof. dr. T. Osswald at the University of Wisconsin Madison. The work was awarded with the national best thesis award in 2019 in the field of: Methods and approaches for the development and design of plastic compounds from the WAK (Wissenschaftlicher Arbeitskreis der Kunststofftechnik). From 2019, she started working at the Chemical Engineering Department, Faculty of Applied Sciences, Delft University of Technology as a PhD candidate. She worked on the reactor design and the influence of flow patterns (Taylor flow) on the performance of the electrochemical conversion of CO_2 to value added products under the supervision of her promoters Prof. dr. J.R. van Ommen and Dr. V. van Steijn.

LIST OF PUBLICATIONS

JOURNAL PUBLICATIONS RELATED TO THIS DISSERTATION:

3. **I. Bagemihl**, N. Girichandran, S. Saeedy, J. Bleeker, Albert Santoso, Saeed Saedy, R. Kortlever, J.R. van Ommen, V. van Steijn, "Exploring the viability of a Taylor flow electrolyser for enhanced CO_2 electrolysis.", *Under preparation.*

2. **I. Bagemihl**, L. Cammann, M. Pérez-Fortes, V. van Steijn, J.R. van Ommen, "Techno-economic Assessment of CO_2 Electrolysis: How interdependencies between model variables propagate across different modelling scales." *ACS Sustainable Chem. Eng.*, 2023.

1. **I. Bagemihl**, C. Bhatraju, J.R. van Ommen, V. van Steijn, "Electrochemical reduction of CO_2 in tubular flow cells under gas–liquid Taylor flow." *ACS Sustainable Chem. Eng.*, 2022.

OTHER JOURNAL PUBLICATIONS:

2. J. Bleeker; S. S. J. Deursen; L. C. Bakker; T. J. J. M. van Overveld; K. M.R. Lawrence; **I. Bagemihl**; G. Lastrucci; D. Bosma; C. V. Schinkel; E. C. Wagner; J.R. Ommen; D. Vermaas, "Pressure-pulsed flow triples mass transport in aqueous CO_2 electrolysis.", *Under review.*

1. A. S. Kumar, M. Kroes, **I. Bagemihl**, R. Kortlever, W. Jong, M. Ramdin, "Process modelling and techno-economic analysis of an integrated large scale CO_2/CO reduction plant to produce C_{2+} products.", *Under preparation.*

CONFERENCE PROCEEDINGS/PRESENTATIONS:

5. **I. Bagemihl**, L. Cammann, M. Pérez-Fortes, V. van Steijn, J.R. van Ommen, AIChE Annual Meeting, Phoenix, United States of America, *Oral Presentation*, 2022.

4. **I. Bagemihl**, V. van Steijn, J.R. van Ommen, ECCM2022, the Hague, the Netherlands, *Poster Presentation*, 2022.

3. **I. Bagemihl**, C. Bhatraju, J.R. van Ommen, V. van Steijn, NPS17, Delft, the Netherlands, *Oral Presentation*, 2022.

2. **I. Bagemihl**, C. Bhatraju, J.R. van Ommen, V. van Steijn, ECCEAB, *online*, *Oral Presentation*, 2021.

1. **I. Bagemihl**, J.R. van Ommen, V. van Steijn, Physics @ Veldhoven, Veldhoven, the Netherlands, *Poster Presentation*, 2020.